AD/A-006 467

IDENTIFICATION OF EARTHQUAKES AND UNDERGROUND EXPLOSIONS

Eugene Herrin

Southern Methodist University

Prepared for:

Air Force Office of Scientific Research
Advanced Research Projects Agency

February 1975

UNCLASSIFIED

SECURITY CLASSIFICATION OF THIS PAGE (When Data Entered)

REPORT DOCUMENTATION PAGE

READ INSTRUCTIONS BEFORE COMPLETING FORM

1. REPORT NUMBER: AFOSR - TR - 75 - 0314
2. GOVT ACCESSION NO.
3. RECIPIENT'S CATALOG NUMBER

4. TITLE (and Subtitle): IDENTIFICATION OF EARTHQUAKES AND UNDERGROUND EXPLOSIONS

5. TYPE OF REPORT & PERIOD COVERED: Final

6. PERFORMING ORG. REPORT NUMBER

7. AUTHOR(s): Eugene Herrin

8. CONTRACT OR GRANT NUMBER(s): AFOSR 71-213 2

9. PERFORMING ORGANIZATION NAME AND ADDRESS:
Dallas Geophysical Laboratory
Southern Methodist University
Dallas, Texas 75222

10. PROGRAM ELEMENT, PROJECT, TASK AREA & WORK UNIT NUMBERS: AO 1827-6

11. CONTROLLING OFFICE NAME AND ADDRESS:
Advanced Research Projects Agency
1400 Wilson Blvd.
Arlington, VA 22209

12. REPORT DATE: February 1975

13. NUMBER OF PAGES: 165

14. MONITORING AGENCY NAME & ADDRESS (if different from Controlling Office):
Air Force Office of Scientific Research/NP
1400 Wilson Blvd.
Arlington, VA 22209

15. SECURITY CLASS. (of this report): UNCLASSIFIED

15a. DECLASSIFICATION/DOWNGRADING SCHEDULE

16. DISTRIBUTION STATEMENT (of this Report)

17. DISTRIBUTION STATEMENT (of the abstract entered in Block 20, if different from Report)

Approved for public release;
distribution unlimited.

18. SUPPLEMENTARY NOTES

19. KEY WORDS (Continue on reverse side if necessary and identify by block number)

Rayleigh wave dispersion
Polar paths
Array processing techniques
Network computations
Body wave magnitudes
Rayleigh spectrum
Lateral heterogeneity
Source regions

20. ABSTRACT (Continue on reverse side if necessary and identify by block number)

Research during the reporting period was accomplished in four categories, (a) Analysis of Rayleigh wave dispersion for polar paths; (b) development of improved array processing techniques; (c) determination of bias in network computations of body wave magnitudes; and (d) investigation of the effect on the Rayleigh spectrum of lateral heterogeneity in earthquake source regions. Because of the uniformity of group velocity dispersion within the polar wave guide and the broad-band nature of the Rayleigh waves, "matched" or chirp-filter techniques were found to be particularly effective on data recorded at

DD FORM 1 JAN 73 1473 EDITION OF 1 NOV 65 IS OBSOLETE

PRICES SUBJECT TO CHANGE

UNCLASSIFIED

SECURITY CLASSIFICATION OF THIS PAGE (When Data Entered)

McKinney, Texas, site. The principal components of a major soft-ware system for continuous general analysis of array data have been developed. The system, called FKSCAN, transforms successive blocks of array data to the frequency-wave number domain and explores that space for correlations. A method for correcting the bias in body wave magnitude estimates is described and shows that observations from any seismological network lead to over estimation of the magnitude of seismic events which are near the detection threshold of that network. Studies of Rayleigh wave spectra obtained from a high-gain, long period seismograph at Grand Saline, Texas, show that for earthquakes occurring in some Pacific island arc regions, such as New Hebrides, New Britain, and the Solomons, a shift of spectral energy to longer periods with increasing source depth is observed. However, for earthquakes originating in certain other island arcs, such as Tonga-Kermedec, the Phillipines, and the Marianas, no corresponding spectral shift was observed.

AFOSR - TR - 75 - 0314

FINAL TECHNICAL REPORT

to the

AIR FORCE OFFICE OF SCIENTIFIC RESEARCH

from

Eugene Herrin
Dallas Geophysical Laboratory
Southern Methodist University

ARPA Order: 1827-6
Program Code: 3F10
Name of Contractor: Southern Methodist University
Effective Date of Contract: 1 July 1971
Contract Expiration Date: 30 June 1974
Amount of Contract Dollars: $267,687
Contract Number: 71-2133C
Principal Investigator and Phone Number: Eugene Herrin
#214-692-7295
Program Manager and Phone Number: Truman Cook,
Director
Research Administration
#214-692-2031

Title of Work: Identification of Earthquakes and Underground Explosions

University Account Number: 80-46

Approved for public release;
distribution unlimited.

Sponsored by

Advanced Research Projects Agency

Introduction

Research during the reporting period was accomplished in four categories ---(a) Analysis of Rayleigh wave dispersion for polar paths; (b) development of improved array processing techniques; (c) determination of bias in network computations of body wave magnitudes; and (d) investigation of the effect on the Rayleigh spectrum of lateral heterogeneity in earthquake source regions. Results of the research on these topics have been reported to AFOSR in technical reports, and the technical reports are included as the main body of this final report.

Rayleigh Wave Dispersion

Our studies using long period data recorded in northeast Texas have shown that a wave guide for Rayleigh waves exists from China and the southern border of the USSR across the Arctic to Texas. We determined group velocity dispersion curves for a number of Rayleigh waves which traveled through this polar wave guide and found that at periods greater than 30 seconds the dispersion curve does not vary with epicentral location within the wave guide.

Because of the uniformity of group velocity dispersion within the polar wave guide and the broad-band nature of the Rayleigh waves, "matched" or chirp-filter techniques were found to be particularly effective on data recorded at our

McKinney, Texas, site. A technical report to AFOSR entitled "Continental Rayleigh Wave Dispersion and the Estimation of Chirp-Filter Detectors" by William Tucker, John McDonald, and Eugene Herrin is attached and describes these subjects in detail.

Array Processing Techniques

We have generated the principal components of a major soft-ware system for continuous general analysis of array data. The system, called FKSCAN, transforms successive blocks of array data to the frequency-wave number domain and explores that space for correlations. The powerful advantage of transforming array data from time and physical space into the frequency-wavenumber domain is that, quite generally, correlations are automatically separated and sorted according to frequency, velocity, and azimuth permitting detection and description of signals not readily discerned in time and physical space. Further, spatial filtering is markedly facilitated in transform space and, as one consequence, large overriding signals may, in effect, be "turned off" after the fact to permit the detection of much smaller simultaneous arrivals. FKSCAN, after transforming and exploring each array data block, filters and removes the principal signals and correlations

thus detected and searches the transform space once again for any small, hidden signals.

FKSCAN then outputs a bulletin for each data block citing detections and printing out the frequency power spectral estimates of those signals. For each such signal there are also output spectra of phase-velocity, back azimuth, and F-statistic as functions of frequency. (The F-statistic is a measure of the likclihood that detected correlations are genuine; i.e., not due to chance combinations of noise).

An auxiliary program called FKPLOT was written which outputs contoured printer plots of cross-sections of frequency wavenumber spectra cut normal to the frequency axis.

Bias in Network Estimation of Body Wave Magnitudes

A method for correcting the bias in body wave magnitude (m_b) estimates is described in an enclosed technical report to the AFOSR entitled "On the Estimation of Body Wave Magnitudes" by Eugene Herrin and William Tucker. This report shows that observations from any seismological network lead to over estimation of the magnitude of seismic events which are near the detection threshold of that network. Methods are presented for calculating this magnitude bias. Consideration must be given to this effect in comparing networks with significantly different thresholds, in comparing theoretical and empirical estimates of network capability, and in

determining the source energy of small seismic events.

Effect on the Rayleigh Spectrum of Lateral Heterogeneity in Earthquake Source Areas

Studies of Rayleigh wave spectra obtained from a high-gain, long period seismograph at Grand Saline, Texas, show that for earthquakes occurring in some Pacific island arc regions, such as New Hebrides, New Britain, and the Solomons, a shift of spectral energy to longer periods with increasing source depth is observed. This is consistent with theoretical predictions for simple sources in laterally homogeneous layered media. However, for earthquakes originating in certain other island arcs, such as Tonga-Kermedec, the Phillipines, and the Marianas, no corresponding spectral shift was observed. In the first group of island arcs, the lithospheric plate dips more or less toward the recording site at Grand Saline; in the second group, the dip is away from Grand Saline. It is suggested that lateral heterogeneity in the earthquake source regions is at least partially responsible for the spectral differences and that in particular the downward bent lithosphere acts as a wave guide at some azimuths for some Rayleigh wave lengths. An enclosed technical report to AFOSR entitled "A Model Study of the Effect on the Rayleigh Spectrum of Lateral Heterogeneity in Earthquake Source Regions" by Tom Goforth describes a verification of this hypothesis using an analog scale model.

The study indicates that for intermediate and deep-focus earthquakes in subduction zones, higher values of Ms will be observed at azimuths opposite to the direction of dip of the lithospheric plate than would occur if the same earthquake had occurred in laterally homogeneous layered media.

ABSTRACT

Rayleigh wave data were recorded by a single vertical high-gain seismograph located in north Texas. It was found that Rayleigh waves propagating in a continental path over the pole to this station exhibited very stable dispersion characteristics, particularly in the period range 35-75 secs: at shorter periods an average dispersion curve could be estimated. A composite dispersion curve was used to develop "chirp" (or matched) filters, the form of which depended on the distance between the seismograph and the event. Such filters are shown to be very efficient in improving the signal-to-noise ratio of Rayleigh waves emanating from events in the Sino-Soviet region and can be used as a means of separating "mixed" Rayleigh waves. For the path over the pole (or "polar waveguide") the detection threshold is estimated to be at $M_s = 3.5$.

INTRODUCTION

Ewing and Press (1952) described the classical "peak-and-trough" method of determining a fundamental dispersion curve from a single surface wave coda. Satô (1955) applied Fourier analysis to the calculation of dispersion curves. These techniques have been improved upon (Block and Hales, (1968), Landisman, et al (1969) and Dziewonski, et al (1969)), and an overall processing system was devised combining Fourier analysis and time-varying filters, enabling the calculation of, not only the fundamental phase and group velocity curves, but also the curves for the higher modes. In particular, once a group velocity curve has been obtained it is possible to design a time varying filter that extracts a single dispersed mode and effects a significant improvement in the signal-to-noise ratio. The filtered output is then an estimate of the true signal. Dziewonski, et al (1968) summarizes these methods and it is evident that they extract the maximum amount of information from the surface wave signal. Nevertheless, the methods are both time consuming and computationally difficult. But if we restrict the investigation to the fundamental mode of surface wave propagation, it becomes

possible to develop a fast, simple digital technique for the analysis.

In this paper we describe a scheme which estimates the fundamental group velocity dispersion curve from a seismogram, and then constructs a "matched" filter based on the estimated curve. This matched, or chirp, filter can then be used to operate on signals with low signal-to-noise ratios.

THE SEISMOGRAMS

During the period March through August 1970 a three-component seismograph system was operated at a depth of 180 m in the Morton Salt Company mine at Grand Saline, Texas (Sorrells et al., 1971). The seismometers were sealed in such a manner that the masses were not subject to buoyancy effects from atmospheric pressure changes. The systems were of the "advanced" long period type which are operated with a peak magnification at a period of 50 secs. Sorrells et al. (1971) have shown that if such a system is operated at a site which is remote from seismic noise generated by atmospheric processes, the spectra of the long period noise exhibits a minimum in the period range 20-60 sec. Careful installation of these seismographs at a depth of about 180 m enabled the vertical seismograph, the only one used in the present study, to be operated at a magnification of 200,000. The data were recorded on a digital acquisition system described by Herrin and McDonald (1971) after sampling at a rate of 1 per second.

The recorded seismograms were associated with source parameters and body wave magnitudes provided in Preliminary Determination of Epicenters (PDE) issued by NOAA.

DISPERSION CURVE ESTIMATION

A computer program was written which enabled analog representations of digital time series to be displayed on an oscilloscope. Selected seismograms were then plotted, using a Cal-comp plotter. It was decided to limit the observations to Rayleigh waves recorded at teleseismic distance which had traversed a predominantly continental path; thus restricting the range of azimuths to about 15^{o} east and west of the pole, and the range of epicentral distances to 55^{o}-130^{o}.

Using the plot of the seimogram an estimation was made of the start time (T_s) and the length, in seconds, (window) of the Rayleigh signal. A computer program was written which searched this window, starting at T_s, for zero crossings, in a manner similar to the "peak and trough" technique of Ewing and Press, (1952). The time of the "actual" zero crossing was calculated by triangulation between the last point immediately prior to a zero crossing, and the first point immediately after it. The initial zero crossing time, (T_0) was stored, and at the next zero crossing, (T_1) the first period, (P_1) was computed. T_1 and P_1 were then stored and the seach continued until the window was exhausted. For i = 1, 2, ..., N, the group velocites and the periods were computed from

$$V_i = \frac{\Delta}{TT_i} \quad \text{and} \quad P_i = 2\,(T_i - T_{i-1}),$$

where N = the number of zero crossings in the window,

Δ = the epicentral distance from event to station in km, and

TT_i = the observed travel time from source to the ith zero crossing.

Since the actual zero crossing occurred within a one second interval any variation must be less than one second. As a conservative approximation, we assumed the error to be uniform; thus the variance was 1/12 sec^2.

Now $TT_i = T_i - 0$

where 0 is the origin time of the event. From Herrin et al. (1968) a reasonable origin time variance is 0.81 to 1.00 sec^2. Since T_i and 0 are independent observations their variances may be added. We thus take 1.00 sec^2 as a reasonable variance for each TT_i. From Tucker et al. (1968) and Herrin et al. (1968) a reasonable variance in Δ is 900 km^2. We then have

$$V_i = \frac{\Delta + e_1}{TT_i + e_2},$$

where Δ = the true distance (in km)

TT_i = the true travel time,

e_1 = the error in epicentral distance (σ_1=30 km),

e_2 = the error in travel time (σ_2= 1 sec).

Assuming an event with Δ = 6000 km and a maximum group velocity of 4.00 km/sec (Oliver, 1962) then

$$V_1 = (6000 + e_1)/(1500 + e_2).$$

Since the variance of e_2 is small relative to 1500 we can ignore e_2 and write

$$V_1 = 4.0 + e_1/1500$$
$$= 4.0 + \delta_1,$$

where

$$\sigma^2_{\delta_1} = 0.0004 \text{ sec}^2.$$

For a lower period cutoff of 20 sec (or a velocity of 3.00 km/sec) we get

$$V_N = (6000 + e_N)/2000$$
$$= 3.0 + e_N/2000$$
$$= 3.0 + \delta_2,$$

where

$$\sigma^2_{\delta_2} = 0.000225 \text{ sec}^2.$$

Thus as a conservative approximation we can assume

$$V_i = \text{True velocity } i + \delta$$

where $\sigma_\delta^2 = 0.0004 \text{ sec}^2$.

Let us now consider the variation in the P_i.

We have $$P_i = 2(T_i - T_{i-1})$$

where $$\sigma_{T_i}^2 = 0.0833 \text{ sec}^2.$$

Since the minimum period is assumed to be 20 sec the minimum time difference is of the order of 10 sec and we may assume that the errors in T_i and T_{i-1} are independent. Then the variance of a P_i is

$$\sigma_{P_i}^2 = 4(0.0833 + 0.0833) = 0.6664 \text{ sec}^2.$$

Thus the variance in a velocity observation is three orders of magnitude less than that of a period observation. We therefore ignored the error in the velocity computations and assumed that the velocities were known without error. Now assuming that all the error lies in the period computations, it is possible to consider a group velocity curve as a regression of period on group velocity.

Figure 2 shows the data points obtained from dispersed

Rayleigh waves for three events located in the Arctic (Table 1) at similar epicentral distances and similar azimuths. Data from an event in Sinkiang Province along a similar azimuth, but at a greater distance, (Table 1) are shown in Figure 3. A comparison of the data in Figures 2 and 3 in the velocity range 3.50 to 3.90 km/sec (periods approximately 35 and 75 sec respectively) indicates that there is no statistical difference between the true dispersion curve for each event. The observed scatter could result from statistical fluctuations in the estimates or real differences in the velocity-period relationship along the propagation path. Thus it appears that in the velocity range 3.50 to 3.90 km/sec there is a unique dispersion curve independent of path.

However, in the velocity range 2.90 - 3.5 km/sec (periods of 20-35 sec), there are indications that real differences may exist between the true dispersion curves in Figures 2 and 3. In this velocity range we estimated, for the purposes of this study, an average dispersion curve.

Using group velocity as the independent variable the data for each event were grouped into cells of width 0.5 km/sec. Within each cell the data were ordered according to period value and the sample median was computed. The cell midpoint

velocities and median periods were stored as data pairs. The sample median was chosen as a measure of central tendency because it is more efficient than the sample mean in the presence of outliers (Dixon, 1953)

In the velocity range 3.50 to 4.00 km/sec the sample median periods are observations on a single curve; therefore, adjacent points are related and a smoothing operator should improve the results. Furthermore, in the velocity range 2.90 to 3.50 km/sec only a representative smooth curve was desired, and a three point moving average operator was applied to the sample period values. The operator is given by

$$\text{Period}(1) = X(1)$$

$$\text{Period}(\text{Num}) = 1/2 \cdot X(\text{Num}-1) + 1/2 \cdot X(\text{Num})$$

$$\text{Period}(i) = 1/4 \cdot X(i-1) + 1/2 \cdot X(i) + 1/4 \cdot X(i+1)$$

where $1 = 2, \ldots, \text{Num}-1$

1 = the index of the cell with the largest velocity

Num = the index of the cell with the smallest velocity

$X(i)$ = the sample median period of cell i

Period (i) = the smoothed period of cell i.

The resulting dispersion curves for the four events (Figures 2 and 3) are shown in Figure 4. The smoothed curves show the same results as the original zero crossing data. That is, the curves are not statistically different in the velocity range 3.50 to 3.90 km/sec, and, in the range 2.90 to 3.50 km/sec, the smoothed curves indicate that the actual paths do not produce markedly different dispersions curves at these short periods.

In view of the similarity of the curves we combined the data from the four events and estimated a composite group velocity dispersion curve shown in Figure 5. Also shown in this figure is the continental dispersion curve compiled by Oliver (1962); the long dashed lines indicate bounds of the expected scatter under normal observational conditions. The composite curve can be seen to fall within the error bounds. Furthermore, the composite curve is in good agreement with the results of Ewing and Press (1956) who reported a group velocity of about 3.9 km/sec at a period of 75 sec. The smoothed data points are given in tabular form in Table 2.

CHIRP FILTER CONSTRUCTION

We have shown that, for our seismograph station in north Texas, we can assume a single group velocity dispersion curve for the continental path over the pole. We can then design "matched", or chirp, filters to aid in the detection of surface waves from small earthquakes traversing the same path.

A program was written which produced a sine wave that decreased in period with time, the dispersion being a function of epicentral distance. Such waveforms have been given the name "chirp" in radar technology. In this case the information used to distance - function were from Table 2. The following assumptions were made:

(i) the first arriving energy is at the maximum period observed, and

(ii) between the data points of Table 2 the dispersion curve is linear.

With these assumptions we obtained, by simple algebraic manipulations,

$$TT_i = \Delta / V_i \text{ and } T_o = TT_i - P_{1/2},$$

and for the ith linear segment

$$w_i(t) = \frac{2\pi (t+T_o)(1/TT_{i-1} - 1/TT_i)}{[P_{i-1} - P_i - (P_{i-1}/TT_i - P_i/TT_{i-1})(t+T_o)]},$$

where $(T_{i-1} - T_o) \leq t \leq (T_i - T_o)$,

$w_i(t)$ = frequency in radians for the t th time,

P_i = the i th period in sec,

TT_i = the i th travel time in sec,

i = 1, 2, ..., Num.

The dispersed sine wave computations were given by

$$AMP(k) = \sin [w_i(t) \cdot k + \rho_i],$$

where $k = 1, 2, \ldots, N_i$

N_i = the number of data points in the i th segment

ρ_i = phase shift of the i th segment

AMP(k) = the dispersed sine wave amplitude.

For k = 1 the segment was extrapolated to include time points back to T_0. For all other values of k only time points between the TT_i were included in a given segment.

The ρ_i were as follows

$$\rho_1 = 0$$

$$\rho_i = w_i(t_{max}) + \rho_{i-1},$$

for 1 = 2, 3, ..., Num, where t_{max} is the largest t value in the i th segment. Also

$$t = k + TT_{i-1}$$

so that

$$t_{max} = N_i + TT_{i-1}.$$

In each linear segment the frequency was a function of time given by $w_i(t)$. The origin of the sine wave was taken as zero, which gave the time shift between t and k. The phase shift ρ_i ensured a smooth transition from segment to segment.

In Figure 6 we show the dispersed sine wave for one of the events used in calculating the composite dispersion curve (Figure 5). These sinusoids indicate the effects of differences in epicentral distance; for the Sinkiang Province event ($\Delta = 107.6^{\circ}$) the first zero crossing occurs at about 72 sec and for the other three (Δ = approximately 60°) the first zero crossing occurs at about 68 sec. Similar period differences are evident throughout the curves.

Convolution of these dispersed sine waves, or chirp filters, with their respective signals should then produce

psuedo-autocorrelation functions. The results are not true autocorrelations because the sine waves have not been amplitude modulated; nor is the "true" dispersion given exactly by the composite dispersion curve.

APPLICATION OF THE CHIRP FILTER

The chirp filter constructed from the dispersion curve in Figure 5 was applied to four different sets of seismograms. First, it was convolved with the original seismograms used to construct the dispersion curve; second, with other events remote from the first four; third, as detector of surface waves with a low signal-to-noise ratio; and fourth, as a means of separating "mixed" Rayleigh waves.

In order to remove very long period energy each seismogram was filtered prior to being convolved with the chirp filter. The high-pass digital filter used had a corner at 50 sec and fell at 36 db/octave to a minimum at a period of 100 sec.

Figure 7 shows the application of the chirp filter to the time series for each of the events used in calculating the composite dispersion curve. In each example the lower trace shows the filter output, correctly aligned with the input time series. The auto-correlation-like nature of the output should be noted; the maximum peak of which should occur at the beginning of the Rayleigh wave energy. In each of the figures the data were plotted so that the largest excursion was full-scale; therefore, the improvement in signal-to-noise ratio

can be estimated by examining the reduction in noise.

Three other events were selected (table 3) with similar continental polar surface wave paths to Texas; however, their epicenters were remote from those given in table 1. The results of convolving these seismograms with the same chirp filter used previously are shown in figure 8. The outputs clearly show that the filter is effective for widely separated sources.

Figure 9 shows the results of convolving the chirp filter with seismograms in which the surface waves are barely discernible. This figure shows a seismogram from a small event ($m_b = 4.7$) at a depth of 110 km in the Hindu-Kush; convolution clearly emphasized the start of the surface waves.

Mixed Rayleigh waves resulting either from multiple sources close together or from reflections, or from multi-pathing are very difficult to separate, even when data from large arrays are avialable. However, if the arrivals are separated by times greater than about 50 sec, the chirp filter technique can be useful in separating the arrivals. Figure 10(a) (lower trace) shows the filtered output for a small event from the region of the USSR-Mongolia border;

two and, possibly, three Rayleigh wave arrivals can be seen on the filtered trace. The first and largest of these arrivals occurs precisely at the expected arrival time of the fundamental Rayleigh wave for this event. A fairly large earthquake (m_b = 5.9) sparked an earthquake swarm from this region of the USSR-Mongolia border in May 1970. Another earthquake from the swarm is shown in figure 10(b); again convolution detected two arrivals. All available seismograms of earthquakes in the swarm were processed but only three showed multiple detections of surface waves.

DISCUSSION

We have described above a new approach to the "peak and trough" method of surface wave analysis which has been used to determine group velocity dispersion curves. The machine measurements proved to be at least as good as those of an experienced analyst, and could be produced much faster.

A further advan'age was gained in the present analysis from the special properties of the seismograph system. Many previous surface wave studies have used data from the World-Wide Standard Seismograph Network recordings in which the peak period of the calibration response is at 20 sec. In our systems, the peak response proved to lie within the "stable"portion of the group velocity dispersion curve.

This type of analysis, while being quick and computationally easy, nevertheless has its problems. Any non-least-time arrivals will impair the estimation of the dispersion curve; the technique does not give as much information as that of Dziewonski et al. (1969), which places a restriction on the use of the method.

Nevertheless, by carefully selecting events with a large signal-to-noise ratio, and with an absence of either higher modes or very long period surface waves, it has been

shown that a single fundamental group velocity dispersion curve can be calculated for a continental path over the pole to the central United States. This claim can be further substantiated by the fact that a chirp filter, constructed from this fundamental dispersion curve, proved effective for events from a region extending from southern USSR and northern China to the Arctic Ocean.

In addition to the events mentioned in the previous sections of this paper, seismograms from the other events listed in table 3 were processed. In some cases the auto-correlations displayed low signal-to-noise ratios, but in every search for an event reported by NOAA, an event was detected; unreported events were also detected. Thus further study is required to determine operational detection thresholds and false alarm rates.

CONCLUSIONS

In view of the results reported here it might be appropriate to suggest a reason for the stability of the group velocity dispersion curve, particularly at the longer periods, on a continental path over the pole.

It has been shown in recent years (e.g. Roy et al. 1972) that the western United States, known structurally as the Basin and Range Province, is characterized by high temperatures in the lower crust and upper mantle. This region, which is known to extend up the western part of Canada, is also a poor transmitter of long period surface waves. A particularly good example of this phenomenum can be seen in figure 11. The Greenland Sea event (table 1), as recorded at Grand Saline, is compared to the same event recorded at Queen Creek, Arizona. This station (Fix and Sherwin, 1970) is located in the heart of the Basin and Range Province. The gains of the seismographs at the two stations were equalized at 50 sec, but it will be seen that the longer period surface waves are virtually missing at the Queen Creek site.

To the east the continental United States are characterized by the Atlantic and Gulf coastal plains. Furthermore, the central plains are known to have relatively low temperatures

in the lower crust and upper mantle (Roy, et al., 1968, Combs and Simmons, 1973) which provides an exceptionally good path for Rayleigh waves with periods from 20-75 sec. Our detection station in north Texas is, essentially, at the southern end of a surface wave guide which passes over the north pole (Figure 12).

The analog plots of the seismograms used in the study were analysed, after they had been high-pass filtered, for the presence of detectable Rayleigh waves. Using the formula

$$M_s = \log \left(\frac{A}{T}\right) + 1.66 \log \Delta - 0{\cdot}18, \text{ which}$$

can be easily derived (Gutenberg, 1945), values of M_s were found where A is the peak-to-peak amplitude, in mμ, of the surface wave at a period of T=20 sec, and Δ is the distance from epicenter to detector, in degrees. The results of these computations are given in tables 1 and 3, where the values of M_s are compared to the values of m_b determined by NOAA.

Using the data presented in this study an interim detection threshold has been determined for our Grand Saline recording station. For events travelling within the polar waveguide this threshold is at $M_s = 3{\cdot}5$, for a single vertical seismometer, which is equivalent to a threshold of $m_b = 4{\cdot}5$ for events at depths of less than 50 km.

ACKNOWLEDGEMENTS

Nancy Cunningham was responsible for much of the software developments used in this research, Frank P. Van Leer was responsible for the initial seismic analysis. The research was supported by the Air Force Office of Scientific Research under Grant No. 71-2133B.

REFERENCES

Bloch, S. and A. L. Hales (1969). New techniques for the determination of surface wave phase velocities, Bull. Seism. Soc. Am. 58, 1021-1034.

Combs, J. and G. Simmons, Terrestial heat flow determinations in north central United States, J. Geophys. Res., 78, 441-461, 1973.

Dixon, W. J. (1953). Processing data for outliers, Biometrics 9, 74-89.

Dziewonski, A., M. Landisman, S. Bloch, Y. Sato and S. Asano (1968). Progress report on recent improvements in the analysis of surface wave observations, Journal of Physics of the Earth, Special Issue 16, 1-26.

Dziewonski, A., S. Bloch and M. Landisman (1969). A technique for the analysis of transient seismic signals, Bull. Seism. Soc. Am. 59, 427-444.

Ewing, Maurice and Frank Press (1952). Crustal structure and surface wave dispersion, pt. 2, Bull. Seism. Soc. Am. 42, 315-325.

Ewing, Maurice and Frank Press (1956). Rayleigh wave dispersion in the period range 10 to 500 seconds, Trans. Am. Geophys. Union 37, 213-215.

Fix, J. E. and J. R. Sherwin, A high-sensitivity strain/inertial seismograph installation, Bull. Seis. Soc. Am., 60, 180-3-1822, 1970.

Gutenberg, B., Amplitudes of surface waves and magnitudes of shallow earthquakes, Bull. Seis. Soc. Am., 35, 3-12, 1945.

Herrin, Eugene, William Tucker, James Taggart, David W. Gordon and John L. Lobdell (1968). Estimation of surface focus P travel times, Bull. Seism. Soc. Am. 58, 1273-1291.

Herrin, Eugene and John A. McDonald (1971). A digital system for the acquisition and processing of geoacoustic data, Geophys. J. R. Astr. Soc. 26, 13-20.

Landisman, M. A., A. Dgiewonski and Y. Sato (1969). Recent improvements in the Analysis of surface wave observations, Geophys. J. R. Astr. Soc. 17, 369-403.

Oliver, Jack (1962). A summary of observed seismic surface wave dispersion, Bull. Seism. Soc. Am. 52, 81-86.

Roy, R. F., E. R. Decker, D. D. Blackwell and F. Birch, Heat flow in the United States. J. Geophys. Res., 73, 5207-5221, 1968.

Roy, R. F., D. D. Blackwell and E. R. Decker (1972). Continental heat flow, in Nature of the Solid Earth, ed. E. C. Robertson, McGraw-Hill, New York, 506-543.

Sato, Y. (1955). Analysis of dispersed surface waves by means of Fourier Transform 1, Bull. Earthquake Res. Inst., Tokyo Univ., Part 1, 33, 33-47.

Sorrells, G. G., John A. McDonald, Z. A. Der and Eugene Herrin (1971). Earth motion caused by local atmospheric pressure changes, Geophys. J. R. Astr. Soc. 26, 83-98.

Tucker, William, Eugene Herrin and Helen W. Freedman (1968). Some statistical aspects of the estimation of seismic travel times, Bull. Seism. Soc. Am. 58, 1243-1260.

FIGURE CAPTIONS

1. Response of the seismograph system.

2. Rayleigh wave dispersion information recorded in north Texas for three events (see table 1), (a) North of Svalbard, (b) Greenland Sea, (c) Norwegian Sea.

3. Rayleigh wave dispersion information recorded in north Texas for an event in Sinkiang Province (see table 1).

4. Rayleigh wave dispersion curves for the four events in table 1 after smoothing (a) North of Svalbard (b) Greenland Sea (c) Norwegian Sea (d) Sinkiang Province.

5. Composite Rayleigh wave dispersion curve for the four events in table 1 in conjunction with continental dispersion curve due to Oliver (1962).

6. Typical dispersed sine wave, or chirp filter, derived from the dispersion curve shown in figure 4 (b).

7. Convolution of the chirp filter derived from the curve in figure 5 with each of the four events given in table 1, (a) North of Svalbard, (b) Greenland Sea (c) Norwegian Sea (d) Sinkiang Province.

8. Convolution of the chirp filter derived from the curve in figure 5 with three of the events given in table 3: events from very different locations.

9. Convolution of the chirp filter derived from the curve in figure 5 with an event from the Hindu-Kush (table 3) in which surface waves are barely discernible.

10. Convolution of filter and surface waves showing two, or possibly, three surface wave arrivals (a) USSR Mongolian border on 17 May 1970, m_b = 4.5, (b) USSR - Mongolian border on 23 May 1970, m_b = 4.5. (See table 3 for details).

11. Comparison of the surface waves from the Greenland Sea event (table 1) recorded at (a) Queen Creek, Arizona, (b) Grand Saline, Texas.

12. A polar plot of the world centered on Grand Saline. The locations of the epicenters of the events used in this study are shown; the alphanumeric designation refers to tables 1 and 3.

TABLE CAPTIONS

1. Data for the four events used to calculate the composite dispersion curve shown in figure 5.
2. Coordinates of the points used to plot the curve in figure 5.
3. Data for the other events used in this study.

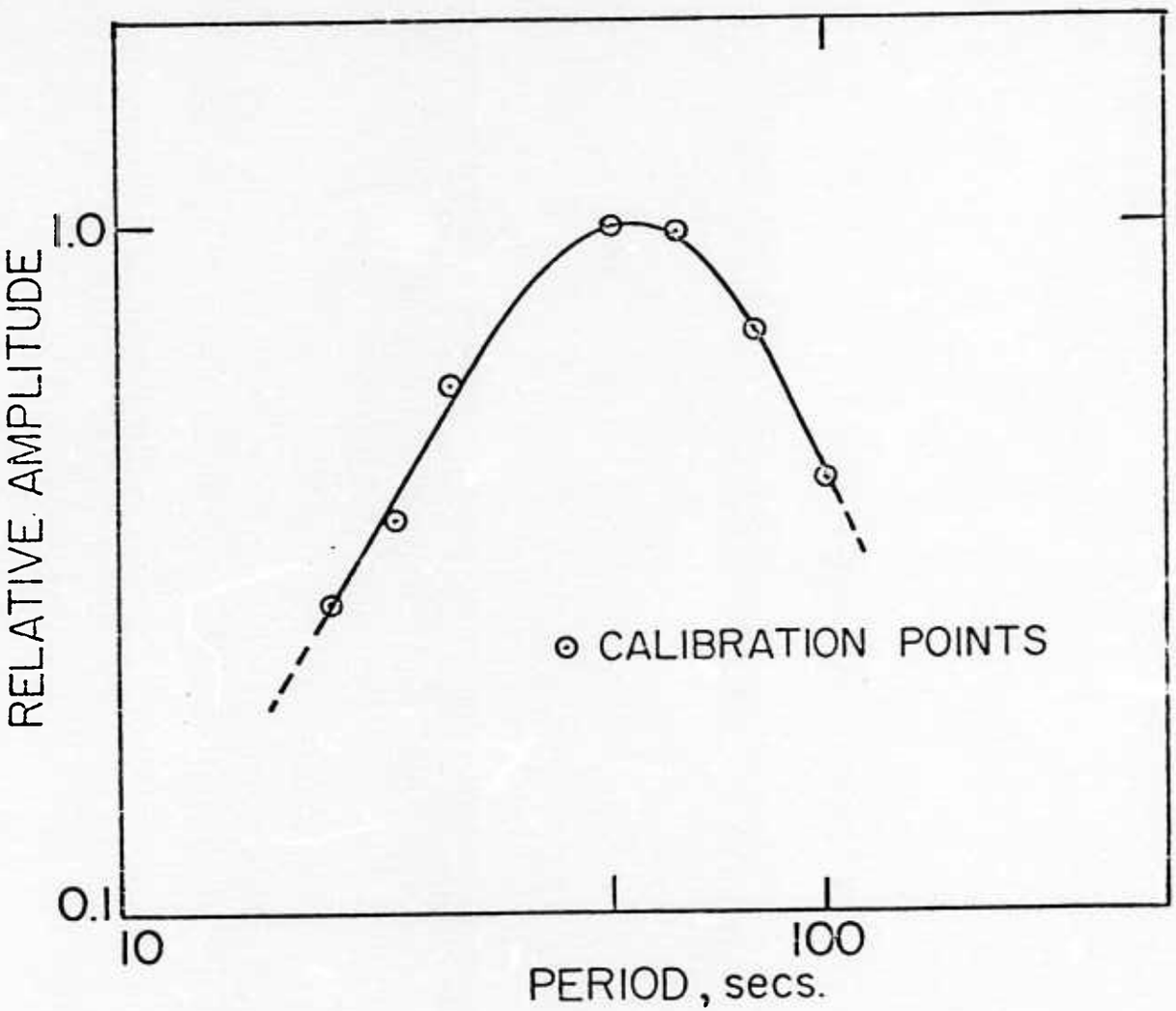
RELATIVE AMPLITUDE
1.0
0.1
10
100
PERIOD, secs.
⊙ CALIBRATION POINTS

Figure 1

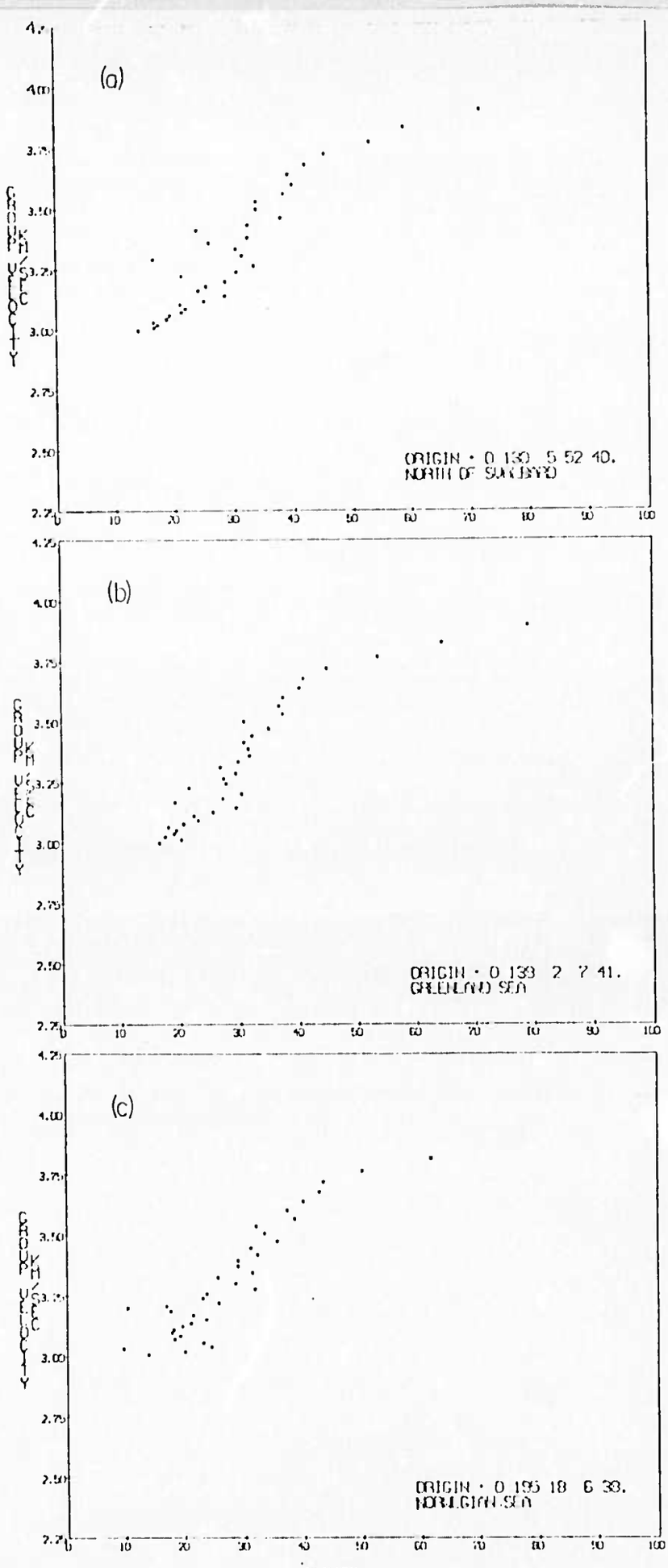
(a)
ORIGIN - 0 130 5 52 40.
NORTH OF SHETLAND
(b)
ORIGIN - 0 133 2 7 41.
GREENLAND SEA
(c)
ORIGIN - 0 195 18 6 38.
NORWEGIAN SEA
GROUP VELOCITY KM/SEC
PERIOD SEC

Figure 2

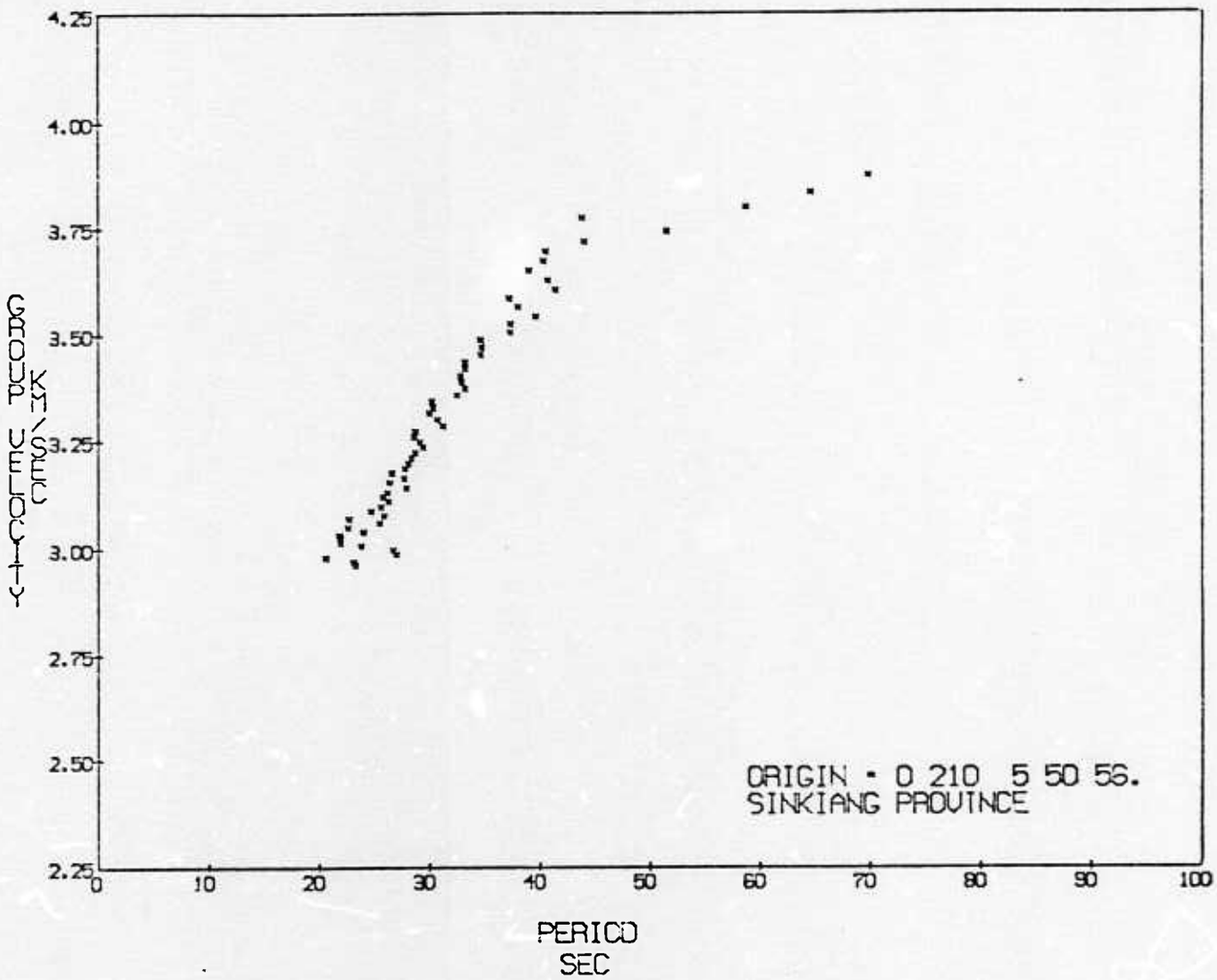
4.25
4.00
3.75
3.50
3.25
3.00
2.75
2.50
2.25
GROUP VELOCITY KM/SEC
0
10
20
30
40
50
60
70
80
90
100
PERIOD SEC
ORIGIN - 0 210 5 50 56.
SINKIANG PROVINCE

Figure 3

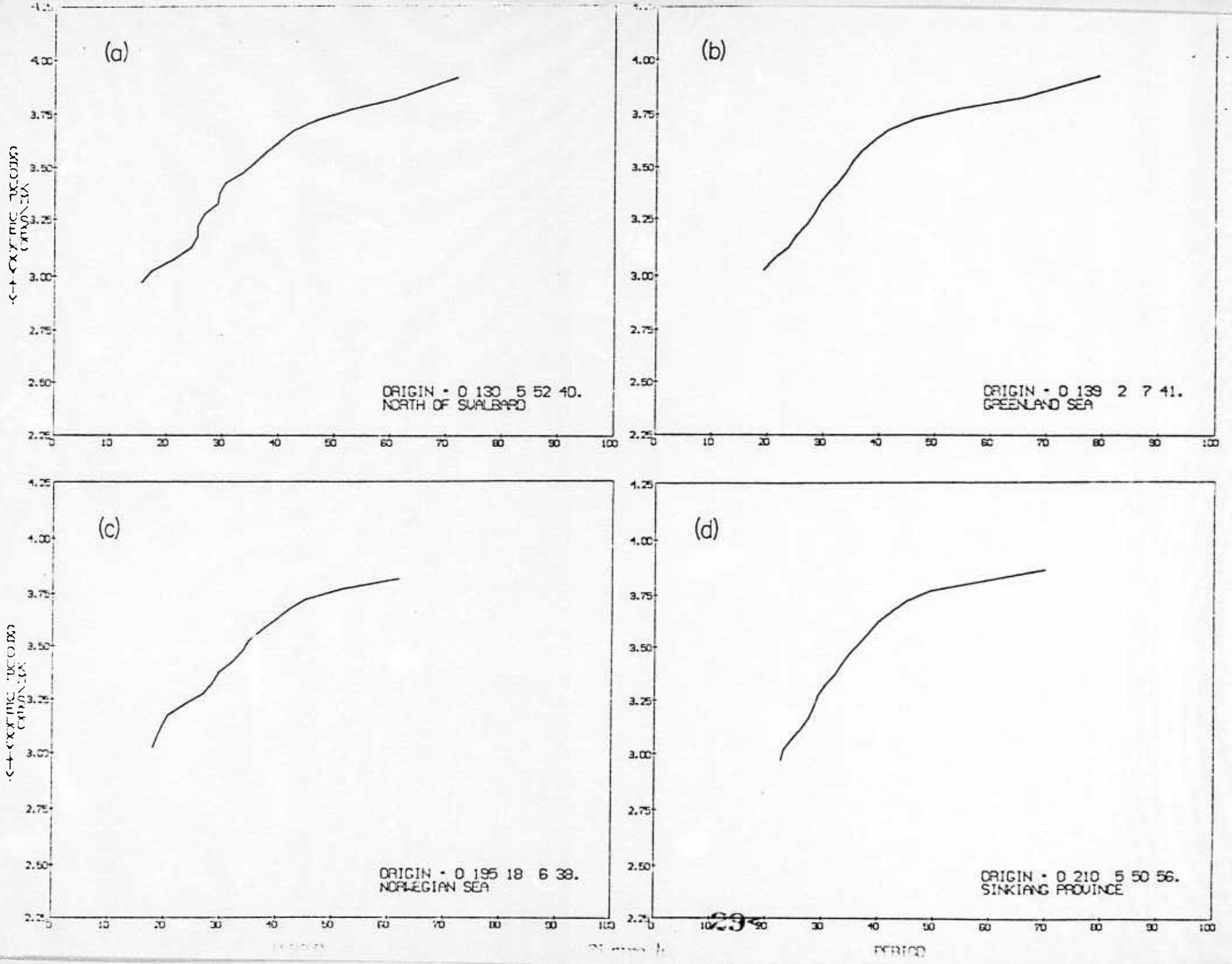
(a)
ORIGIN = 0 130 5 52 40.
NORTH OF SVALBARD
(b)
ORIGIN = 0 139 2 7 41.
GREENLAND SEA
(c)
ORIGIN = 0 195 18 6 38.
NORWEGIAN SEA
(d)
ORIGIN = 0 210 5 50 56.
SINKIANG PROVINCE
PERIOD

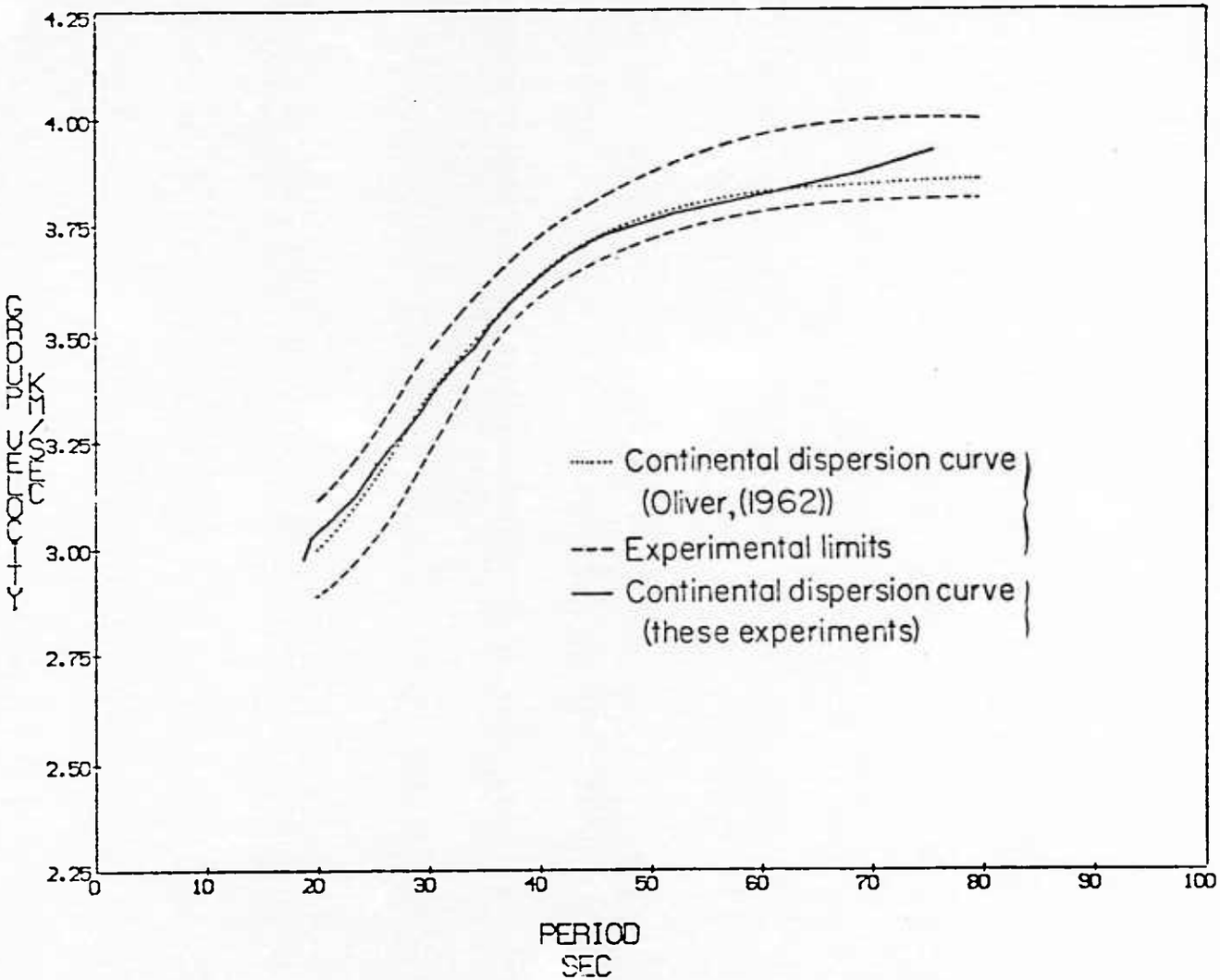
4.25
4.00
3.75
3.50
3.25
3.00
2.75
2.50
2.25
0
10
20
30
40
50
60
70
80
90
100
GROUP VELOCITY KM/SEC
PERIOD SEC
Continental dispersion curve (Oliver,(1962))
Experimental limits
Continental dispersion curve (these experiments)

Figure 5

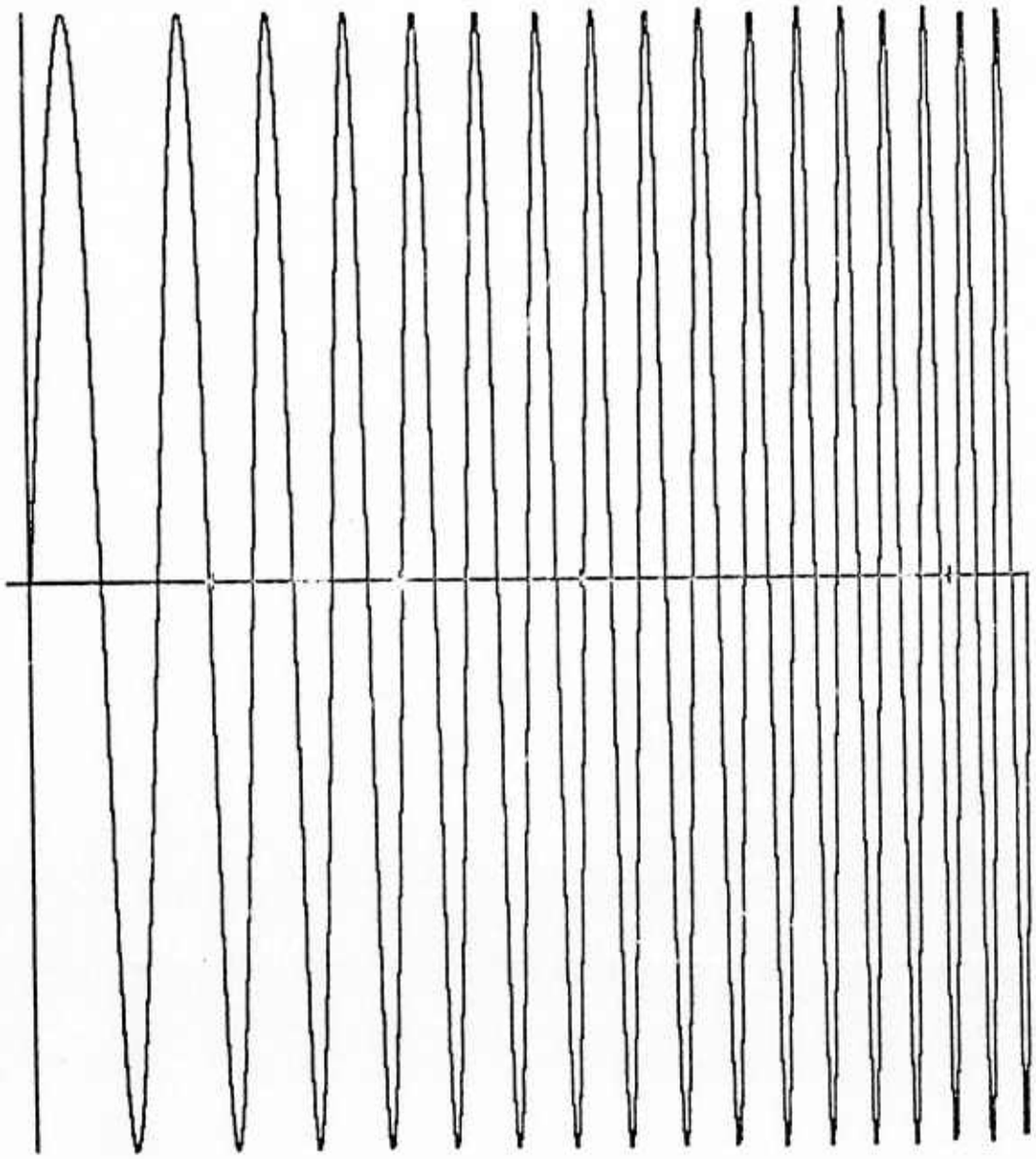

DISPERSED SINE WAVE
GREENLAND SEA
DELTA = 59.70
TICK MARKS EVERY 100 SEC

Figure 6

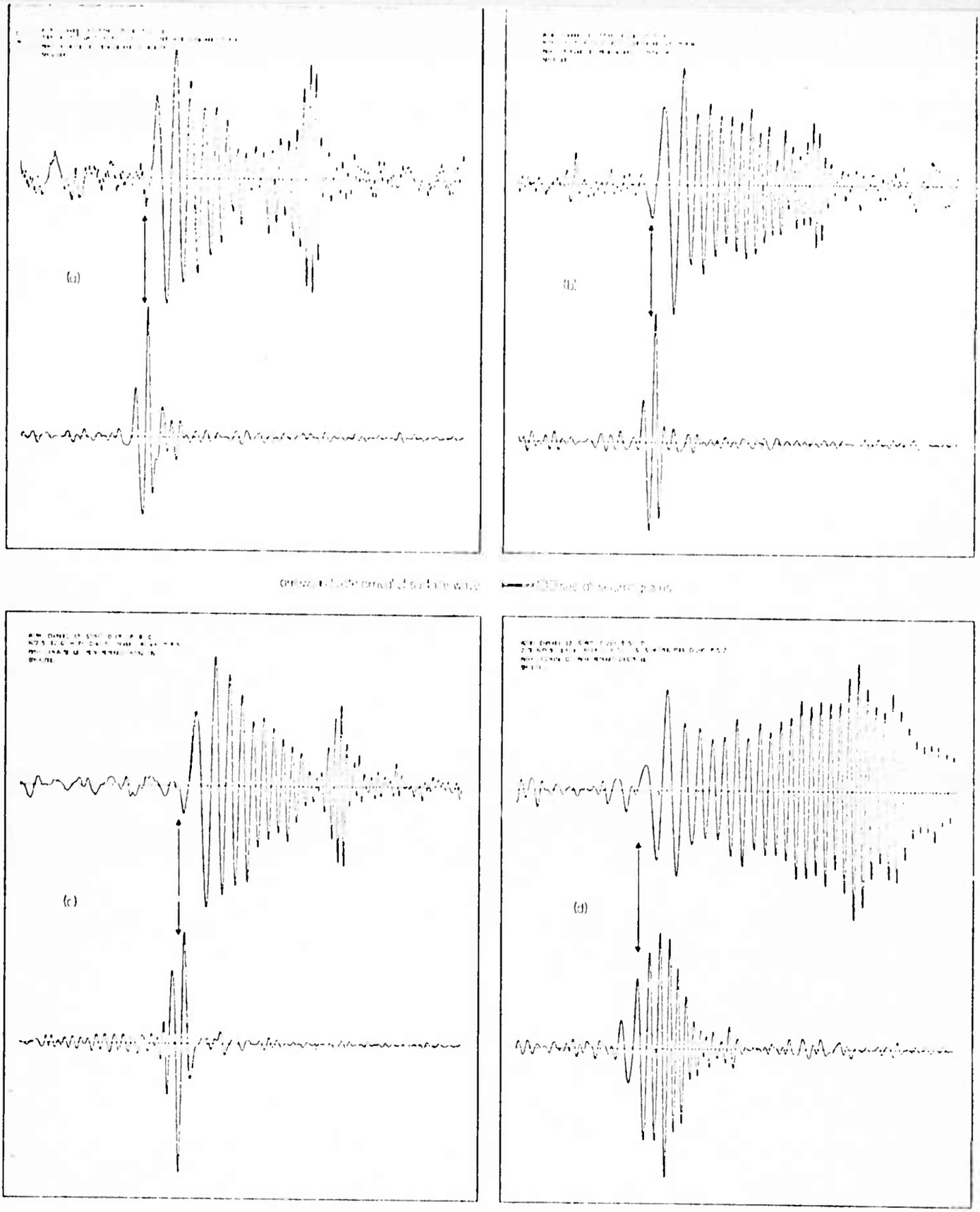

Figure 7

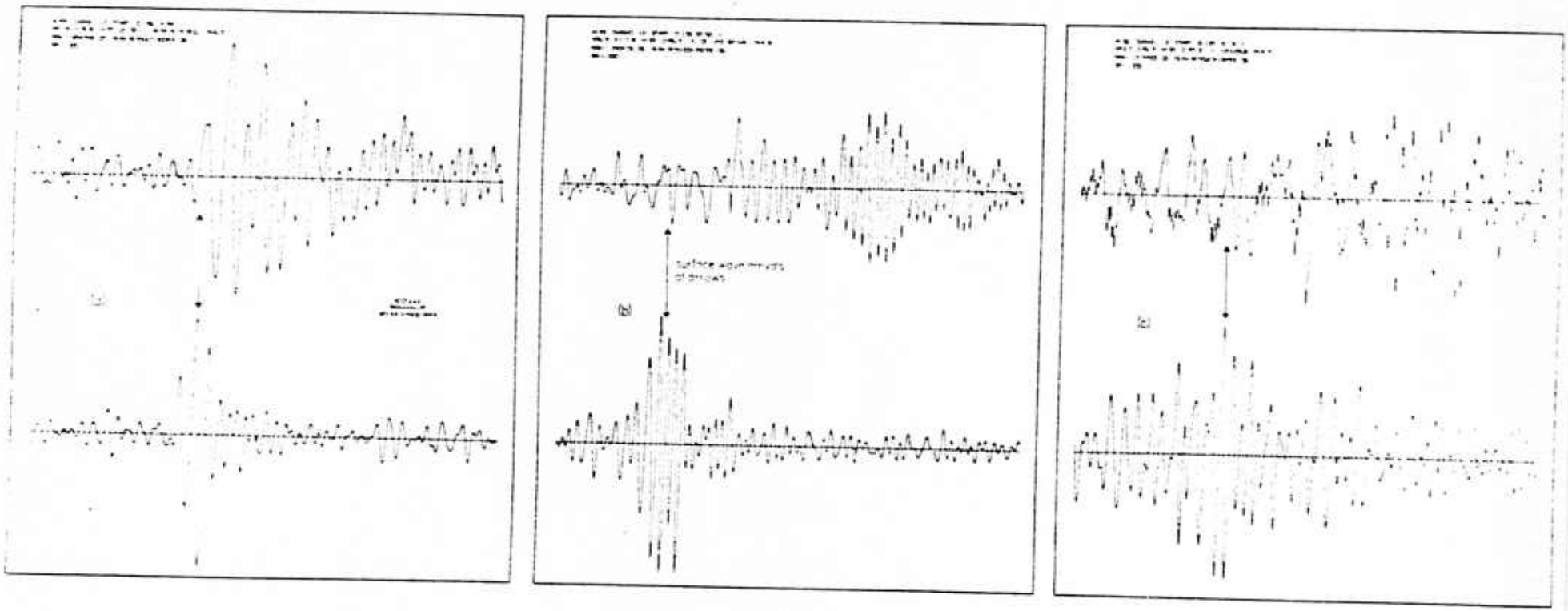

Figure 8

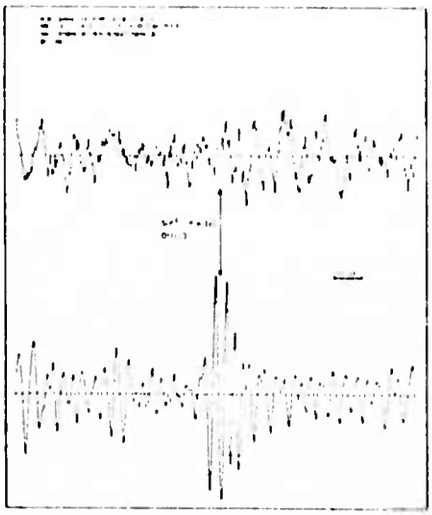

Figure 9

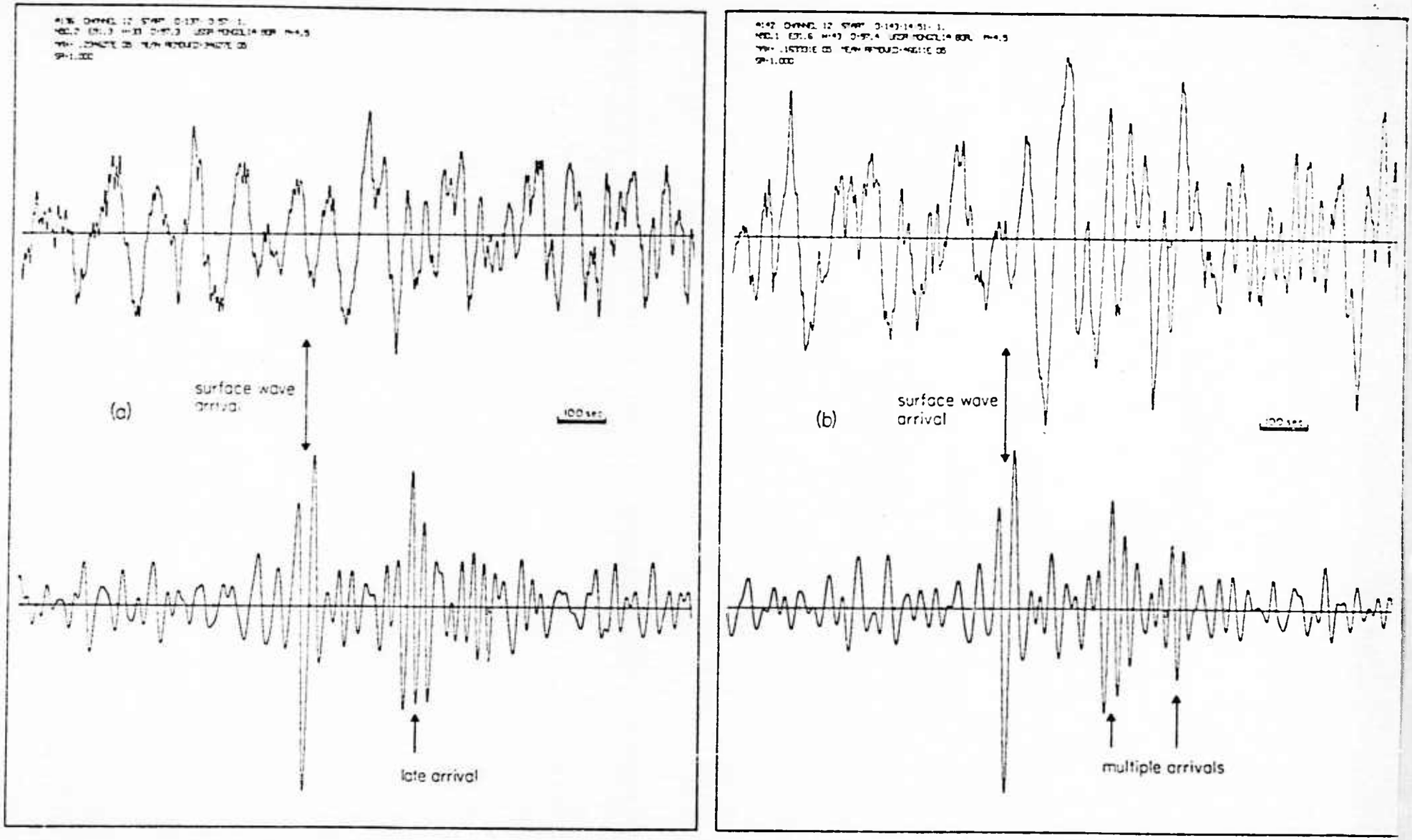
(a)
surface wave arrival
late arrival
(b)
surface wave arrival
multiple arrivals

Figure 10

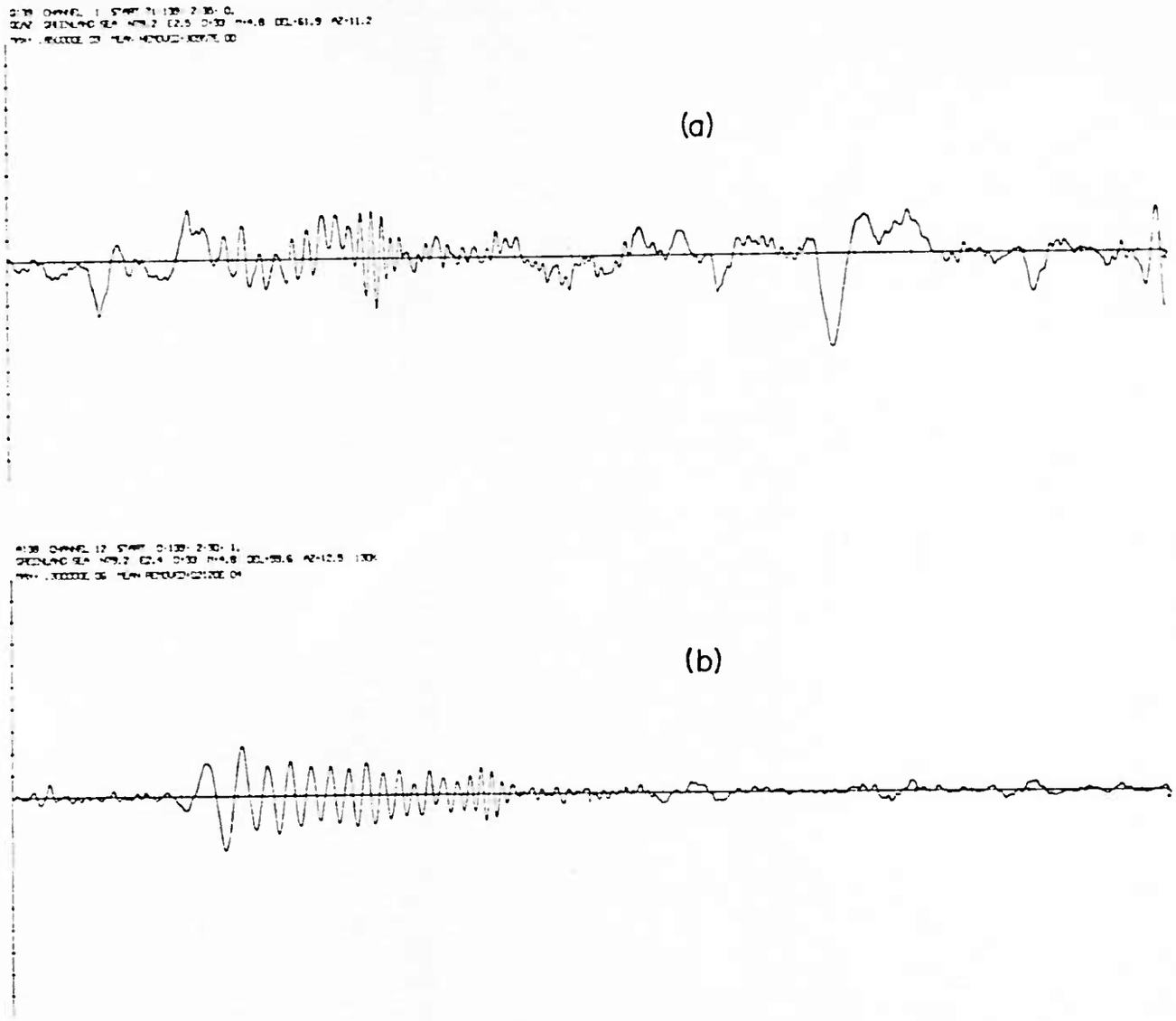

Figure 11

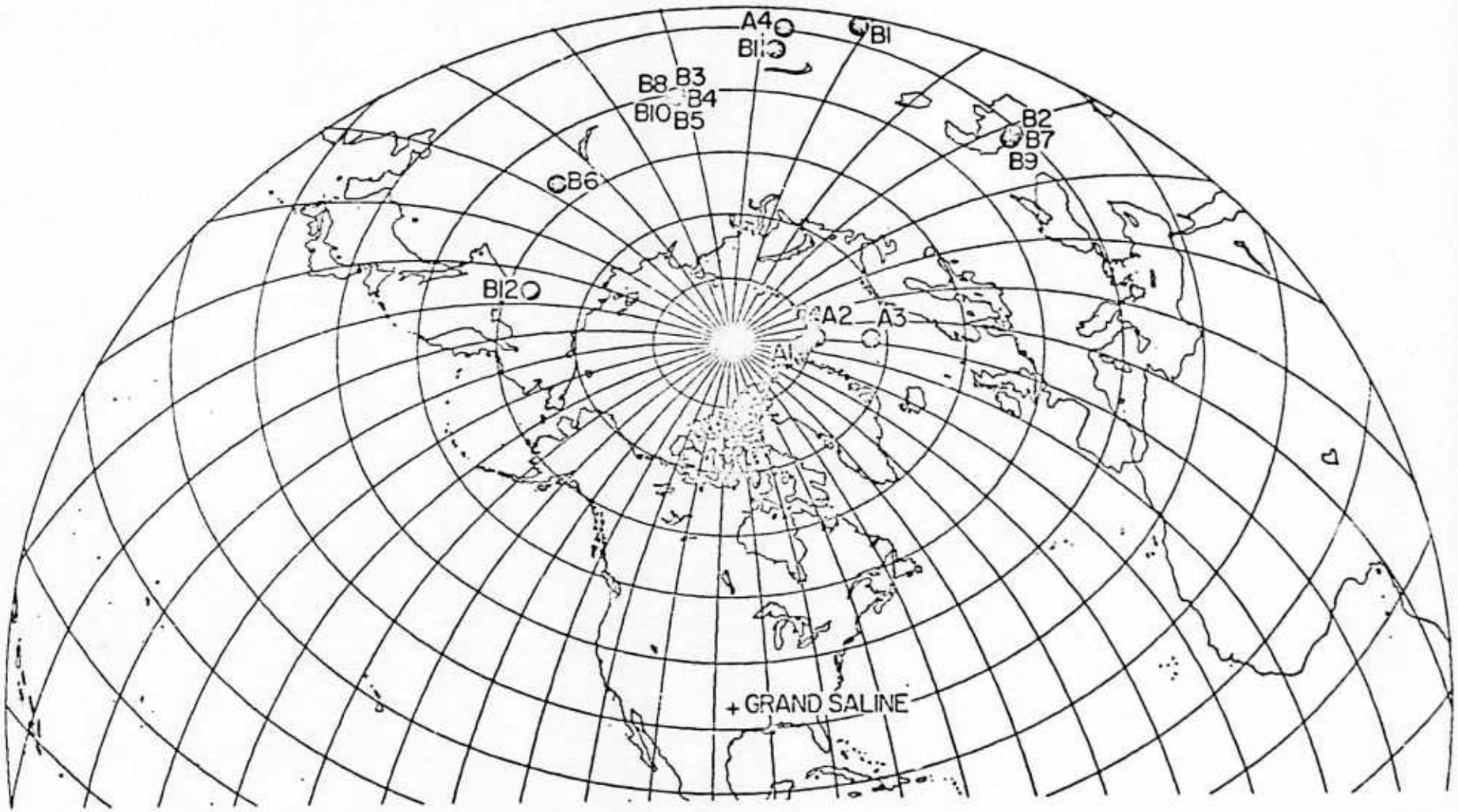

Figure 12

TABLE 1

Geographic Location	Origin Time[1]			Lat.[1]	Long.[1]	Depth[1]	m_b[1]	M_s[2]	Δ[3]	Azimuth[3]
	Year	Day	Time	deg	deg	Km			deg	deg
A1. N. of Svalbard	70	130	055240·2	81.5N	4.7W	33	4.4	4.0	58.1	10.1
A2. Greenland Sea	70	139	020741.5	79.2N	2.5E	33	4.8	3.7	59.7	12.5
A3. Norwegian Sea	70	195	180637.8	72.5N	2.0E	33	4.9	3.9	61.5	20.0
A4. S. Sinkiang Prov.	70	210	055056.4	39.9N	77.8E	13	5.2	5.4	107.6	5.2

1. From NOAA PDE cards

2. Calculated from Gutenberg (1945) using calculated Δ

3. Calculated from coordinates of epicenter and of recording station:

Grand Saline Texas 32° 39' 19" N)
95° 42' 10" W)

(Same footnotes apply to table 3.)

TABLE 2

Group Velocity	Period
3.9250	75.5223
3.8750	69.2352
3.8250	60.8679
3.7750	51.8606
3.7250	45.6151
3.6750	41.9743
3.6250	39.5603
3.5750	37.4096
3.5250	35.5422
3.4750	34.0502
3.4250	32.0733
3.3750	30.5458
3.3250	29.3486
3.2750	27.7666
3.2250	26.1123
3.1750	24.6726
3.1250	23.4360
3.0750	21.3606
3.0250	19.2884
2.9750	18.6214

TABLE 3

	Geographic Location	Origin Time Year - Day - Time GMT	Lat[1] deg	Long[1] deg	Depth[1] km	M_b[1]	M_s[2]	Δ[3] deg	Azimuth deg
B1.	Hindu-Kush	70-130-123233.3	36.1N	71.1E	121	4.7	?	110.5	11.4
B2.	E. Caucasus	70-135-061916.6	43.1N	47.3E	33	4.5	3.2	97.4	26.4
B3.	USSR-Mongolia Bd.	70-135-171315.1	50.2N	91.3E	33	5.9	5.7	97.3	355.5
B4.	USSR-Mongolia Bd.	70-135-185007.4	50.3N	91.2E	33	4.6	4.9	97.2	355.5
B5.	USSR-Mongolia Bd.	70-135-201216.9	50.2N	91.3E	33	5.0	4.3	97.3	355.5
B6.	E. Lake Baikal	70-135-205012.7	56.8N	117.8E	33	4.9	4.3	86.5	342.3
B7.	E. Caucasus	70-136-104323.0	42.9N	47.1E	33	4.4	3.3	97.4	26.6
B8.	USSR-Mongolia Bd.	70-137-005648.0	50.2N	91.3E	33	4.5	3.4	97.3	355.5
B9.	E. Caucasus	70-137-050217.7	43.0N	46.9E	33	4.7	3.4	97.3	26.7
B10.	USSR-Mongolia Bd.	70-143-145134.6	50.1N	91.6E	43	4.5	3.4	97.4	355.3
B11.	Alma-Alta Rgn.	70-156-045306.4	42.5N	78.8E	20	6.0	5.7	105.1	4.2
B12.	E. Siberia	70-156-103154.3	63.4N	146.2E	33	5.5	4.5	72.5	335.4

(For footnote see table 1)

TECHNICAL REPORT

to the

AIR FORCE OFFICE OF SCIENTIFIC RESEARCH

from

Eugene Herrin
and
William Tucker

Dallas Geophysical Laboratory
Southern Methodist University
Dallas, Texas 75222

ARPA Order Number: 1827-1
Program Code: 2F10
Name of Contractor: Southern Methodist University
Effective Date of Grant: July 1, 1971
Grant Expiration Date: June 30, 1973
Amount of Grant Dollars: $179,739
Grant Number: 71-2133B
Principal Investigator and Phone Number: Eugene Herrin
214 692-2760
Program Manager and Phone Number: Truman F. Cook, Director of
Research Administration
214 692-2031
Title of Work: Identification of Earthquakes and Underground
Explosions
University Account Number: 80-46

Sponsored by
Advanced Research Projects Agency
ARPA Order No. 1827-1

ON THE ESTIMATION OF BODY WAVE MAGNITUDES

Eugene Herrin and William Tucker

Dallas Seismological Observatory
Southern Methodist University
D[illegible], Texas 75222

October 1972

ABSTRACT

Observations from any seismological network lead to overestimation of the magnitude of seismic events which are near the detection threshold of that network. Methods are presented for calculating this magnitude bias. Consideration must be given to this effect in comparing networks with significantly different thresholds, in comparing theoretical and empirical estimates of network capability and in determining the source energy of small seismic events.

INTRODUCTION

Body wave magnitude was first defined by Gutenberg (1945 a,b), and his distance and focal depth normalization factors are still in general use. Recently Veith and Clawson (1972), based on a large quantity of data from explosions and earthquakes, have revised these normalization factors. In this paper we assume that the calculations required to obtain magnitudes have been made correctly, that the depth-distance corrections are exact and that there are no gross errors in the observations. We are primarily concerned with problems which arise in the determination of magnitudes for small seismic events which are near the detection limit of the observing network.

Freedman (1967) showed that the individual observations of amplitude divided by period (A/T) used in the estimation of magnitude for a given event tend to be log-normally distributed; thus, the values of log A/T are approximately normally distributed. She concluded that the mean of the magnitudes determined by each station should be used to characterize the source strength of a given event. Freedman worked with large events, however, and was not concerned with the problem of missing data. In the following discussions we define the "true" magnitude of an

event to be the mean of the individual magnitudes as observed by stations in a "perfect network"; a "perfect network" is one for which the probability of each station observing the P-wave from the event is essentally unity.

DISTRIBUTION OF OBSERVED MAGNITUDES

Mack (1969) showed that surprisingly large variations in amplitude were observed among the elements of LASA for the first arriving P-waves from any given event. He attributed this variation to a multipath phenomenon. We have investigated the variation in magnitude estimates which would arise from the multipath effect proposed by Mack.

We assumed an observed signal to be S(t) where

$$S(t) = S_1(t) + a S_1(t+\tau_2) + b S_1(t+\tau_2+\tau_3) \qquad (1)$$

$S_1(t)$ is the LASA summation, properly phased, for a presumed explosion on April 21, 1966, in East Kazahkstan, U.S.S.R. (figure 1). S(t) was computed and plotted for:

a = 0.2, 0.4, ... , 1.0

b = 0.2, 0.4, ... , 1.0

τ_2 = 0, 0.1, 0.2, ... , 0.9 sec.

τ_3 = 0, 0.1, 0.2, ... , 0.9 sec.

We also plotted

$$S(t) = S_1(t) + c S_1(t+\tau_4) \qquad (2)$$

for $c = 0.2, 0.4, \ldots, 1.0$ and

$\tau_4 = 0, 0.1, 0.2, \ldots, 1.8$ sec.

These combinations, plus $S_1(t)$, provided 2596 signals. The peak-to-peak amplitude (A) and the period (T) were read for the maximum peak-to-peak excursion in the first 5 sec. of each signal, according to the method used by analysts reporting LRSM, WMO, BMO, CPO, UBO and TFO data. Histograms for the observed values of A/T and log A/T are shown in figures 2 and 3. These histograms should be compared with figures 1 and 2 in Freedman (1967). The variation in signal amplitude seen in this study simulates the effects to be expected from multipath phenomena of the kind suggested by Mack (1969). The variations of A/T tend to be log-normally distributed; multipath effects may, in part, explain the empirical results reported by Freedman (1967).

In the following sections we have assumed that the individual observations of magnitude for an event are normally and independently distributed. In our simulation study the standard deviation, for 2596 observations of magnitude, was 0.12 magnitude unit. Freedman (1967) reports a standard deviation (SD) for USCGS data of about 1/2 unit, and Mack (personal communication, 1972) reported a SD for LASA of about

1/3 unit. Veith and Clawson (1972) give values of SD of 0.356 for explosion data and 0.350 for earthquake data. We believe that the simulation studies give a low value of amplitude variability because only the effects of three combinations of a simple P-wave signal were considered. Thus reasonable limits for the SD of the magnitude distribution are 0.2 to 0.5 unit; a value of 0.35 magnitude unit has been used for the standard deviation in all calculations reported in this paper.

ESTIMATION OF MAGNITUDE FOR SMALL EVENTS

In any given network various stations will fail to detect and determine magnitudes for smaller events. We speak of a 90% body wave detection threshold as that magnitude for which there is a probability of 0.9 that at least n stations of the network will observe the initial P-wave, but only those stations observing the signal can report a magnitude.

Stonewall model - Figure 4(a, b, c) shows a simple model which illustrates the problem of estimating magnitudes for small events. In this model no station can observe a magnitude less than the stonewall value, m_d. As long as the "true" magnitude of the event, m_b, is large with respect to m_d (figure 4a), the expected value of the observed magnitude is the "true" value. When m_b approaches m_d (figure 4b) only those values of magnitude to the right of the stonewall can be observed by the network, thus the expected value of the observed magnitude, $E(\hat{m})$, is larger than the "true" value. The resulting bias increases with decreasing values of m_b. An extreme case is shown in figure 4c where the "true" magnitude is less than the stonewall value. Notice that the reported magnitude; i.e., the mean of the observed magnitudes, can never be less

than the stonewall magnitude, no matter how small the "true" value becomes.

The stonewall model is an obvious simplification of what really happens in a network, but it can be used to illustrate the effect with which we are concerned. The model describes an automated detection system using signals from a large array. In this case the distances from source to each element of the array are nearly the same and noise levels should not vary significantly among the elements. If a fixed threshold is used in the detection program, then the stonewall model is an accurate description of the process.

Random-wall model - A more useful model for the study of magnitude bias is one in which the location of the stonewall is a random variable; that is, we can only speak of the probability of the wall having a particular value for any given observation. The variability in location of the wall depends on such factors as differences in epicentral distances, in noise levels and in detection criteria. It is impractical to determine a priori, the distribution function for the random-wall. We have carried out the computations reported in the next sections for two distributions, the normal and the uniform. Conclusions are essentially the same for both cases; all of

the following equations and calculations assume a normal distribution function for the random-wall.

Terms are defined as follows:

M_b body wave magnitude - a normal random variable

m_b mean of M_b - "true" magnitude

σ_b standard deviation of M_b

M_d Random-wall - a normal random variable

m_d mean of Md

σ_d standard deviation of M_d

$\sigma^2 = \sigma_b^2 + \sigma_d^2$

$F_{k,l}$ is the cumulative F - distribution with k,l degrees of freedom

$P_{n,N}$ is the probability that at least n stations from a total of N stations detect an event with "true" magnitude m_b.

$\hat{m}$ magnitude observed by those stations that detect the event - a random variable

We define p as the probability of detection of an event by an individual station; thus

$p = Pr(M_b > M_d)$.

Letting $i = 2n$ and $j = 2(N-n+1)$ we have that (see appendix

for derivations)

$$P_{n,N} = F_{i,j}\left\{\frac{\frac{j}{i}p}{1-p}\right\} \qquad (3)$$

and

$$E(\hat{m}\,|\,n,N) = m_b + \frac{\sigma_b^2}{\sigma\sqrt{2\pi}}\exp\left[-\frac{1}{2}\left(\frac{m_d - m_b}{\sigma}\right)^2\right] \qquad (4)$$

The LHS in equation (4) is the conditional mean of m given that at least n of N stations in the network detected the event. The quantity $E(\hat{m}\,|\,n,N)$ is defined as the <u>apparent</u> magnitude of the event; the magnitude we would expect the network to report.

NUMERICAL RESULTS

Computer algorithms were written using equations (3) and (4). The first code gives the detection probability as a function of "true" magnitude. In equation (4) we see that the second term on the RHS is the magnitude bias. The computer code calculates the apparent or biased magnitude as a function of "true" magnitude.

In order to arrive at reasonable estimates of the standard deviation (σ_d) of M_d, the <u>random-wall</u> distribution, we must know something about the properties of the network. If we restrict epicentral distances to lie between 30 and 70 degrees the range of log A/T, from the distance effect alone is, according to Veith and Clawson (1972), about 0.2 magnitude unit. Noise at individual stations may well change in amplitude by a factor of two giving a variability in the detection threshold of about 0.3 magnitude unit. Clearly when $\sigma_d = 0$ we revert to the <u>stonewall model</u>. For the restricted network case we take $\sigma_d = 0.20$, a value which appears to allow for the expected variability. Tables 1 and 2 and figures 5 and 6 show calculations for two networks. The first is characteristic of the existing WWSSN with its 90% detection threshold reported to be about 4.5 magnitude units. The second is a

NETWORK PARAMETERS
MO = 4.40
N = 20
NO. DET = 4
SIGMA B = .3500
SIGMA D = .2000

TABLE 1

Magnitude bias and detection probability for WWSSN -- Restricted distance range

DETECTION PROBABILITY MB	PROB	NETWORK BIAS TRUE MB	EST MB
1.00000	.0000000	1.00000	3.5981580
1.05000	.0000000	1.05000	3.6109622
1.10000	.0000000	1.10000	3.6237803
1.15000	.0000000	1.15000	3.6366128
1.20000	.0000000	1.20000	3.6494604
1.25000	.0000000	1.25000	3.6623238
1.30000	.0000000	1.30000	3.6752035
1.35000	.0000000	1.35000	3.6881003
1.40000	.0000000	1.40000	3.7010150
1.45000	.0000000	1.45000	3.7139483
1.50000	.0000000	1.50000	3.7269012
1.55000	.0000000	1.55000	3.7398744
1.60000	.0000000	1.60000	3.7528690
1.65000	.0000000	1.65000	3.7658859
1.70000	.0000000	1.70000	3.7789263
1.75000	.0000000	1.75000	3.7919912
1.80000	.0000000	1.80000	3.8050819
1.85000	.0000000	1.85000	3.8181995
1.90000	.0000000	1.90000	3.8313456
1.95000	.0000000	1.95000	3.8445215
2.00000	.0000000	2.00000	3.8577287
2.05000	.0000000	2.05000	3.8709689
2.10000	.0000000	2.10000	3.8842437
2.15000	.0000000	2.15000	3.8975551
2.20000	.0000000	2.20000	3.9109048
2.25000	.0000000	2.25000	3.9242950
2.30000	.0000000	2.30000	3.9377276
2.35000	.0000000	2.35000	3.9512048
2.40000	.0000000	2.40000	3.9647288
2.45000	.0000000	2.45000	3.9783017
2.50000	.0000000	2.50000	3.9919255
2.55000	.0000000	2.55000	4.0056018
2.60000	.0000000	2.60000	4.0193317
2.65000	.0000000	2.65000	4.0331152
2.70000	.0000000	2.70000	4.0469506
2.75000	.0000000	2.75000	4.0608333
2.80000	.0000000	2.80000	4.0747540
2.85000	.0000000	2.85000	4.0888335
2.90000	.0000000	2.90000	4.1031538
2.95000	.0000001	2.95000	4.1175548
3.00000	.0000001	3.00000	4.1320454
3.05000	.0000002	3.05000	4.1466347
3.10000	.0000003	3.10000	4.1613326
3.15000	.0000006	3.15000	4.1761497
3.20000	.0000012	3.20000	4.1910972
3.25000	.0000026	3.25000	4.2061872
3.30000	.0000059	3.30000	4.2214326
3.35000	.0000140	3.35000	4.2368474
3.40000	.0000346	3.40000	4.2524465
3.45000	.0000879	3.45000	4.2682463

DETECTION PROBABILITY MB	PROB	NETWORK BIAS TRUE MB	EST MB
3.50000	.0002270	3.50000	4.2842642
3.55000	.0005879	3.55000	4.3005193
3.60000	.0015074	3.60000	4.3170322
3.65000	.0037713	3.65000	4.3338254
3.70000	.0090768	3.70000	4.3509234
3.75000	.0207290	3.75000	4.3683529
3.80000	.0443519	3.80000	4.3861430
3.85000	.0879273	3.85000	4.4043253
3.90000	.1600898	3.90000	4.4229346
3.95000	.2660748	3.95000	4.4420053
4.00000	.4026234	4.00000	4.4615875
4.05000	.5554633	4.05000	4.4817165
4.10000	.7028317	4.10000	4.5024431
4.15000	.8243254	4.15000	4.5238188
4.20000	.9094053	4.20000	4.5458986
4.25000	.9597181	4.25000	4.5687407
4.30000	.9847099	4.30000	4.5924064
4.35000	.9950872	4.35000	4.6169595
4.40000	.9986733	4.40000	4.6424652
4.45000	.9997006	4.45000	4.6689902
4.50000	.9999438	4.50000	4.6966005
4.55000	.9999912	4.55000	4.7253602
4.60000	.9999989	4.60000	4.7553298
4.65000	.9999999	4.65000	4.7865640
4.70000	1.0000000	4.70000	4.8191097
4.75000	1.0000000	4.75000	4.8530034
4.80000	1.0000000	4.80000	4.8882690
4.85000	1.0000000	4.85000	4.9249157
4.90000	1.0000000	4.90000	4.9629363
4.95000	1.0000000	4.95000	5.0023060
5.00000	1.0000000	5.00000	5.0429822
5.05000	1.0000000	5.05000	5.0849048
5.10000	1.0000000	5.10000	5.1279980
5.15000	1.0000000	5.15000	5.1721725
5.20000	1.0000000	5.20000	5.2173286
5.25000	1.0000000	5.25000	5.2633602
5.30000	1.0000000	5.30000	5.3101581
5.35000	1.0000000	5.35000	5.3576145
5.40000	1.0000000	5.40000	5.4056258
5.45000	1.0000000	5.45000	5.4540960
5.50000	1.0000000	5.50000	5.5029383
5.55000	1.0000000	5.55000	5.5520764
5.60000	1.0000000	5.60000	5.6014454
5.65000	1.0000000	5.65000	5.6509910
5.70000	1.0000000	5.70000	5.7006692
5.75000	1.0000000	5.75000	5.7504450
5.80000	1.0000000	5.80000	5.8002915
5.85000	1.0000000	5.85000	5.8501880
5.90000	1.0000000	5.90000	5.9001194
5.95000	1.0000000	5.95000	5.9500747

NETWORK PARAMETERS
MD = 3.75
N = 20
NO. DET = 4
SIGMA B = .3500
SIGMA D = .2000

TABLE 2

Magnitude bias and detection probability
for Improved Network - restricted distance range

DETECTION PROBABILITY MB	PROB	NETWORK BIAS TRUE MB	EST MB	DETECTION PROBABILITY MB	PROB	NETWORK BIAS TRUE MB	EST MB
1.00000	.0000000	1.00000	3.1158859	3.50000	.8243254	3.50000	3.8738188
1.05000	.0000000	1.05000	3.1289263	3.55000	.9094053	3.55000	3.8958986
1.10000	.0000000	1.10000	3.1419912	3.60000	.9597181	3.60000	3.9187407
1.15000	.0000000	1.15000	3.1550819	3.65000	.9847099	3.65000	3.9424064
1.20000	.0000000	1.20000	3.1681995	3.70000	.9950872	3.70000	3.9669585
1.25000	.0000000	1.25000	3.1813456	3.75000	.9986733	3.75000	3.9924652
1.30000	.0000000	1.30000	3.1945215	3.80000	.9997006	3.80000	4.0189902
1.35000	.0000000	1.35000	3.2077287	3.85000	.9999438	3.85000	4.0466005
1.40000	.0000000	1.40000	3.2209689	3.90000	.9999912	3.90000	4.0753602
1.45000	.0000000	1.45000	3.2342437	3.95000	.9999989	3.95000	4.1053298
1.50000	.0000000	1.50000	3.2475551	4.00000	.9999999	4.00000	4.1365640
1.55000	.0000000	1.55000	3.2609048	4.05000	1.0000000	4.05000	4.1691097
1.60000	.0000000	1.60000	3.2742950	4.10000	1.0000000	4.10000	4.2030034
1.65000	.0000000	1.65000	3.2877276	4.15000	1.0000000	4.15000	4.2382690
1.70000	.0000000	1.70000	3.3012048	4.20000	1.0000000	4.20000	4.2749157
1.75000	.0000000	1.75000	3.3147288	4.25000	1.0000000	4.25000	4.3129363
1.80000	.0000000	1.80000	3.3283017	4.30000	1.0000000	4.30000	4.3523060
1.85000	.0000000	1.85000	3.3419255	4.35000	1.0000000	4.35000	4.3929822
1.90000	.0000000	1.90000	3.3556018	4.40000	1.0000000	4.40000	4.4349048
1.95000	.0000000	1.95000	3.3693317	4.45000	1.0000000	4.45000	4.4779980
2.00000	.0000000	2.00000	3.3831152	4.50000	1.0000000	4.50000	4.5221725
2.05000	.0000000	2.05000	3.3969506	4.55000	1.0000000	4.55000	4.5673286
2.10000	.0000000	2.10000	3.4108333	4.60000	1.0000000	4.60000	4.6133602
2.15000	.0000000	2.15000	3.4247540	4.65000	1.0000000	4.65000	4.6601581
2.20000	.0000000	2.20000	3.4388335	4.70000	1.0000000	4.70000	4.7079145
2.25000	.0000000	2.25000	3.4531538	4.75000	1.0000000	4.75000	4.7566258
2.30000	.0000001	2.30000	3.4675548	4.80000	1.0000000	4.80000	4.8062960
2.35000	.0000001	2.35000	3.4820454	4.85000	1.0000000	4.85000	4.8569383
2.40000	.0000002	2.40000	3.4966347	4.90000	1.0000000	4.90000	4.9087764
2.45000	.0000003	2.45000	3.5113326	4.95000	1.0000000	4.95000	4.9617454
2.50000	.0000006	2.50000	3.5261497	5.00000	1.0000000	5.00000	5.0159910
2.55000	.0000012	2.55000	3.5410972	5.05000	1.0000000	5.05000	5.0716692
2.60000	.0000026	2.60000	3.5561872	5.10000	1.0000000	5.10000	5.1288450
2.65000	.0000059	2.65000	3.5714326	5.15000	1.0000000	5.15000	5.1875915
2.70000	.0000140	2.70000	3.5868474	5.20000	1.0000000	5.20000	5.2480850
2.75000	.0000346	2.75000	3.6024465	5.25000	1.0000000	5.25000	5.3104194
2.80000	.0000879	2.80000	3.6182463	5.30000	1.0000000	5.30000	5.3747747
2.85000	.0002270	2.85000	3.6342642	5.35000	1.0000000	5.35000	5.4412460
2.90000	.0005879	2.90000	3.6505193	5.40000	1.0000000	5.40000	5.5099279
2.95000	.0015074	2.95000	3.6670322	5.45000	1.0000000	5.45000	5.5809167
3.00000	.0037713	3.00000	3.6838254	5.50000	1.0000000	5.50000	5.6543098
3.05000	.0090768	3.05000	3.7009234	5.55000	1.0000000	5.55000	5.7301057
3.10000	.0207290	3.10000	3.7183529	5.60000	1.0000000	5.60000	5.8083032
3.15000	.0443519	3.15000	3.7361430	5.65000	1.0000000	5.65000	5.8890018
3.20000	.0879273	3.20000	3.7543253	5.70000	1.0000000	5.70000	5.9722010
3.25000	.1600898	3.25000	3.7729346	5.75000	1.0000000	5.75000	5.7580005
3.30000	.2660748	3.30000	3.7920083	5.80000	1.0000000	5.80000	5.8000003
3.35000	.4026234	3.35000	3.8115875	5.85000	1.0000000	5.85000	5.8500002
3.40000	.5554633	3.40000	3.8317165	5.90000	1.0000000	5.90000	5.9000001
3.45000	.7028317	3.45000	3.8524431	5.95000	1.0000000	5.95000	5.9500000

greatly improved world-wide network with a comparable threshold of about 3.9. In all cases we assumed 20 stations in each network and required observation by 4 or more stations before the event was considered to have been detected. Some of the results for the restricted network are summarized in Table 3.

TABLE 3

Restricted Distance Model

	Detection Probability	Apparent Magnitude	True Magnitude
WWSSN	90%	4.54	4.20
	50%	4.47	4.04
	10%	4.41	3.86
Improved Network	90%	3.89	3.55
	50%	3.82	3.39
	10%	3.76	3.22

An event which appears to the WWSSN to have a magnitude of 4.5 has a "true" value of 4.1. This same event will appear to the Improved Network to have a magnitude of 4.2. Both estimates are biased; the relative bias is 0.3 unit.

Figures 5 and 6 show the interval probability distribution (see SIPRI, 1968, p. 48) for the two networks. The spread in apparent magnitude between the 10% and 90% is only about 0.1 unit, smaller than observed for real networks. Studies of detection capability for networks composed of LRSM stations, WWSS and stations such as TFO (see, for example, Tech. Rept. 64-163, VELA Project VT/036, 1964, Geotech-Teledyne) show that the apparent range between 10% and 90% detection probability is more like 0.3 or 0.4 magnitude unit. Of course, in the real network studies there is no restriction on epicentral distance; all detected events are included. As predicted by Evernden (1967) and observed by Veith and Clawson (1972), the variability of signal levels is greatly increased when the entire distance range for direct P arrival is considered. Because we do not know a priori what the epicentral distances will be for our hypothetical networks, we must model the effect of removing the distance restriction by increasing the standard deviation of m_d. We found that with σ_d about 0.5

NETWORK PARAMETERS
MD = 4.56
N = 20
NO. DET = 4
SIGMA B = .3500
SIGMA D = .4700

TABLE 4

Magnitude bias and detection probability
for WWSSN -- all distances

DETECTION PROBABILITY MB	PROB	NETWORK BIAS TRUE MB	EST MB	DETECTION PROBABILITY MB	PROB	NETWORK BIAS TRUE MB	EST MB
1.00000	.0000000	1.00000	2.3027036	3.50000	.0054670	3.50000	3.9609520
1.05000	.0000000	1.05000	2.3352909	3.55000	.0099205	3.55000	3.9954215
1.10000	.0000000	1.10000	2.3678887	3.60000	.0176484	3.60000	4.0300004
1.15000	.0000000	1.15000	2.4004975	3.65000	.0301334	3.65000	4.0646943
1.20000	.0000000	1.20000	2.4331176	3.70000	.0500384	3.70000	4.0995104
1.25000	.0000000	1.25000	2.4657495	3.75000	.0800796	3.75000	4.1344560
1.30000	.0000000	1.30000	2.4983935	3.80000	.1231546	3.80000	4.1695388
1.35000	.0000000	1.35000	2.5310501	3.85000	.1815933	3.85000	4.2047671
1.40000	.0000000	1.40000	2.5637197	3.90000	.2563215	3.90000	4.2401495
1.45000	.0000000	1.45000	2.5964029	3.95000	.3460732	3.95000	4.2756952
1.50000	.0000000	1.50000	2.6291000	4.00000	.4469903	4.00000	4.3114142
1.55000	.0000000	1.55000	2.6618116	4.05000	.5529068	4.05000	4.3473165
1.60000	.0000000	1.60000	2.6945381	4.10000	.6563878	4.10000	4.3834130
1.65000	.0000000	1.65000	2.7272801	4.15000	.7502698	4.15000	4.4197151
1.70000	.0000000	1.70000	2.7600379	4.20000	.8291814	4.20000	4.4562348
1.75000	.0000000	1.75000	2.7928121	4.25000	.8905055	4.25000	4.4929845
1.80000	.0000000	1.80000	2.8256030	4.30000	.9344814	4.30000	4.5299771
1.85000	.0000000	1.85000	2.8584111	4.35000	.9635289	4.35000	4.5672262
1.90000	.0000000	1.90000	2.8912365	4.40000	.9811722	4.40000	4.6047457
1.95000	.0000000	1.95000	2.9240795	4.45000	.9910109	4.45000	4.6425497
2.00000	.0000000	2.00000	2.9569399	4.50000	.9960406	4.50000	4.6806529
2.05000	.0000000	2.05000	2.9898174	4.55000	.9983946	4.55000	4.7190639
2.10000	.0000000	2.10000	3.0227114	4.60000	.9994019	4.60000	4.7578157
2.15000	.0000000	2.15000	3.0556204	4.65000	.9997956	4.65000	4.7969053
2.20000	.0000000	2.20000	3.0885425	4.70000	.9999360	4.70000	4.8363532
2.25000	.0000000	2.25000	3.1214745	4.75000	.9999817	4.75000	4.8761738
2.30000	.0000000	2.30000	3.1544853	4.80000	.9999952	4.80000	4.9163808
2.35000	.0000000	2.35000	3.1875923	4.85000	.9999988	4.85000	4.9569874
2.40000	.0000000	2.40000	3.2207246	4.90000	.9999997	4.90000	4.9980057
2.45000	.0000001	2.45000	3.2538839	4.95000	.9999999	4.95000	5.0394464
2.50000	.0000001	2.50000	3.2870722	5.00000	1.0000000	5.00000	5.0813189
2.55000	.0000001	2.55000	3.3202916	5.05000	1.0000000	5.05000	5.1236310
2.60000	.0000002	2.60000	3.3535443	5.10000	1.0000000	5.10000	5.1663883
2.65000	.0000002	2.65000	3.3868324	5.15000	1.0000000	5.15000	5.2095943
2.70000	.0000004	2.70000	3.4201583	5.20000	1.0000000	5.20000	5.2532501
2.75000	.0000006	2.75000	3.4535245	5.25000	1.0000000	5.25000	5.2973543
2.80000	.0000010	2.80000	3.4869334	5.30000	1.0000000	5.30000	5.3419027
2.85000	.0000017	2.85000	3.5203879	5.35000	1.0000000	5.35000	5.3868885
2.90000	.0000029	2.90000	3.5538907	5.40000	1.0000000	5.40000	5.4323019
2.95000	.0000052	2.95000	3.5874448	5.45000	1.0000000	5.45000	5.4781307
3.00000	.0000093	3.00000	3.6210533	5.50000	1.0000000	5.50000	5.5243598
3.05000	.0000171	3.05000	3.6547195	5.55000	1.0000000	5.55000	5.5709720
3.10000	.0000319	3.10000	3.6884469	5.60000	1.0000000	5.60000	5.6179479
3.15000	.0000604	3.15000	3.7222391	5.65000	1.0000000	5.65000	5.6652562
3.20000	.0001155	3.20000	3.7560999	5.70000	1.0000000	5.70000	5.7129042
3.25000	.0002220	3.25000	3.7900335	5.75000	1.0000000	5.75000	5.7609383
3.30000	.0004276	3.30000	3.8240441	5.80000	1.0000000	5.80000	5.8092443
3.35000	.0008211	3.35000	3.8581362	5.85000	1.0000000	5.85000	5.8578976
3.40000	.0015656	3.40000	3.8923148	5.90000	1.0000000	5.90000	5.9061739
3.45000	.0029499	3.45000	3.9265850	5.95000	1.0000000	5.95000	5.9550495

NETWORK PARAMETERS
MD = 3.95
N = 20
NO. DET = 4
SIGMA B = .3500
SIGMA D = .4700

TABLE 5

Magnitude bias and detection probability for Improved Network - all distances

DETECTION PROBABILITY MB	PROB	NETWORK BIAS TRUE MB	EST MB	DETECTION PROBABILITY MB	PROB	NETWORK BIAS TRUE MB	EST MB
1.00000	.0000000	1.00000	2.0910853	3.50000	.6761382	3.50000	3.7806566
1.05000	.0000000	1.05000	2.1238303	3.55000	.7673765	3.55000	3.8170013
1.10000	.0000000	1.10000	2.1565914	3.60000	.8428843	3.60000	3.8535659
1.15000	.0000000	1.15000	2.1893689	3.65000	.9006362	3.65000	3.8903631
1.20000	.0000000	1.20000	2.2221632	3.70000	.9413811	3.70000	3.9274060
1.25000	.0000000	1.25000	2.2549748	3.75000	.9678502	3.75000	3.9647081
1.30000	.0000000	1.30000	2.2878037	3.80000	.9836569	3.80000	4.0022833
1.35000	.0000000	1.35000	2.3206502	3.85000	.9923206	3.85000	4.0401459
1.40000	.0000000	1.40000	2.3535140	3.90000	.9966725	3.90000	4.0783107
1.45000	.0000000	1.45000	2.3863949	3.95000	.9986733	3.95000	4.1167923
1.50000	.0000000	1.50000	2.4192920	4.00000	.9995141	4.00000	4.1556057
1.55000	.0000000	1.55000	2.4522039	4.05000	.9998368	4.05000	4.1947657
1.60000	.0000000	1.60000	2.4851283	4.10000	.9999498	4.10000	4.2342870
1.65000	.0000000	1.65000	2.5180617	4.15000	.9999859	4.15000	4.2741838
1.70000	.0000000	1.70000	2.5511048	4.20000	.9999964	4.20000	4.3144698
1.75000	.0000000	1.75000	2.5842167	4.25000	.9999991	4.25000	4.3551578
1.80000	.0000000	1.80000	2.6173542	4.30000	.9999998	4.30000	4.3962597
1.85000	.0000001	1.85000	2.6505192	4.35000	1.0000000	4.35000	4.4377861
1.90000	.0000001	1.90000	2.6837135	4.40000	1.0000000	4.40000	4.4797460
1.95000	.0000001	1.95000	2.7169394	4.45000	1.0000000	4.45000	4.5221467
2.00000	.0000002	2.00000	2.7501990	4.50000	1.0000000	4.50000	4.5649935
2.05000	.0000003	2.05000	2.7834945	4.55000	1.0000000	4.55000	4.6082895
2.10000	.0000004	2.10000	2.8168282	4.60000	1.0000000	4.60000	4.6520352
2.15000	.0000007	2.15000	2.8502027	4.65000	1.0000000	4.65000	4.6962286
2.20000	.0000011	2.20000	2.8836206	4.70000	1.0000000	4.70000	4.7408652
2.25000	.0000019	2.25000	2.9170845	4.75000	1.0000000	4.75000	4.7859373
2.30000	.0000033	2.30000	2.9505973	4.80000	1.0000000	4.80000	4.8314349
2.35000	.0000058	2.35000	2.9841621	4.85000	1.0000000	4.85000	4.8773450
2.40000	.0000105	2.40000	3.0177818	4.90000	1.0000000	4.90000	4.9236522
2.45000	.0000193	2.45000	3.0514600	4.95000	1.0000000	4.95000	4.9703388
2.50000	.0000362	2.50000	3.0852000	5.00000	1.0000000	5.00000	5.0173849
2.55000	.0000687	2.55000	3.1190056	5.05000	1.0000000	5.05000	5.0647689
2.60000	.0001316	2.60000	3.1528807	5.10000	1.0000000	5.10000	5.1124681
2.65000	.0002531	2.65000	3.1868293	5.15000	1.0000000	5.15000	5.1604586
2.70000	.0004873	2.70000	3.2208558	5.20000	1.0000000	5.20000	5.2087159
2.75000	.0009349	2.75000	3.2549649	5.25000	1.0000000	5.25000	5.2572153
2.80000	.0017790	2.80000	3.2891614	5.30000	1.0000000	5.30000	5.3059338
2.85000	.0033422	2.85000	3.3234504	5.35000	1.0000000	5.35000	5.3548466
2.90000	.0061702	2.90000	3.3578376	5.40000	1.0000000	5.40000	5.4039314
2.95000	.0111434	2.95000	3.3923286	5.45000	1.0000000	5.45000	5.4531670
3.00000	.0196013	3.00000	3.4269298	5.50000	1.0000000	5.50000	5.5025335
3.05000	.0334437	3.05000	3.4616476	5.55000	1.0000000	5.55000	5.5520124
3.10000	.0551409	3.10000	3.4964869	5.60000	1.0000000	5.60000	5.6015872
3.15000	.0875642	3.15000	3.5314613	5.65000	1.0000000	5.65000	5.6512430
3.20000	.1335578	3.20000	3.5665725	5.70000	1.0000000	5.70000	5.7009665
3.25000	.1952405	3.25000	3.6018309	5.75000	1.0000000	5.75000	5.7507461
3.30000	.2731556	3.30000	3.6372452	5.80000	1.0000000	5.80000	5.8005719
3.35000	.3655320	3.35000	3.6728249	5.85000	1.0000000	5.85000	5.8504351
3.40000	.4680021	3.40000	3.7085796	5.90000	1.0000000	5.90000	5.9003287
3.45000	.5740415	3.45000	3.7445199	5.95000	1.0000000	5.95000	5.9502465

60<

the apparent spread in magnitude from a 10% to 90% detection probability is about 0.35 unit, in good agreement with observed results. Table 4 and 5 and figures 7 and 8 show detection capability and magnitude bias for the two hypothetical networks with $\sigma_d = 0.47$. A summary of these results is given in Table 6.

TABLE 6

Unrestricted Distance Model

	Detection Probability	Apparent Magnitude	True Magnitude
WWSSN	90%	4.50	4.25
	50%	4.33	4.03
	10%	4.14	3.77
Improved Network	90%	3.89	3.65
	50%	3.72	3.41
	10%	3.54	3.17

From these calculations we see that an event which appears to the WWSSN to have a magnitude of 4.5 has a "true" value of 4.25. This same event will appear to the Improved Network to have a magnitude of 4.36. Again, both estimates are biased; the relative bias is 0.14 unit.

DISCUSSION

Simulation studies have been used to determine the theoretical detection thresholds for various networks (see SIPRI, 1968, pp. 115 - 125). Maps produced from these studies show contours of detection threshold in terms of "true" magnitude, as defined earlier in this paper. Empirical studies of data obtained from one of these networks would provide detection thresholds in terms of apparent magnitude. Unless magnitude bias is considered, no real network can ever appear to have as low a detection threshold as was predicted by the simulation studies. The computer codes used for these studies can easily be modified to give the apparent magnitude for each event detected; all of the pertinent information is available in memory. We suggest that network studies of this kind should, in the future, provide threshold calculations in terms of both apparent and "true" magnitude, and that the results of empirical network studies should be corrected for magnitude bias.

The computations of magnitude bias for small events presented in the previous section are conservative in that we assumed an accurate measurement of the signal amplitude had been made; additive noise was not considered. In general,

the presence of noise will increase the magnitude bias for threshold events. Results for the two networks show conclusively that magnitude bias must be taken into account in the comparison of performance by networks with significantly different thresholds and in the estimation of the source energy of events near the threshold for the detecting network.

Acknowledgements

We wish to thank Nancy Cunningham for programming assistance and Gerry Clawson for helpful discussions during the course of this study. We particularly wish to thank Dr. C. A. Swanberg who, while a suffering graduate student, laboriously read the amplitude and period of 2596 signals. The work was supported by grant number AFOSR 71-2133 from the Air Force Office of Scientific Research as part of the Advanced Research Projects Agency's project Vela Uniform.

REFERENCES

Evernden, J. F. (1967) Magnitude determinations at regional and near-regional distances in the United States, Bull. Seism. Soc. Am. 57, 591-639.

Freedman, Helen W. (1967) Estimating earthquake magnitude, Bull. Seism. Soc. Am. 57, 747-760.

Gutenberg, B. (1945a) Amplitudes of P, PP, S and magnitude of shallow earthquakes, Bull. Seism. Soc. Am. 35, 57-69.

Gutenberg, B. (1945b) Magnitude determinations for shallow focus earthquakes, Bull. Seism. Soc. Am. 35, 117-130.

Mack, H. (1969) Nature of short-period P-wave signal variations at LASA, J. Geophy. Res. 74, 3161-3170.

SIPRI Report (1968) Seismic Methods for Monitoring Underground Explosions, International Institute for Peace and Conflict Research, Stockholm, 130 pp.

Veith, K. F., and G. E. Clawson (1972) Magnitude from short-period P-wave data, Bull. Seism. Soc. Am. 62, 435-452.

FIGURE CAPTIONS

Figure 1: LASA summation for presumed explosion of 21 April 1966, in East Kazakhstan, U.S.S.R.

Figure 2: Simulation study - histogram of A/T.

Figure 3: Simulation study - histogram of log A/T.

Figure 4: Schematic diagram of stonewall model.

Figure 5: Magnitude bias and detection probability for WWSSN - restricted distance range.

Figure 6: Magnitude bias and detection probability for Improved Network - restricted distance range.

Figure 7: Magnitude bias and detection probability for WWSSN - all distances.

Figure 8: Magnitude bias and detection probability for Improved Network - all distances.

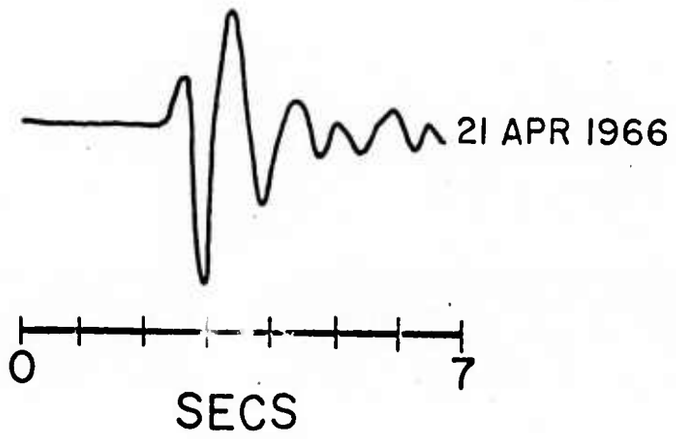

Figure 1

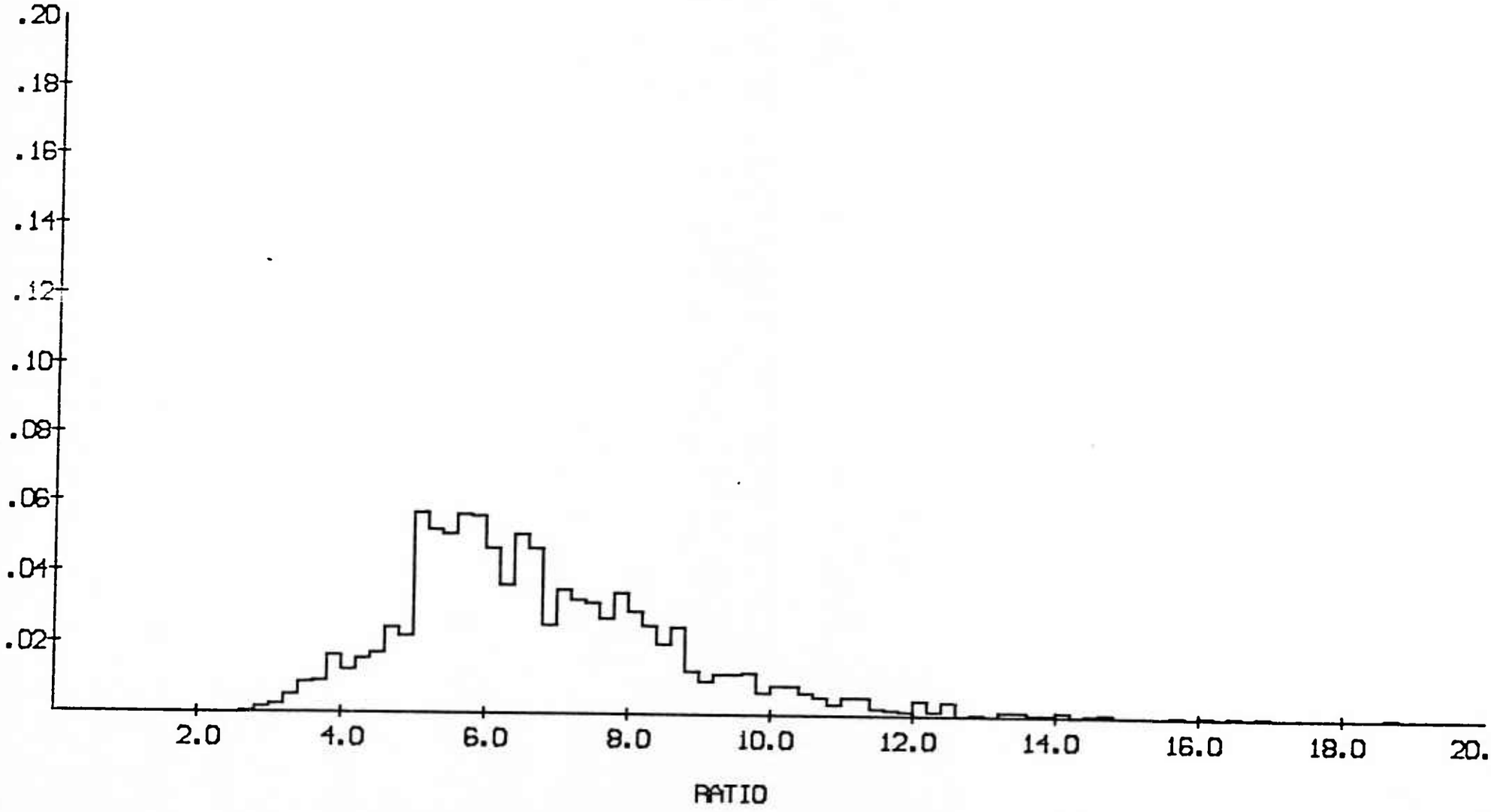

Figure 2

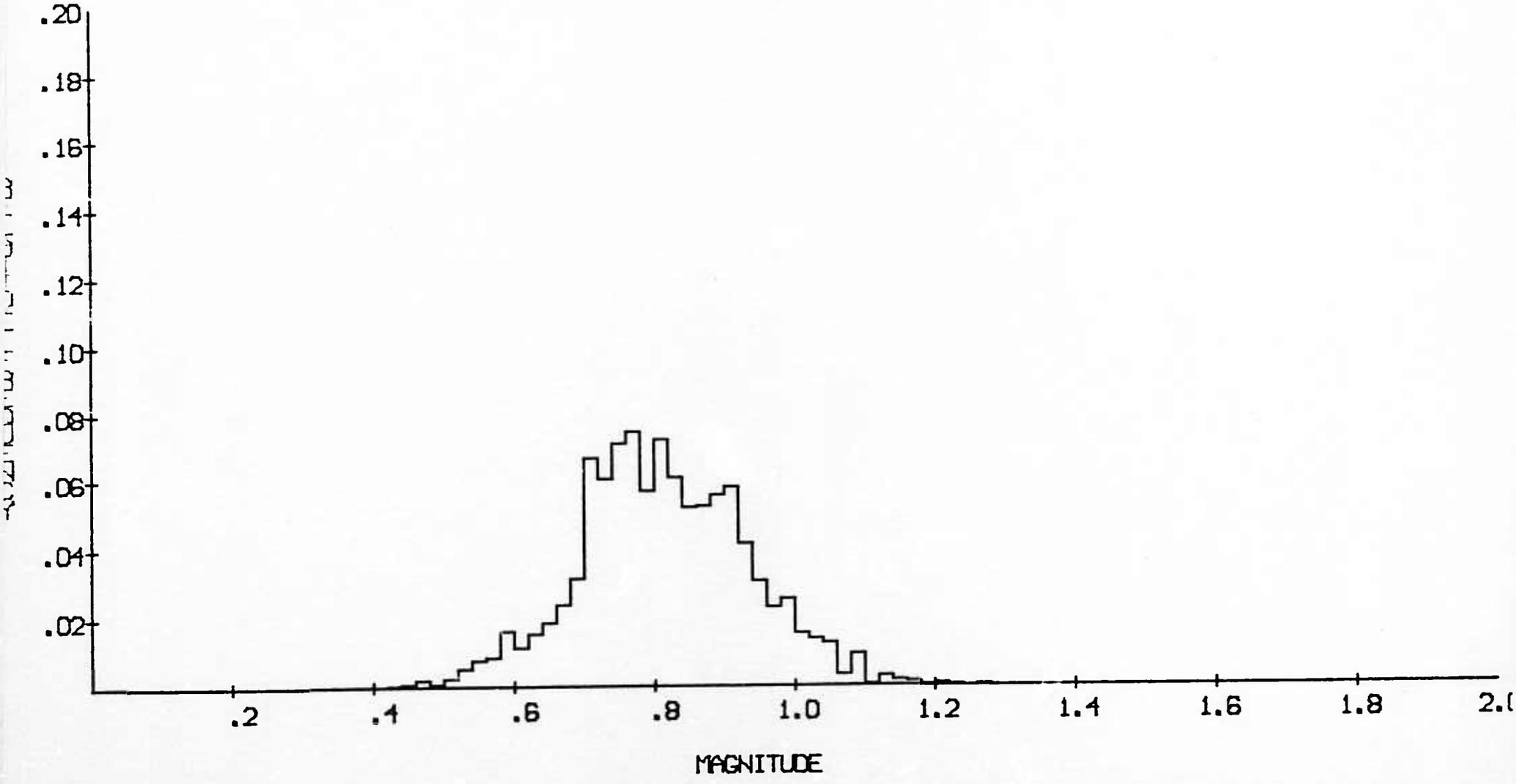

Figure 3

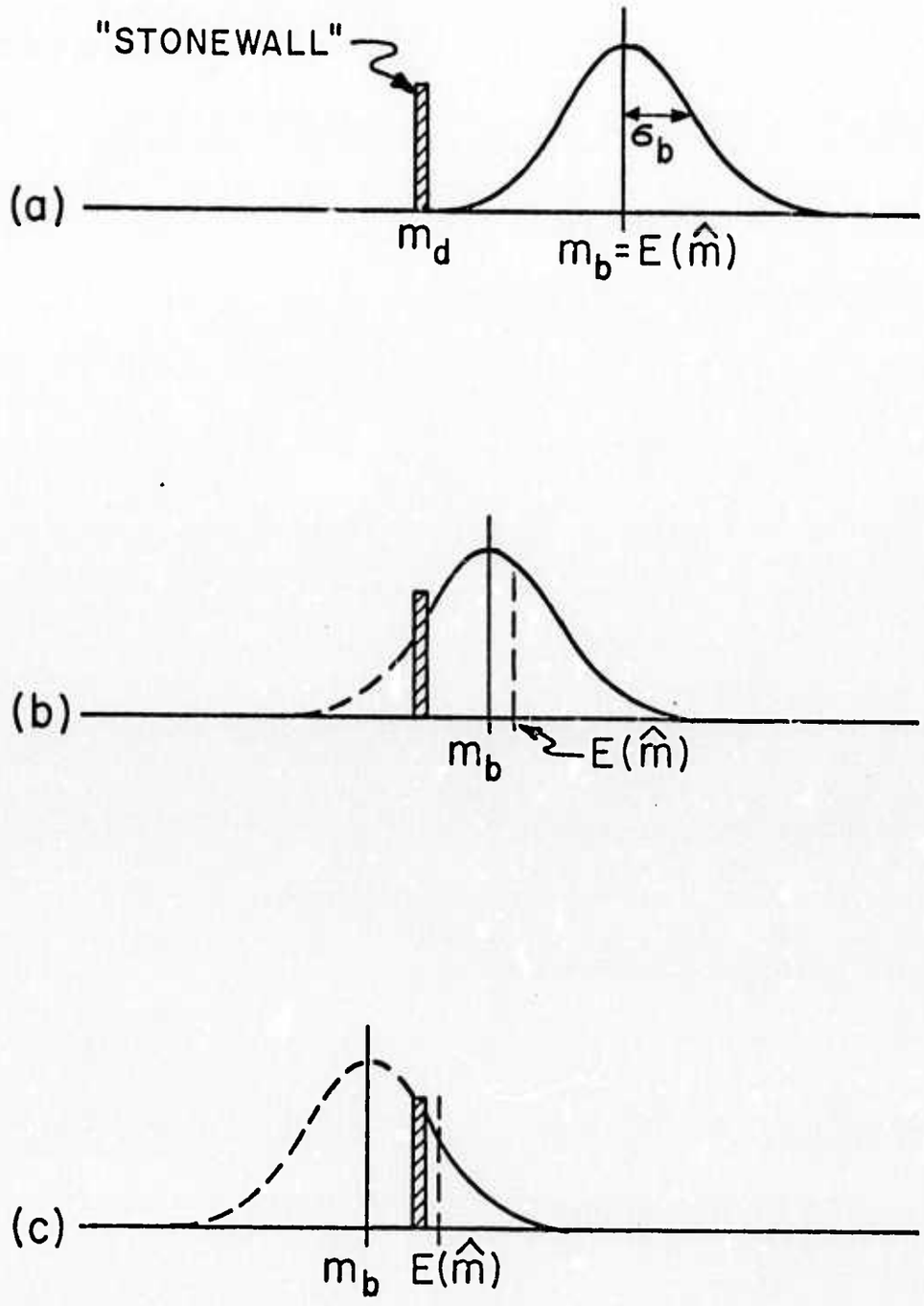

Figure 4

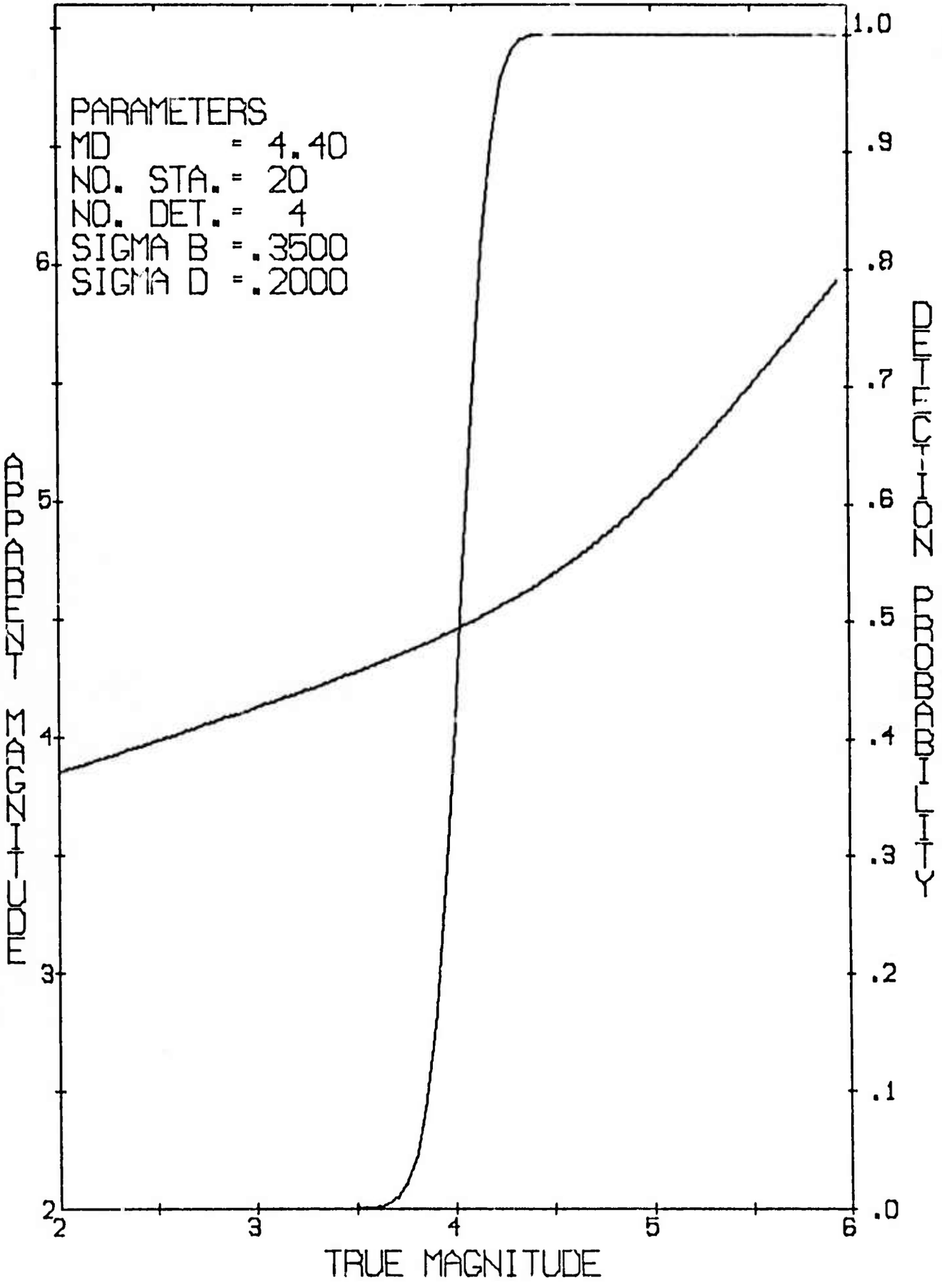
PARAMETERS
MD = 4.40
NO. STA. = 20
NO. DET. = 4
SIGMA B = .3500
SIGMA D = .2000
MEASURED MAGNITUDE
DETECTION PROBABILITY
TRUE MAGNITUDE
2
3
4
5
6
.0
.1
.2
.3
.4
.5
.6
.7
.8
.9
1.0

Figure 5

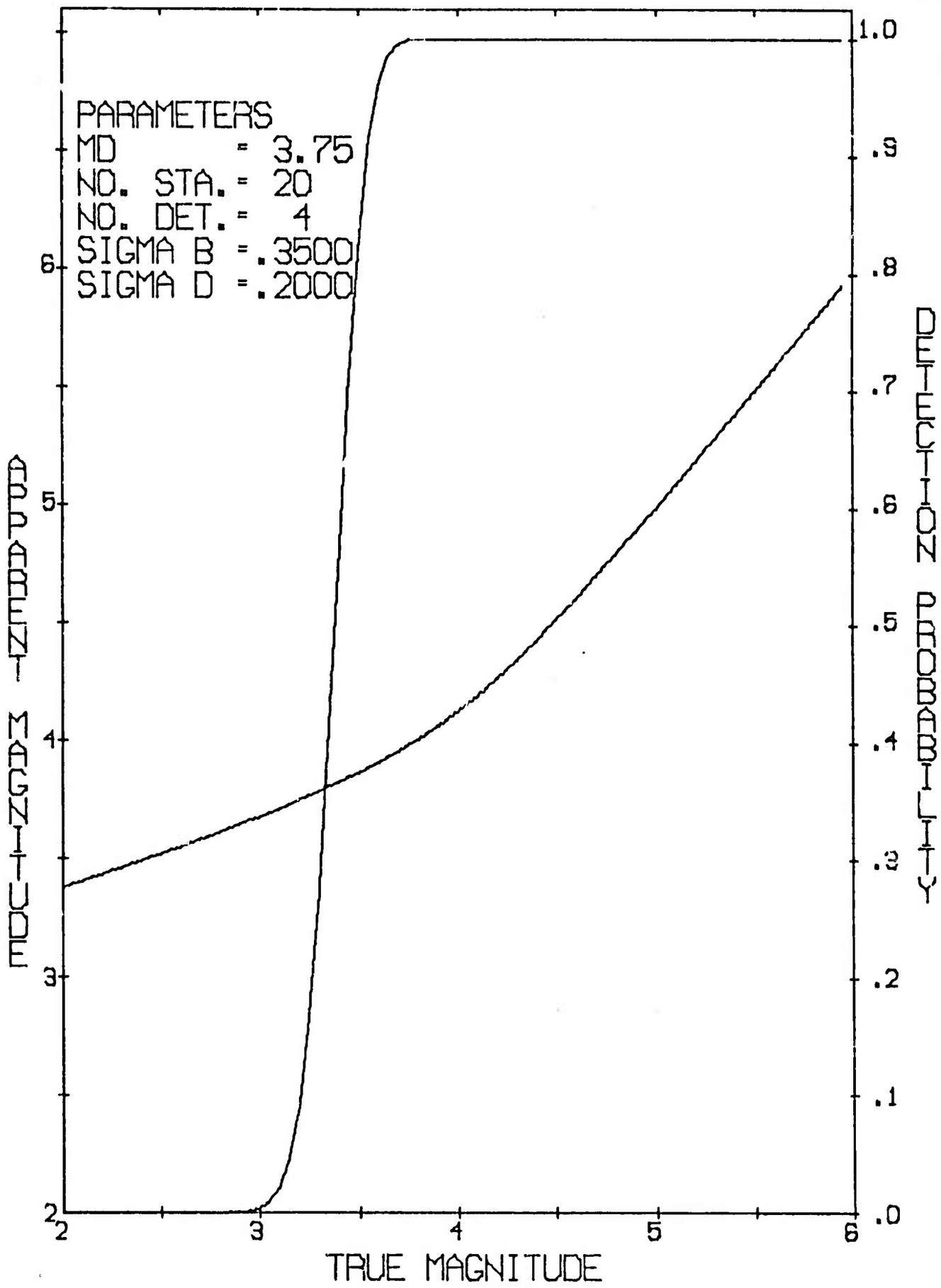
PARAMETERS
MD = 3.75
NO. STA. = 20
NO. DET. = 4
SIGMA B = .3500
SIGMA D = .2000
DETECTION PROBABILITY
1.0
.9
.8
.7
.6
.5
.4
.3
.2
.1
.0
6
5
4
3
2
2
3
4
5
6
TRUE MAGNITUDE

Figure 6

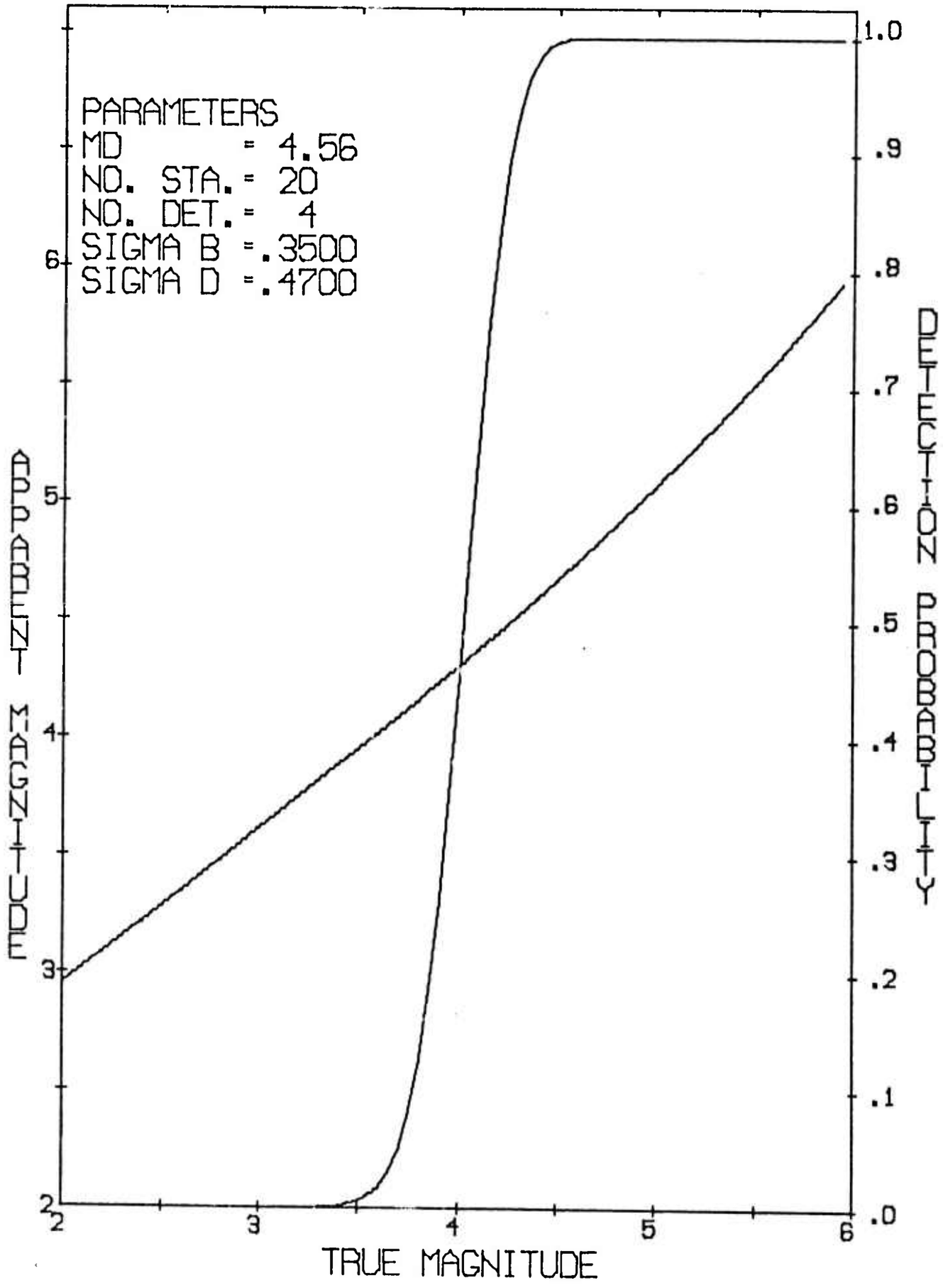
PARAMETERS
MD = 4.56
NO. STA. = 20
NO. DET. = 4
SIGMA B = .3500
SIGMA D = .4700
APPARENT MAGNITUDE
DETECTION PROBABILITY
TRUE MAGNITUDE
2
3
4
5
6
1.0
.9
.8
.7
.6
.5
.4
.3
.2
.1
.0

Figure 7

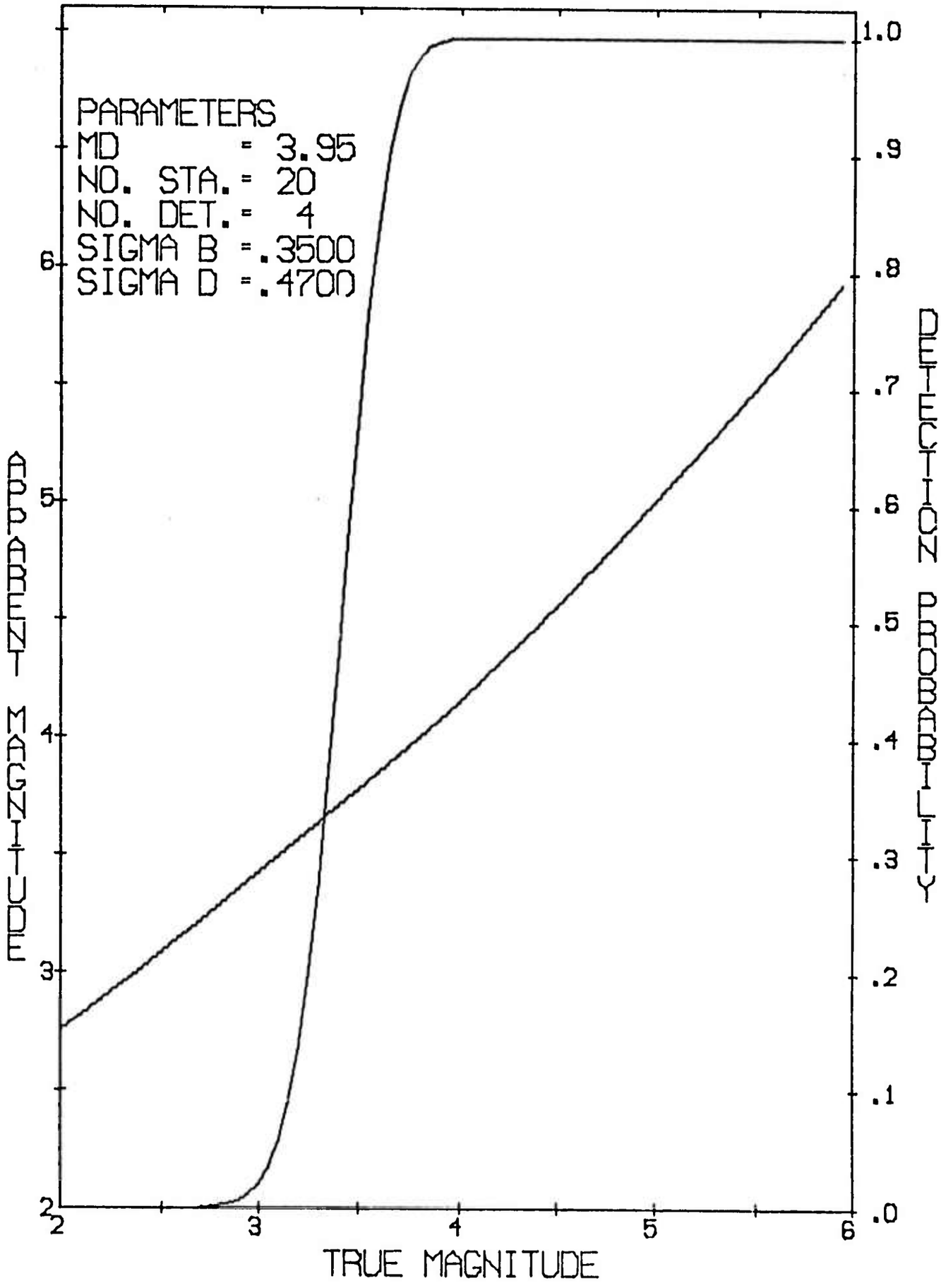
PARAMETERS
MD = 3.95
NO. STA. = 20
NO. DET. = 4
SIGMA B = .3500
SIGMA D = .4700
APPARENT MAGNITUDE
TRUE MAGNITUDE
DETECTION PROBABILITY
2
3
4
5
6
.0
.1
.2
.3
.4
.5
.6
.7
.8
.9
1.0

Figure 8

APPENDIX

Derivation of the net detection probability. We suppose that the observed body wave magnitude, M_b, is a random variable with

$$M_b \sim N(m_b, \sigma_b^2)$$

and that the threshold magnitude, M_d, is also a random variable with

$$M_d \sim N(m_d, \sigma_d^2)$$

with M_b and M_d independent. Then the probability that any given station detects, p, is given by

$$p = Pr(M_b > M_d) = Pr(M_b - M_d > 0).$$

But

$$M_b - M_d \sim N(m_b - m_d, \sigma^2)$$

where

$$\sigma^2 = \sigma_b^2 + \sigma_d^2$$

so that

$$p = Pr\left(\frac{M_b - M_d - (m_b - m_d)}{\sigma} > \frac{m_d - m_b}{\sigma}\right)$$

$$= Pr\left(Z > \frac{m_d - m_b}{\sigma}\right)$$

where Z is the standard normal variable. Thus we obtain the result that the individual station detection probabilities are all equal. It then follows from the definition of the binomial distribution that

$$Pr(\text{Net Detection}) = P_{n,N}$$
$$= \sum_{x=n}^{N} \binom{N}{x} p^x q^{N-x}$$

where

$$q = 1 - p$$
$$\binom{N}{x} = \frac{N!}{(N-x)!\,x!} \quad .$$

But as is well known the binomial cumulative can be evaluated by the incomplete beta function as

$$P_{n,N} = \frac{1}{B(n, N-n+1)} \int_0^p x^{n-1} (1-x)^{N-n} \, dx \quad .$$

Let $x = z/(1+z)$, $0 \le x \le 1$

so that

$$\frac{dx}{dz} = (1+z)^{-2}$$

and

$$P_{n,N} = \frac{\Gamma(N+1)}{\Gamma(n)\Gamma(N-n+1)} \int_0^{\frac{p}{1-p}} z^{n-1} (1+z)^{-(N+1)} \, dz$$

which gives

$$P_{n,N} = \frac{\Gamma\left(\frac{i+j}{2}\right)}{\Gamma\left(\frac{i}{2}\right)\Gamma\left(\frac{j}{2}\right)} \int_0^{\frac{p}{1-p}} z^{\frac{i}{2}-1}(1+z)^{-\left(\frac{i+j}{2}\right)} dz$$

if $i = 2n$

and $j = 2(N-n+1)$.

Now let $z = \frac{i}{j} t, \quad 0 \le z < \infty$

so that $\frac{dz}{dt} = \frac{i}{j}$

and

$$P_{n,N} = \frac{\Gamma\left(\frac{i+j}{2}\right)}{\Gamma\left(\frac{i}{2}\right)\Gamma\left(\frac{j}{2}\right)} \int_0^{\frac{\frac{j}{i}p}{1-p}} \left(\frac{i}{j}t\right)^{\frac{i}{2}} \left(1+\frac{i}{j}t\right)^{-\left(\frac{i+j}{2}\right)} dt$$

which is the cumulative F. Thus

$$P_{n,N} = F_{i,j}\left(\frac{\frac{j}{i}p}{1-p}\right)$$

where

$$i = 2n$$
$$j = 2(N-n+1)$$
$$p = P_r\left(z > \frac{m_d - m_b}{\sigma}\right).$$

We note that the result is valid for any constant station detection probability, p, so that other distributional assumptions on M_b and M_d are possible. Note that if $\sigma_d = 0$ then M_d degenerates to the point m_d and

$$p = P_r\left(z > \frac{m_d - m_b}{\sigma_b}\right)$$

giving the stonewall case. With the other parameters held fixed the effect of increasing σ_d is to rotate p about $m_b = m_d$. Thus for $m_b > m_d$ p is decreased and for $m_b < m_d$ p is increased. If p increases then $\frac{p}{1-p}$ increases even more and if p decreases $\frac{p}{1-p}$ decreases even more. Therefore, with the other parameters fixed the final effect on $P_{n,N}$ is a rotation. For $m_b > m_d$ $F_{i,j}$ is decreased as σ_d is increased and for $m_b < m_d$ $F_{i,j}$ is increased as σ_d is increased.

It is easy to show that

$$p \to 1, \text{ as } m_b \to \infty$$

and

$$p \to 0, \text{ as } m_b \to -\infty$$

If m_d is changed, say

$$\tilde{m}_d = m_d + \Delta$$

and we let

$$\tilde{m}_b = m_b + \Delta$$

then p remains the same (assuming σ to be constant). Thus with the other parameters held fixed an incremental change in m_d produces only a location shift in $P_{n,N}$.

Derivation of the bias in magnitude estimates. We suppose that the station detection probability, p, is constant and that the magnitude estimate, $\hat{m}$, is formed from only those stations which detect. Thus

$$\hat{m} = \sum_{k=1}^{n_d} M_b(k) / n_d$$

where

n_d = the number of stations that detect,

$M_b(k)$ = the magnitude of the $k^{\underline{th}}$ station that detected.

Since only the detected magnitudes are employed any expectations must be formed conditional on a detection occurring and the mean of $\hat{m}$ is $E(\hat{m} \mid \text{Net dection}) = E(\hat{m} \mid n,N)$, say. We have

$$E(\hat{m}|n,N) = \frac{1}{P_{n,N}} \sum_{n_d=n}^{N} \left(\frac{1}{n_d} \sum_{k=1}^{n_d} E\left[M_b(k) \middle| M_b(k) > M_d(k)\right] \right) \binom{N}{n_d} P^{n_d} q^{N-n_d} .$$

With our previous assumptions on M_b and M_d we have that

$$E(M_b(k) \mid M_b(k) > M_d(k)) = E(M_b \mid M_b > M_d) .$$

Then

$$E(\hat{m} \mid n,N) = \sum_{n_d=n}^{N} \left(E\left[M_b \middle| M_b > M_d\right] \binom{N}{n_d} P^{n_d} q^{N-n_d} \right) \frac{1}{P_{n,N}} .$$

$$= E\left[M_b \middle| M_b > M_d\right] .$$

Thus the mean of the magnitude estimator is a function of only the conditional distribution of M_b given $M_b > M_d$. This result also holds for any distributional assumptions on M_b and M_d that give $E(M_b(k) \mid M_b(k) > M_d(k))$ a constant over k and p constant.

Let the conditional density be denoted by $f(x \mid M_b > M_d)$.

Then

$$f(x \mid M_b > M_d) = \frac{d}{dx} Pr(M_b \le x \mid M_b > M_d)$$

$$= \frac{d}{dx} \frac{Pr(M_b \le x \text{ and } M_b > M_d)}{Pr(M_b > M_d)}$$

$$= \frac{1}{P} \frac{d}{dx} Pr(M_b \le x \text{ and } M_b > M_d)$$

We have $Pr(M_b \le x \text{ and } M_b > M_d)$

$$= \int_{-\infty}^{x} \int_{-\infty}^{u} f_{M_b}(u) f_{M_d}(v) \, dv \, du$$

$$= \int_{-\infty}^{x} \Phi\left(\frac{u - m_d}{\sigma_d}\right) f_{M_b}(u) \, du$$

where $$\Phi(y) = \int_{-\infty}^{y} \frac{1}{\sqrt{2\pi}} e^{-\frac{z^2}{2}} \, dz \quad .$$

We then have that

$$\frac{d}{dx} Pr(M_b \le x \text{ and } M_b > M_d)$$

$$= \Phi\left(\frac{x - m_d}{\sigma_d}\right) \frac{1}{\sqrt{2\pi}\,\sigma_b} e^{-\frac{1}{2}\left(\frac{x - m_b}{\sigma_b}\right)^2}$$

so that $$f(x \mid M_b > M_d) = \frac{1}{P} \Phi\left(\frac{x - m_d}{\sigma_d}\right) \frac{1}{\sqrt{2\pi}\,\sigma_b} e^{-\frac{1}{2}\left(\frac{x - m_b}{\sigma_b}\right)^2}, \quad -\infty < x < \infty .$$

The conditional mean is thus

$$E[M_b \mid M_b > M_d]$$

$$= \int_{-\infty}^{\infty} \frac{x}{P} \Phi\left(\frac{x - m_d}{\sigma_d}\right) \frac{1}{\sqrt{2\pi}\,\sigma_b} e^{-\frac{1}{2}\left(\frac{x - m_b}{\sigma_b}\right)^2} dx \quad .$$

80<

Let $$z = \frac{x - m_b}{\sigma_b}, \quad -\infty < x < \infty$$

so that $$\frac{dz}{dx} = \frac{1}{\sigma_b}$$

to obtain

$$E[M_b \mid M_b > M_d]$$

$$= \frac{1}{p\sqrt{2\pi}} \int_{-\infty}^{\infty} (\sigma_b z + m_b) \Phi\left(\frac{\sigma_b z + m_b - m_d}{\sigma_d}\right) e^{-\frac{z^2}{2}} dz$$

$$= \frac{1}{p\sqrt{2\pi}} \left[m_b \int_{-\infty}^{\infty} \Phi\left(\frac{\sigma_b z + m_b - m_d}{\sigma_d}\right) e^{-\frac{z^2}{2}} dz \right.$$

$$\left. + \sigma_b \int_{-\infty}^{\infty} z \Phi\left(\frac{\sigma_b z + m_b - m_d}{\sigma_d}\right) e^{-\frac{z^2}{2}} dz \right].$$

But the first integral is just $p\sqrt{2\pi}$ so that

$$E[M_b \mid M_b > M_d] = m_b + \frac{\sigma_b}{p\sqrt{2\pi}} \int_{-\infty}^{\infty} z \Phi\left(\frac{\sigma_b z + m_b - m_d}{\sigma_d}\right) e^{-\frac{z^2}{2}} dz.$$

Now let $$u = \Phi\left(\frac{\sigma_b z + m_b - m_d}{\sigma_d}\right)$$

and

$$dv = z e^{-\frac{z^2}{2}} dz$$

to obtain

$$\int_{-\infty}^{\infty} z \Phi\left(\frac{\sigma_b z + m_b - m_d}{\sigma_d}\right) e^{-\frac{z^2}{2}} dz$$

$$= \int_{-\infty}^{\infty} u \, dv$$

$$= uv\Big|_{-\infty}^{\infty} - \int_{-\infty}^{\infty} v\,du$$

$$= -\Phi\left(\frac{\sigma_b z + m_b - m_d}{\sigma_d}\right) e^{-\frac{z^2}{2}}\Big|_{-\infty}^{\infty} + \int_{-\infty}^{\infty} e^{-\frac{z^2}{2}} \left(\frac{\sigma_b}{\sigma_d}\right) \frac{1}{\sqrt{2\pi}} e^{-\frac{1}{2}\left(\frac{\sigma_b z + m_b - m_d}{\sigma_d}\right)^2} dz$$

$$= \frac{\sigma_b}{\sigma} e^{-\frac{1}{2}\left(\frac{m_d - m_b}{\sigma}\right)^2} \int_{-\infty}^{\infty} \frac{1}{\sqrt{2\pi}\,\frac{\sigma_d}{\sigma}} e^{-\left\{\frac{1}{2(\sigma_d/\sigma)^2}\left[z - \frac{\sigma_b}{\sigma^2}(m_d - m_b)\right]^2\right\}} dz$$

upon completing the square in the exponent.

Thus $$E[M_b \mid M_b > M_d] = m_b + \frac{\sigma_b^2}{p\sigma\sqrt{2\pi}} e^{-\frac{1}{2}\left(\frac{m_d - m_b}{\sigma}\right)^2}$$

where $$\sigma^2 = \sigma_b^2 + \sigma_d^2$$

and

$$E(\hat{m} \mid n, N) = m_b + \frac{\sigma_b^2}{p\sigma\sqrt{2\pi}} e^{-\frac{1}{2}\left(\frac{m_d - m_b}{\sigma}\right)^2} .$$

If $\sigma_d = 0$ then M_d degenerates to the point m_d and

$$E(\hat{m} \mid n, N) = m_b + \frac{\sigma_b}{p\sqrt{2\pi}} e^{-\frac{1}{2}\left(\frac{m_d - m_b}{\sigma}\right)^2}$$

giving again the <u>stonewall</u> case.

Recall that as $m_b \to \infty$, $p \to 1$. In this case it is easy to show that

$$E(\hat{m} \mid n, N) \longrightarrow m_b, \text{ as } m_b \to \infty$$

In the case that $m_b \to -\infty$, $p \to 0$ and we employ L'Hopital's rule to show that

$$E(\hat{m} \mid n, N) \longrightarrow \frac{\sigma_d^2}{\sigma^2} m_b + \frac{\sigma_b^2}{\sigma^2} m_d, \text{ as } m_b \to -\infty .$$

Thus if $\sigma_d = 0$, then

$$E(\hat{m} \mid n,N) \to m_d \text{ , as } m_b \to -\infty$$

which is intuitively clear. If $\sigma_d \neq 0$, then

$$\frac{E(\hat{m} \mid n,N)}{m_b} \longrightarrow \frac{\sigma_d^2}{\sigma^2} \text{ , as } m_b \to -\infty$$

and $E(\hat{m} \mid n,N)$ is asympototic to m_b. In this case the effect is a reduction in bias relative to the case when $\sigma_d = 0$ for "smaller" m_b.

Other distributional assumptions. We also studied the case of a uniform distribution on M_d and a normal on M_b. That is we supposed

$$M_b \sim N(m_b, \sigma_b^2)$$

and

$$M_d \sim U(m_d, \text{Halfwidth } W_d)$$

and M_b and M_d independent. After straight forward but tedious computations one obtains

$$p = 1 - \left(\frac{m_d + W_d - m_b}{2W_d}\right)\Phi\left(\frac{m_d + W_d - m_b}{\sigma_b}\right) + \left(\frac{m_d - W_d - m_b}{2W_d}\right)\Phi\left(\frac{m_d - W_d - m_b}{\sigma_b}\right) + \frac{\sigma_b}{2W_d\sqrt{2\pi}}\left[e^{-\frac{1}{2}\left(\frac{m_d - W_d - m_b}{\sigma_b}\right)^2} - e^{-\frac{1}{2}\left(\frac{m_d + W_d - m_b}{\sigma_b}\right)^2}\right]$$

and

$$E(M_b \mid M_b > M_d) = m_b + \frac{\sigma_b^2}{2W_d p}\left\{\Phi\left(\frac{m_d + W_d - m_b}{\sigma_b}\right) - \Phi\left(\frac{m_d - W_d - m_b}{\sigma_b}\right)\right\}.$$

Also one has

$$\rho \to 1, \text{ as } m_b \to \infty$$

and

$$\rho \to 0, \text{ as } m_b \to -\infty.$$

It is then easy to show that

$$E(M_b \mid M_b > M_d) \longrightarrow m_b, \text{ as } m_b \to \infty.$$

The case in which $m_b \longrightarrow -\infty$ is not as straight forward. However, in this case $m_d - w_d$ is a lower bound on any magnitude that is observed with a nonzero probability. Thus in this case

$$E(M_b \mid M_b > M_d) \geq m_d - w_d$$

for all m_b. Relative to the normal distribution case the bias should be greater for smaller values of m_b. Test cases verify this. In fact for comparable values of σ_b, m_d and σ_d and w_d the detection probability curves were essentially equal. In every case at values of $m_b < m_d$ the bias in the uniform case was greater than that in the normal case.

TECHNICAL REPORT

to the

AIR FORCE OFFICE OF SCIENTIFIC RESEARCH

from

Tom Goforth

Dallas Geophysical Laboratory
Southern Methodist University
Dallas, Texas 75222

ARPA Order Number: 1827-1
Program Code: 2F10
Name of Contractor: Southern Methodist University
Effective Date of Grant: July 1, 1971
Grant Expiration Date: June 30, 1973
Amount of Grant Dollars: $179,739
Grant Number: 71-2133B
Principal Investigator and Phone Number: Eugene Herrin
214 692-2760
Program Manager and Phone Number: Truman F. Cook, Director of Research Administration
214 692-2031
Title of Work: Identification of Earthquakes and Underground Explosions
University Account Number: 80-46

Sponsored by
Advanced Research Projects Agency
ARPA Order No. 1827-1

A MODEL STUDY OF THE EFFECT ON THE RAYLEIGH SPE[illegible] OF LATERAL HETEROGENEITY IN EARTHQUAKE SOURCE REGIONS

by

Tom T. Goforth

Dallas Geophysical Laboratory
Southern Methodist University
Dallas, Texas

A MODEL STUDY OF

THE EFFECT ON THE RAYLEIGH SPECTRUM OF LATERAL

HETEROGENEITY IN EARTHQUAKE SOURCE REGIONS

Page

Abstract 1

Introduction 4

Construction of the Model 10

Rayleigh Spectra Originating from Foci
in Laterally Homogeneous Layered Media 24

Spectra of Rayleigh Waves from Sources
in the Laterally Heterogeneous Zone 28

Discussion 33

Acknowledgements 36

References 37

LIST OF ILLUSTRATIONS

Figure		Page
1.	Rayleigh wave spectrum recorded at Grand Saline, Texas, from an earthquake in the Tonga Islands	5
2.	Rayleigh spectra from two earthquakes with source depths of 65 and 203 kilometers near New Britain Island illustrating a shift of spectral peak to longer periods with increasing source depth	6
3.	Rayleigh spectra from two earthquakes with source dpeths of 74 and 275 kilometers in the Tonga Islands illustrating the absence of a shift of spectral peak to longer periods with increasing source depth	7
4.	Rayleigh spectra from two earthquakes with source depths of 67 and 602 kilometers in the Mariana Islands illustrating a slight shift of spectral peak with a great increase in source dpeth	9
5.	Model shear wave velocity as a function of depth	16
6.	Diagram showing the dimensions of the model and the widths and velocities of each layer . . .	18
7.	Schematic cross-sectional view of the model . . .	19
8.	Diagram of the mounting of the Clevite PZT-4 piezoelectric crystal used as the receiver . . .	
9.	Block diagram of the modeling electronics . . .	
10.	Comparison of the model source spectrum and the Rayleigh spectrum of a Grand Saline recording	

Page

of an earthquake in the Tonga Islands (Δ = 91.9°; h = 95 kilometers; m_b = 5.3) . . . . . .

11. Comparison of a model seismogram resulting from the application of a vertical surface force on a vinyl-aluminum half-space which has the velocity properties of the model lithosphere and Lamb's theoretical result . . . . . .

12. Flexural waves resulting when the transducer is applied perpendicular to the medial plane of a sheet of 2024-T3 aluminum . . . . . .

13. Comparison of a model seismogram resulting from a source at depth in a homogeneous half-space, represented by a 2024-T3 aluminum plate, with Lapwood's (1947) theoretically-predicted arrival times . . . . . .

14. Model seismogram resulting from a vertical surface source over a layered half-space illustrating the dispersed Rayleigh wave. The scaled propagation distance is 2667 kilometers (24°). The time window selected fro spectral analysis is indicated by the brackets . . . . . .

15. Spectrum of the Rayleigh wave whown in Figure 14 . . .

16. Comparison of model and theoretical Rayleigh spectra for a horizontal force at a scaled depth of 50 kilometers in a layered half-space. The scaled propagation idstance is 24° . . . . . .

17. Comparison of model and theoretical Rayleigh spectra for a vertical force at a scaled depth of 50 kilometers in a layered half-space. The scaled propagation distance is 24°. . . . . .

18. Comparison of model and theoretical Rayleigh spectra for a horizontal force at a scaled depth of 250 kilometers in a layered half-space. The scaled propagation distance is 24°. . . . . .

19. Model source locations in relations to the geometry of the dipping lithospherere . . . . . .

20. Comparison of model Rayleigh spectra for a vertical surface source over the layered half-space and for a vertical surface source over the dipping lithosphere . . . . . .

21. Comparison of model Rayleigh spectra for a vertical source at a scaled depth of 50 kilometers in the layered half-space and for a similar source depth above the dipping lithospherere . . . .

22. Model Rayleigh spectrum from a horizontal force at a scaled depth of 250 kilometers in the dipping lithosphere. Also shown are the theoretical spectrum and the model spectrum for the same source at a depth of 250 kilometers in the layered half-space . . . . . .

23. Rayleigh spectrum from a source aligned along the dip of the lithosphere at a scaled depth of 250 kilometers. Also shown is the Rayleigh spectrum from a horizontal source at a scaled depth of 250 kilometers in the layered half-space . . . . . .

24. Comparison of Rayleigh spectra from sources at scaled depths of 50 to 250 kilometers in a layered half-space . . . . . .

LIST OF TABLES

Table		Page
1.	Commonly available modeling materials and their elastic properties	11
2.	Amplitude attenuation as a function of scaled travel distance and period	26

ABSTRACT

Theory has been previously developed to determine the spectrum of Rayleigh waves which have been excited and propagated through laterally homogeneous layered media. The spectral shape is a complicated function of the source and medium properties, but in general there is a shift of spectral energy in a relative sense toward the longer periods as the source depth is increased.

Studies of Rayleigh wave spectra obtained from a high-gain, long period seismograph at Grand Saline, Texas, show that for earthquakes occurring in some Pacific island arc regions, such as the New Hebrides, New Britian and the Solomons, the relative spectral shift to longer periods with increasing source depth is indeed observed. However, for earthquakes originating in certain other island arc regions, such as Tonga-Kermedec, The Phillipines, and the Marianas, no corresponding spectral shift was observed. In the first group of island arcs, the lithospheric plate dips more or less toward the recording site at Grand Saline; in the second group, the dip is away from Grand Saline. It is suggested that lateral heterogeneity in the earthquake source regions is at least partially responsible for the spectral differences and that in particular the downward bent lithosphere acts as a waveguide at some azimuths for some Rayleigh wavelengths.

To test this hypothesis, a two-dimensional scale model of an assumed island arc source region was designed and constructed. The model was scaled such that Rayleigh energy was in the frequency range 20 to 200 kilohertz. The signals were converted to digital form for spectral analysis. Sources were first located at scaled depths of 0, 50, and 250 kilometers in the laterally homogeneous portion of the model. Spectra from these events agree quite well with theory and give confidence that results obtained in the laterally heterogeneous portion of the model, where theory is not directly applicable, are valid. Sources were then located at similar depths in the dipping portion of the model lithosphere. Comparison of these spectra with those from sources at the same depth in the laterally homogeneous portion indicates a significant enhancement of energy at periods less than 50 seconds for the sources in the dipping lithosphere. At a period of 30 seconds there is about 16 dB more amplitude for a source in the downward bent portion of the lithosphere as compared to the same source at the same depth in the laterally homogeneous portion of the model. There is 7 dB more amplitude at 40 seconds and 5 dB more at 50 seconds. There is no difference at periods of 60 seconds and greater. It is suggested

that wave lengths as large as twice the width of the lithosphere are utilizing it as a wavequide to the surface.

INTRODUCTION

The relations for the far-field surface wave displacements for sources located in specified laterally homogeneous Earth models were presented by Harkrider (1964) and Ben-Menahem and Harkrider (1964), and have been expanded upon in the work of Harkrider and Anderson (1966) and Harkrider (1970). If the source mechanism and the elastic parameters of the model layers are specified, the theory yields smoothly-varying Rayleigh spectra which are quite sensitive to depth of focus.

There are data available, however, which suggest that Rayleigh wave spectra are considerably more complicated than that predicted by theory. During the spring and summer of 1970, Southern Methodist University, in cooperation with Teledyne-Geotech of Garland, Texas, operated and recorded digitally a long-period vertical seismograph in a salt mine near Grand Saline, Texas. The combination of a broad response peaking at 45 seconds and the isolation from atmospherically generated noise achieved by the subterranean location allowed the recording of Rayleigh waves of superior quality. These seismograms offered a previously unavailable

view of the dispersed wave train over the period range 10 to 100 seconds. A point transform technique (Filon, 1928) was used to calculate the Fourier spectra of the dispersed Rayleigh wave trains originating from sources with a wide range of magnitudes, focal depths, epicentral distances, and azimuths. Many of these spectra, such as the typical one shown in Figure 1, are rather complicated with many rapid changes in slope--quite different from the smoothly varying spectra predicted by theory. None of the Grand Saline spectra is corrected for instrument response.

A study of these spectra also indicates a surprising lack of attenuation for periods in the range 20 to 50 seconds with increasing depth of focus in some island arcs.

Figure 2 shows the spectra from two earthquakes with different source depths near New Britain Island. The spectra are normalized at a period of 40 seconds. An increase in the focal depth of from 65 kilometers to 203 kilometers results in a shift of the spectral peak to longer periods. This type result is also found for earthquakes in the New Hebrides and Solomon Islands, and is consistent with intuitive expectations of Rayleigh spectral change with increasing source depth.

A much different pattern is seen in Figure 3, which shows Rayleigh spectra from two earthquakes of different source depth

in the Tonga Islands. These spectra are also normalized at a period of 40 seconds. In this case, an increase in source depth from 74 kilometers to 275 kilometers produces no significant spectral shift. Figure 4 shows the spectra of Rayleigh waves from two earthquakes in the Mariana Islands, one with a focal depth of 67 kilometers and the other with a focal depth of 602 kilometers. The spectra are normalized at a period of 40 seconds. A surprisingly small spectral shift to longer periods is noted for the deeper focus event. The Grand Saline data show a similar lack of shift of Rayleigh spectra with increasing focal depth in the Kermedec and Phillipine Island arcs. No focal mechanism studies have been made for the earthquakes recorded at Grand Saline, and thus the effect that differences in source radiation function have in establishing this pattern is not known. However, it seems possible that factors not included in layered media theory are exerting an influence in some source regions. A likely contributing factor is lateral heterogeneity along the propagation path resulting in (a) horizontal multi-pathing and interference, and (b) refraction, reflection, and scattering effects in the vertical plane containing the source and receiver. In this second category is the effect of the geometry of the source

area with which this paper is concerned.

Earthquakes are now known to originate in anomalous areas of the Earth which are characterized by lateral heterogeneity. In particular, island arcs are the source of a large majority of all earthquakes and the source of essentially all deep earthquakes. Recent evidence from many fields indicates that island arcs are areas in which a portion of the upper mantle is being thrust under the adjacent area, forming a relatively cool, high-strength zone in the midst of hotter, weaker material. Earthquakes originate along this downward-bent wedge of lithosphere, suggesting that a more realistic model for surface wave spectral studies is that of a source at some depth below an elbow in a curved waveguide.

It is interesting to note that the Marianas, Tonga, Kermedec, and Phillipine Islands, where earthquakes recorded at Grand Saline show no large shift of Rayleigh spectral peak to longer periods with increasing depth of focus, are subduction zones in which the lithosphere plunges away from the recording station at Grand Saline. On the other hand, the New Britain, New Hebrides, and Solomon Islands, where earthquakes do show a spectral shift, are zones in which the lithosphere plunges toward Grand Saline. This suggests that the geometry of the dipping lithosphere may be

enhancing the Rayleigh periods of 20 to 50 seconds at those azimuths opposite to the direction of dip.

An Earth model in which a downgoing slab of lithosphere is considered greatly complicates the theoretical problem. Numerical solutions to the laterally heterogeneous problem are possible in principle, but would be complicated and time consuming in practice. As an alternative approach, a two-dimensional analog model of an assumed island arc structure with a downgoing wedge was designed and constructed, and the effect of this source structure on the Rayleigh spectrum was evaluated using the scale model.

Several studies have been made previously of the propagation of Rayleigh waves in two-dimensional models. These have been primarily not scale models of Earth situations, but rather observations of the behavior of Rayleigh waves as they propagate around corners, across non-horizontal boundaries, and through channels of changing width. For example, de Bremaecker (1950) studied the energy conversions occurring when a Rayleigh wave is incident upon a corner whose angle is between 0 and 180 degrees. Knopoff and Gangi (1961), in a similar experiment, observed that the Rayleigh wave undergoes a change in wave form as it negotiates the corner. Kuo

and Thompson (1963) studied experimentally the effect of a gently-sloping interface on the propagation of Rayleigh waves. Gangi (1967) determined experimentally the P wave to Rayleigh wave conversion coefficients at a stress-free wedge. Ottaviani (1971) showed that P waves incident upon a corner generate secondary Rayleigh waves which then propagate in either direction from the corner. All of these investigators used equipment and procedures based on a work by Oliver, Press, and Ewing (1954) who demonstrated mathematically and verified empirically that wave propagation in and on the edge of thin sheets can be related to plane wave propagation in three demensions. The characteristic relation between period and phase velocity for Rayleigh waves on the edge of a plate is the same as for the free surface of an infinite solid. However, the plate dilatational velocity is $Vp = \left[\frac{4\mu(\lambda+\mu)}{\rho(\lambda+2\mu)}\right]^{1/2}$ rather than the infinite solid dilatational velocity, $\alpha = \left[\frac{\lambda+2\mu}{\rho}\right]^{1/2}$, where λ and μ are the Lame elastic constants and ρ is the density. By simply replacing α = Vp, many of the problems of propagation of plane waves in a stratified Earth can be related to two-dimensional models.

CONSTRUCTION OF THE MODEL

In trying to build a scale model of a portion of the Earth it is quickly apparent that the classical technique of two-dimensional model construction, i.e., butt-joining pieces of different materials to fashion layers of different elastic properties, is not satisfactory. There is not a wide enough assortment of available modeling materials to build even the grossest approximation of a crustal and upper mantle structure. Table 1 shows most of the commonly available modeling materials and their elastic velocities. While it is easy enough to find three or four materials with significantly different seismic velocities, it is quite another matter to obtain three or four materials whose velocities differ by a desired specific ratio, which is the necessary criterion for building a scale model.

A solution to this problem was suggested by Angona (1960) and Riznichenko, et al. (1961). If sheets of two materials are joined broadside to form a composite plate, the seismic velocities of wave lengths long in comparison to the total thickness will be intermediate between the velocities of the component plates and will be proportional to the relative thicknesses of the components. The exact empirical relation

TABLE 1

Material	Plate Dilatational Velocity (km/sec)	Shear Velocity (km/sec)	Density (gm/cc)
2024-T3 Aluminum Alloy	5.62	3.24	2.77
Plexiglass	2.36	1.37	1.22
Vinyl	1.96	1.18	1.47
Formica	2.58	1.54	1.30
Copper	3.96	2.29	9.03
Steel	5.44	3.25	7.78
Brass	3.81	2.13	8.34
Zinc	3.99	2.35	7.07

is

$$(1)\quad \bar{v}^2 = \frac{\rho_1 c_1 v_1^2 + \rho_2 c_2 v_2^2}{c_1 \rho_1 + c_2 \rho_2}$$

where $\bar{v}$ is the composite velocity

c_i is the thickness proportion of component i

v_i is the velocity of component i

ρ_i is the density of component i

By selecting a high velocity material such as aluminum, and low velocity material such as vinyl, a wide range of velocities can be obtained by varying the relative thicknesses.

The choice of the particular structure of the crust and upper mantle to be modeled was guided by a desire to have a suitably Earth-like situation incorporating first-order features while avoiding unnecessarily detailed layering. Thus, only four Earth units were modeled--a crust, a high-velocity lithosphere with a dipping wedge, a low-velocity intermediate layer, and a high-velocity half-space. The Earth shear wave velocity distribution, shown in Figure 5, which is a simplification of the oceanic shear wave model of Toksoz and Anderson (1966), was adopted for modeling.

Aluminum has the highest elastic velocities of any easily available modeling material. The basic scaling problem in

constructing the model was to utilize the aluminum as the high-velocity half-space, together with varying thicknesses of vinyl to form the lower velocity layers. Since the shear wave velocity of aluminum is 3.24 km/sec and the desired half-space velocity is 5.4 km/sec, a velocity scale factor of 5/3 was suggested. That is

$$\nu_{\text{Earth}} = 5/3\ \nu_{\text{Model}}$$

The frequency range of interest, (0.01 to 0.1 Hz), can be scaled to the effective frequency range of the piezoelectric transducers (20 to 200 kHz). This implies a time (t) scale factor such that

$$t_{\text{Earth}} = 2 \times 10^6\ t_{\text{Model}}$$

By fixing the time and velocity scale factors, the length relation is constrained to be

$$l_{\text{Earth}} = \nu_{\text{Earth}} \cdot t_{\text{Earth}} = (10/3 \times 10^6)\ l_{\text{Model}}$$

The relative thicknesses of the vinyl and the aluminum in the composite sheets forming the upper zones were determined by equation 1. A diagram showing the dimensions of the model and the widths and velocities of each layer are shown in Figure 6. Shown in Figure 7 is a schematic cross-sectional view of the composite plate model. The four different velocity layers were made from different combinations of two thicknesses

of vinyl, 0.006 inches and 0.016 inches. Each layer of vinyl was attached with Duro E·Pox·E resin, number 14.

The maximum thickness of the composite plate was 0.104 inches, or equivalently, 0.264 centimeters. The shortest wave length of interest was 2.39 centimeters. It is important that the thickness of a two-dimensional model be small compared to the shortest wave lengths of interest. Otherwise, the compressional wave will be dispersive, which of course is not analogous to compressional wave propagation in the Earth.

The Source

A piezoelectric crystal was used as the source of the elastic waves. This type of crystal changes shape when an electric field is applied, and conversely, develops an electric field when pressure is applied. Rochelle salt, ammonium dehydrogen phosphate, lithum sulphate, barium titanate crystals, and lead zirconate-lead titanate (PZT) ceramics are in common use as electromechanical transducers.

Various types of PZT ceramics are available, including radial expanders, length expanders, shear actors, and bimorphs (benders). Each type was investigated for the purpose of determining which was most suitable for the purposes of the study. The chief criteria involved in the selection and implementation

of the source were that it must be a type which could efficiently generate surface waves when located at depth and was attachable to the plate in some fashion so as to excite symmetrical modes, i.e., to induce energy along the medial plane of the plate and not transverse to it. Length expanders were found to be satisfactory in every respect. The type used was 1/8-inch long and acted as a vector force directed along the line of orientation of the crystal. The crystal was mounted in a 3/16-inch diameter hole drilled through the plate. The crystal was held against the interior of the hole by a rubber band which was stretched prior to insertion of the crystal and then allowed to contract, the increased thickness holding the crystal firmly.

The 1/8-inch Clevite PZT-5 piezoelectric crystal has a resonant frequency near 350 kilohertz. If this frequency falls within the passband of interest, some measure must be taken to dampen the resonant ringing. This can be done by backing the crystal with ordinary modeling clay. In the present study, the resonant frequency was well outside the 20 to 200 kilohertz passband and was not evident on the seismograms; thus the bulky backing was not necessary and only the 1/8-inch crystal itself needed to be applied to the interior of the small hole.

In implanting the crystal in the plate, some care was taken to place the crystal face squarely against the hole edge and in good contact with the aluminum portion of the composite plate. Otherwise, asymmetric or low-level signals could be generated. Good contact was aided by filing slightly the interior of the hole to remove the curvature at the point of contact.

Since making a hole in the model was necessary to implant a source at depth, a preliminary experiment was conducted to determine the effect of a previously drilled hole in the vicinity of a source location. A 3/16-inch diameter hole was drilled in a 48 inches by 36 inches by 0.040 inch sheet of aluminum, the center of the hole being 1.0 inch from one edge. A horizontal source was mounted in the hole, and a seismogram was recorded. A second hole was then drilled 2.25 inches to the side of the first hole, but not in the travel path. The source was then located in the second hole and another seismogram was recorded. The resulting seismograms were essentially identical, indicating that any reflected or scattered energy resulting from the superfluous hole is not measurable at the operating system amplification.

It was the procedure to conduct the main body of experiments in a sequence such that no hole was ever located along a travel path, but was always located to the rear of the source, as in the described preliminary experiment.

The Receiver

A Clevite 1/8-inch PZT-4 ceramic crystal was used as the sensing element and was backed and amplified as shown in Figure 8. The crystal and amplifier were mounted in a small carriage which rode upon the upper edge of the model. Gravity was sufficient to hold the crystal in good contact with the plate edge, although care was taken to place the crystal face squarely against the plate edge. Failure to do this will result in the loss of some high frequency energy.

The Modeling Electronics

A block diagram of the modeling electronics is shown in Figure 9. The piezoelectric crystal is activated by a Thyratron pulser which generates a step-function voltage at a prescribed (but variable, if desired) rate. The positive voltage step causes the ceramic transducer to expand and thus to generate elastic waves at the point of contact with the plate. The Thyratron is set to generate a new signal at a

rate of several tens of times per second. A delayed version of the Thyratron excitation pulse is used to trigger a sampling oscilloscope which displays the signal after recording. Prior to oscilloscope display, the recorded signal is amplified and filtered so that the effective passband is 20 to 200 kilohertz. Thus, signal periods are in the range of 5 to 50 microseconds, and travel times are generally a few hundred microseconds. A paper copy of the seismogram on an expanded time scale was routinely obtained by means of a wave translation feature. Upon activation of a switch, a sampling pulse proceeds to sweep across the stored signal at a slow, regulated speed which is coordinated with the paper chart speed. The resulting paper seismogram has a time base of 42.86 μs per inch.

The influence of the frequency responses of the source, the receiver, and of the filtering and amplification electronics on the spectrum of the model Rayleigh signal can be seen in Figure 10. This spectrum was obtained by placing the source and the receiver immediately adjacent to each other, thus eliminating the response of the medium from the system. Also shown in Figure 10 is the spectrum from a typical seismogram recorded at Grand Saline. The frequency response of the seismograph has not been removed. Note that the model spectrum appears to

be a close approximation to a smoothed version of the actual spectrum. This indicates that the model transducers and electronics produced a spectrum, which when adjusted by the model time scale factor, encompasses the frequency range of interest.

Digitization

The wave transformed output was routed to a digitizer which was interfaced with an XDS-925 computer. The analog data were amplified by a factor of 10 to boost the signal into the $\pm$ 10 volt range required by the digitizer, and were passed through an anti-aliasing filter to remove noise at a scaled period below 10 seconds. A sampling trigger was supplied to the digitizer from the Thyratron pulser after delaying and conditioning the pulse. A 1200 μs delay was introduced to allow for settling time of the sample-and-hold amplifier. The delayed pulse was conditioned to provide a sampling trigger of +10 volts amplitude and 2.5 μs duration.

By suitably adjusting the Thyratron repitition rate and allowing for the time scale factor and the wave translation time factor, the resultant signal was sampled once per second.

Spectral Determinations

The digitized seismograms were written on magnetic tape

in a format compatible with data processing programs which were already being used on the real seismograms recorded at Grand Saline. One of these programs, a point transform technique (Filon, 1928) was used to calculate the Rayleigh spectra obtained in this study. This method evaluates the Fourier integral of the desired time series by dividing the time series into 2N equal parts with an interval h equal to the sampling interval. It is assumed that over the 2N range the time series can be approximated with sufficient accuracy by a parabola. Since the parabola is constrained at three points (the three sample values), the arbitrary constants or the parabola are uniquely determined and can be expressed in terms of the adjacent sample values and the sample interval. The integrals over each 2N range can then be evaluated analytically by parts and can be combined to give the total integral. Contrary to the Fast Fourier Transform (e.g., Welch, 1967), the Filon technique allows the transform to be calculated at any desired frequency. No smoothing function was applied to the spectra since the Rayleigh wave is assumed to be a unique entity, having a beginning and an end, and not to be a sample selected from an infinite set as is usually the assumption in spectral analyses of seismic time series.

After computation, the spectra were automatically plotted by a 7126 XDS plotter. The specific quantity plotted was the square root of the sum of the squares of the real and the imaginary parts of the transform expressed in decibels relative to a convenient value fixed by the dynamic range of the digital recording system.

Preliminary Experiments

The aluminum alloy used to build the model was 2024-T3. The Rayleigh velocity of the alloy was determined by measuring the travel times over several distances. The reciprocal of the slope of the best fit straight line was taken as the Rayleigh velocity. However, the scatter of the data points was so small that subsequent velocity measurements were made at only one distance.

To verify formula 1, composite plates of aluminum and vinyl were constructed for each of the three thickness combinations shown in Figure 7. The elastic velocities shown in Figure 6 were then determined by measuring the travel times over a 400 millimeter distance.

A surface source on an aluminum-vinyl half-space duplicates the classical theoretical problem of Lamb (1904). Figure 11 shows the model seismogram and Lamb's theoretical result.

The close correspondence of the two indicates that the composite plate does indeed act as a half-space. That is, there is no modal propagation within the separate vinyl layers, no body wave dispersion which would result if the total plate thickness were large compared to the smallest wave lengths, nor is there evidence of asymmetrical mode propagation. To demonstrate the undesirable asymmetric mode, the thickness expander source was applied transversely to the aluminum plate. Figure 12 shows the result. The very long period inversely dispersed wave train is unmistakable.

It is interesting to compare the model results for a source at depth within a homogeneous half-space, represented by an aluminum plate, with Lapwood's (1949) theoretical results. Lapwood considered a cylindrical explosion as a source at a depth h. Figure 13 shows a model seismogram for the case where both shear and compressional waves are generated by the source and have travelled a distance x which is large compared to depth h. The fact that the source is located below the surface introduces several phase arrivals which are not present in Lamb's problem. The phase denoted as sP has travelled from the source to the surface as a shear wave and has then been refracted along the surface as a compressional wave. The phase pS travelled

to the surface as a compressional wave and along the surface as a shear wave. The arrival times of each phase as given by Lapwood in terms of x, h, and the shear and compressional velocities of the half-space are indicated in the figure. Each of the theoretically predicted phases can be observed on the model seismogram and are seen to be arriving at the times determined by Lapwood. Since the theoretical source space and time function are different from the model source, no exact similarity can be expected between the corresponding phase wave forms.

RAYLEIGH SPECTRA ORIGINATING FROM FOCI IN LATERALLY HOMOGENEOUS LAYERED MEDIA

As can be seen from the sketch of the model in Figure 6, it was possible to place sources in the laterally homogeneous portion of the model, as well as in the downward bent portion of the model lithosphere. This was done in order to establish a set of standard spectra with which to compare the spectra originating from the lithospheric wedge, and also to compare in a qualitative way with theoretical spectra.

Rayleigh waves were recorded at a distance of 800 millimeters, scaled distance of 2667 kilometers, from sources at the surface, and at scaled depths of 50 and 250 kilometers. The distance of 800 millimeters was convenient for two reasons. It was short enough that no compressional wave reflections from the plate edges could interfere with the Rayleigh wave arrival. It was, however, several times larger than the longest wave lengths of interest and therefore allowed comparison of the results with far-field theory.

Figure 14 shows the seismogram of a Rayleigh wave from a vertical surface force. The spectrum of the Rayleigh wave is shown in Figure 15. The time window from which the signal

spectrum was taken is shown in Figure 14. Above the noise the spectrum is perfectly smooth, but at a level where the noise dominates, the spectrum becomes unstable. Note that the signal-to-noise ratio is about 30 dB near the middle of the pass-band.

It is interesting to compare the Rayleigh spectrum with a theoretically predicted spectrum for a laterally homogeneous oceanic structure. Such a spectrum is presented by Harkrider and Anderson (1966) for a vertical surface source. For comparative purposes the theoretical spectrum must be adjusted for the model source spectrum and for the model attenuation as a function of frequency and distance. By comparing the spectrum in Figure 15 with the source spectrum in Figure 10 the attenuation with distance of each frequency can be determined. The spectra are the same at periods greater than 55 seconds, but at smaller periods there is significant attenuation with travel path. Table 2 shows amplitude attenuation in dB as a function of scaled travel path distance. By applying these attenuation factors to the Harkrider and Anderson theoretical spectrum and adjusting the resultant for the model source spectrum, the theoretical spectra can be directly compared to the model spectrum for the same depth.

The dotted curve in Figure 15 shows the theoretical spectrum

TABLE 2

Period (sec)	Attenuation (dB/km)
20	.01900
30	.00600
40	.00075
50	.00033
55	.00000
60	.00000
70	.00000
80	.00000
90	.00000
100	.00000

for the surface vertical force. Figures 16, 17 and 18 show similar comparisons for a horizontal force at a depth of 50 kilometers, a vertical force at 50 kilometers, and a horizontal force at 250 kilometers, respectively. The spectra are normalized at a period of 40 seconds. The spectra shown in Figure 16 are particularly interesting. The theoretical spectrum for the horizontal force at a depth of 50 kilometers shows a zero at a period of 60 seconds. The model spectrum also shows the zero, but it has been filled in to the noise level; the noise also causes a slight shift in the period at which the 'hole' appears to occur. The secondary peaks of the two spectra, occurring at a period of about 85 seconds, match very well. It should be noted that the theoretical spectra are computed on the basis of a very detailed version of the Toksoz and Anderson (1966) oceanic structure while the seismic model is merely a four-layer simplification. Thus, the comparison of theoretical and model spectra cannot be considered as a rigorous demonstration of the fidelity of the model construction. Nevertheless, the very close agreement between the model spectra and the theoretical spectra for all source depths indicates that surface wave generation and propagation in the laterally homogeneous portion of the model are correctly scaled to represent phenomena in an oceanic structure.

SPECTRA OF RAYLEIGH WAVES FROM SOURCES IN THE LATERALLY HETEROGENEOUS ZONE

Sources were located at scaled depths of 0, 50, 150, and 250 kilometers in the downward bent portion of the model lithosphere. Figure 19 shows the source locations in relations to the geometry of the anomalous zone. Note that the line of foci is somewhat to the top of center of the lithosphere. It has been proposed that all earthquakes occur in the upper 20 kilometers (Isacks, Oliver, and Sykes, 1968) of the downgoing slab, and alternatively that the earthquakes occur nearer the center along the axis of cooler temperatures (e.g., McKenzie, 1969; Griggs, 1972). There does not appear to be sufficient evidence to distinguish between the two suggestions at this time. In this study the latter hypothesis was followed, although it is unlikely that it would make much difference since the spectra for sources at 0 and 50 kilometers depth in the laterally homogeneous zone are almost the same.

A Rayleigh spectrum from a vertical surface force at a scaled distance of 2667 kilometers is shown in Figure 20. There appears to be no difference between this spectrum and the spectrum of the surface source in the laterally homogeneous portion of the model, which is shown in the same figure for

comparison. Similarly, the Rayleigh spectrum from a vertical force above the dipping lithosphere at a scaled depth of 50 kilometers, shown in Figure 21 is very similar to the analogous spectrum from a source at a depth of 50 kilometers in the laterally homogeneous area, which is also shown in the figure.

Figure 22 shows the spectrum of a Rayleigh wave from a horizontal force at a scaled depth of 250 kilometers in the anomalous zone. Also shown, by alternating dots and dashes, is the theoretical curve for the same source in laterally homogeneous media and, by a solid line, the model results for the same source in laterally homogeneous media. The solid and the dot-dash spectra are almost coincident in the passband 30 to 100 seconds, indicating that the model and theoretical results for laterally homogeneous source areas and travel paths are in agreement. Below a period of 30 seconds, the model signal spectrum becomes lost in the noise. Comparison of the solid-lined spectrum of the source in the downward bent lithosphere to the other two spectra indicates a significant enhancement of energy in the period range 30 to 60 seconds. With the amplitudes equalized along the long-period side of the spectra, there is about 16 dB more amplitude for the dipping lithosphere source at a period of 30 seconds. There is 7 dB more amplitude at 40 seconds and 5 dB

more at 50 seconds, with the curves converging at 60 seconds. The source depth of 250 kilometers is well below the bend in the lithosphere, and it appears that wave lengths as large as twice the width of the lithosphere are utilizing it as a waveguide to the surface.

Focal mechanism studies of earthquakes in island arcs (Isacks, Oliver, and Sykes, 1968) indicate that the compressive axes of earthquakes occurring below the bend in the lithosphere are generally aligned along the dip of the lithosphere. Accordingly, a piezoelectric crystal was situated at a scaled depth of 250 kilometers so that the axis of compression was along the dip of the model lithosphere. The resulting Rayleigh spectrum is shown in Figure 23, where it is compared with the 250 kilometer source in the layered half-space. This orientation of the source also shows the spectral shift to higher frequencies caused by the location of the source in the anomalous zone relative to the location in the layered half-space.

To determine the behavior of the Rayleigh spectrum nearer to the bend in the lithosphere, a source was situated at a scaled depth of 150 kilometers in the anomalous zone. The Rayleigh spectrum is shown in Figure 24, along with previously shown spectra for sources at 50 kilometers and 250 kilometers deep in the anomalous zone. The bend in the model lithosphere occurs

at a depth of 100 kilometers, so that Figure 24 represents spectra from sources 50 kilometers above the bend, 50 kilometers below the bend, and 150 kilometers below the bend. This figure illustrates the change in the Rayleigh spectrum with increasing source depth in the dipping lithosphere and can be contrasted to Figure 25 which shows the spectral shift occurring with increasing source depth in the laterally homogeneous portion of the model. The spectra shown in Figures 20 through 25 are normalized at a period of 55 seconds. In the layered half-space there is a significant and theoretically predictable spectral shift to longer periods with increasing source depth. For sources in the dipping lithosphere, there is no corresponding shift of the spectral peak; indeed, the shape of the spectra are very similar at periods less than 60 seconds, with the most obvious effect of increasing source depth being the relative increase in energy in the period range 60 to 100 seconds. Thus, in the dipping lithosphere, there is a relative broadening of the spectral peak to the long period side with increasing source depth, but little accompanying decrease on the short period side, at least to a depth of 250 kilometers. The spectral change with increasing source depth illustrated in Figure 24 is interpreted to mean that wave lengths as large as twice the width of the lithosphere

are utilizing the dipping lithosphere as a waveguide to the surface, while larger wave lengths are not enhanced and tend to behave as if the sources were at similar depths in a layered half-space.

DISCUSSION

Simple one-directional forces were used as the model sources to produce the Rayleigh spectra. This was done to keep the source as simple as possible while studying the effect of the source region. However, focal mechanism studies (Isacks, Oliver, and Sykes, 1968) show that a double couple, or shear dislocation, is a more realistic source function. For that reason a quantitative comparison of the model Rayleigh spectra with spectra of real earthquakes recorded at Grand Saline is not warranted. Nevertheless, some interesting qualitative observations can be made.

As noted earlier, the Grand Saline spectra are characterized by rapid changes of slope and "holes" within the signal passband of 20 to 100 seconds. The holes are often of sufficient relief to effectively mask possible depth-dependent spectral zeroes resulting from source displacement nodes. The model spectra are devoid of holes other than the theoretically-predicted energy zero at 60 seconds for a horizontal source at a depth of 50 kilometers. Nc smoothing function was used on either the real or the model spectra. The model results indicate that the holes in the real spectra are not due to interference phenomena associated with source location in the anomalous zone. It seems likely that the holes result from interference effects due to

lateral refraction along the propagation path. The presence of the holes could prove a serious obstacle to the use of frequency-dependent spectral zeroes to determine focal depth.

The fact that Rayleigh spectra from foci above the dipping portion of the lithosphere are not significantly different from spectra from foci at the same depths in the layered half-space implies that current theories of spectral determination based on a laterally homogeneous layered media are adequate for shallow events in island arc regions, the focal depth limit of applicability probably being equal to the thickness of the lithosphere. Since the lithosphere thickness may vary from arc to arc, the depth limit of applicability would vary accordingly.

Because of size limitations of the model, no seismograms could be recorded on the backward side of the island arc. The Grand Saline data suggest that the waveguide effect is not operative in that direction, although the degree of conformity of such spectra with layered media theory is problematical. At any rate, spectra for earthquakes occurring below the bend in the lithosphere are no doubt dependent on azimuth. Surface wave magnitudes (Ms) are known to have an azimuthal dependence, but this has been attributed completely to the radiation pattern of the source function. While source radiation pattern

may be the controlling factor for shallow earthquakes, the effect of the geometry of the source region must be considered for intermediate and deep focus earthquakes. For a given source function, the higher values of Ms would be observed at azimuths opposite to the direction of dip of the lithospheric plate.

The technique of utilizing a two-dimensional model made by face joining two or more materials of different elastic properties has proven to be a practical and flexible method of formulating structures of geophysical interest. It should find other applications in situations where it is desired to investigate the effect on seismic phenomena of zones of great lateral structural variation, such as mid-ocean ridges and continental boundaries.

ACKNOWLEDGEMENTS

Funds for this research were provided by the Air Force Office of Scientific Research under Grant 71-2133B. I wish to thank Mr. C. D. McClure and the Mobil Field Research Laboratory for providing much of the seismic modeling equipment. Ian Harris, Frank Van Leer, and Karl Thomason were of great assistance in maintaining the analog electronics, and John Lobdell was helpful with the computer software. Darrell Rasmussen and Nancy Cunningham helped with computer operations. John McDonald made many helpful suggestions. This work could not have been completed without the encouragement and assistance of Professor Eugene Herrin.

REFERENCES

Angona, F. A., Two-dimensional modeling and its application to seismic problems, Geophysics, 25, 468-482, 1960.

Ben-Menahem, A., and D. G. Harkrider, Radiation patterns of seismic surface waves from buried dipolar point sources in a flat stratified Earth, J. Geophys. Res., 69, 2605-2620, 1964.

de Bremaecker, J. C., Transmission and reflection of Rayleigh waves at corners, Geophysics, 23, 253-266, 1958.

Filon, L. N. G., On a quadrature formula for trigonometric integrals, Proc. Roy. Soc. Edin., 49, 38-47, 1928.

Gangi, A. F., Experimental determination of P wave/Rayleigh wave conversion coefficients at a stress free wedge, J. Geophys. Res., 72, 5685-5692, 1967.

Griggs, D. T., The sinking lithosphere and the focal mechanism of deep earthquakes, The Nature of the Solid Earth, McGraw-Hill, New York, pp. 361-383, 1972.

Harkrider. D. G., Surface waves in multilayered elastic media, 1, Rayleigh and Love waves from buried sources in a multilayered elastic half-space, Bull. Seismol. Soc. Am., 54, 627-679, 1964.

Harkrider, D. G., Surface waves in multilayered elastic media, 2, Higher mode spectra and spectral ratios from point sources in plane layered Earth models, Bull. Seismol. Soc. Am., 60, 1937-1987, 1970.

Harkrider, D. G., and D. L. Anderson, Surface wave energy from point sources in plane layered Earth models, J. Geophys. Res., 71, 2967-2980, 1966.

Isacks, B., Jack Oliver, and L. R. Sykes, Seismology and the new global tectonics, J. Geophys. Res., 73, 5855-5899, 1968.

Knopoff, L., and A. F. Gangi, Transmission and reflection of Rayleigh waves by wedges, Geophysics, 25, 1203-1214, 1960.

Kuo, J. T., and G. A. Thompson, Model studies on the effect of a sloping interface on Rayleigh waves, J. Geophys. Res., 68, 6187-6197, 1963.

Lamb, H., On the propagation of tremors over the surface of an elastic solid, Phil. Trans. Roy. Soc. (London) A, 203, 1-42, 1904.

Lapwood, E. R., The disturbance due to a line source in a semi-infinite elastic medium, Phil. Trans. Roy. Soc. (London) A, 242, 63-100, 1949.

McKenzie, D. P., Speculations on the causes and consequences of plate motions, Geophys. J., 18, 1-15, 1969.

Oliver, Jack, Frank Press, and Maurice Ewing, Two-dimensional model seismology, Geophysics, 19, 202-219, 1954.

Ottaviani, M., Elastic wave propagation in two evenly-welded quarter-spaces, Bull. Seis. Soc. Am., 61, 1119-1152, 1971.

Riznichenko, Y. V., O. G. Shamina, and R. V. Khanutina, Elastic waves with generalized velocity in two dimensional bimorphic models, Bull. Acad. Sci., USSR, Geophys. Ser. (English translation), 321-334, 1961.

Toksoz, M. N., and D. L. Anderson, Phase velocities of long-period surface waves and structure of the upper mantle, 1, Great-circle Love and Rayleigh wave data, J. Geophys. Res., 71, 1641, 1966.

Welch, P. D., The use of the fast Fourier transform for the estimation of power spectra: A method based on time averaging over short, modified periodograms, IEEE Transactions on Audio and Electroacoustics, AU-15, 2, 70-73, 1967.

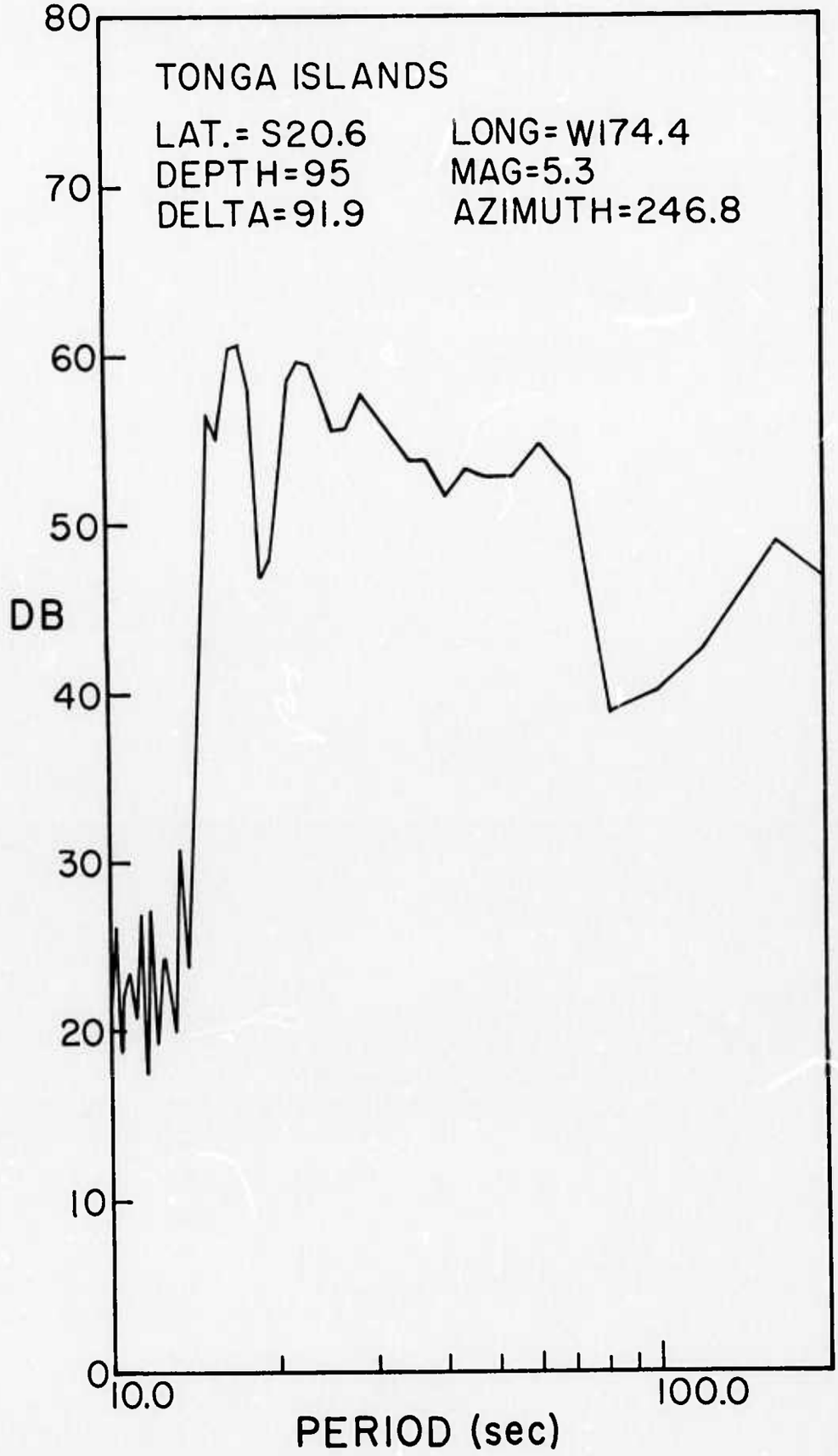
TONGA ISLANDS
LAT.= S20.6
LONG= W174.4
DEPTH=95
MAG=5.3
DELTA=91.9
AZIMUTH=246.8
80
70
60
50
40
30
20
10
0
DB
10.0
100.0
PERIOD (sec)

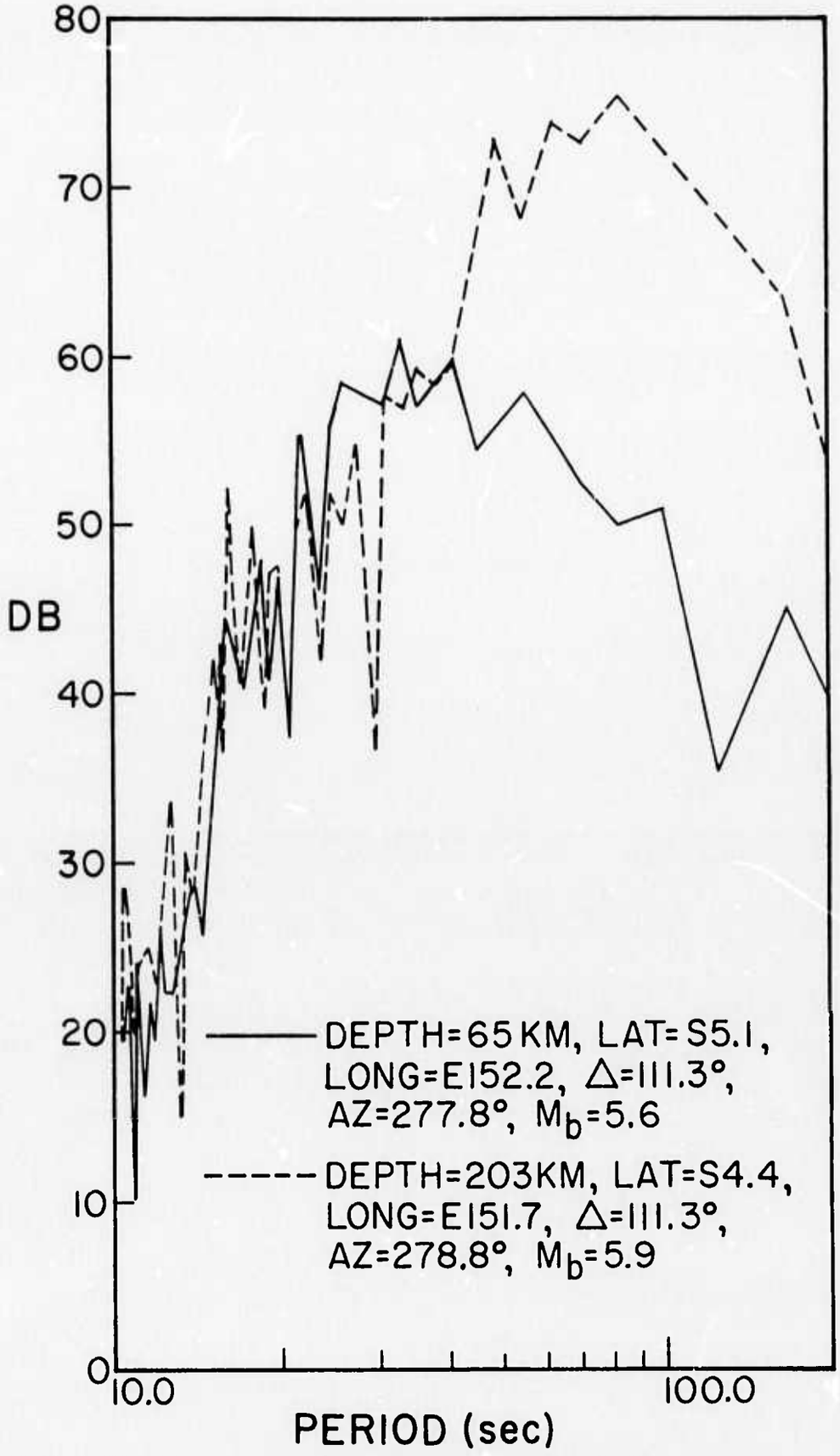
80
70
60
50
DB
40
30
20
10
0
10.0
100.0
PERIOD (sec)
DEPTH=65KM, LAT=S5.1,
LONG=E152.2, Δ=111.3°,
AZ=277.8°, M_b=5.6
DEPTH=203KM, LAT=S4.4,
LONG=E151.7, Δ=111.3°,
AZ=278.8°, M_b=5.9

131<

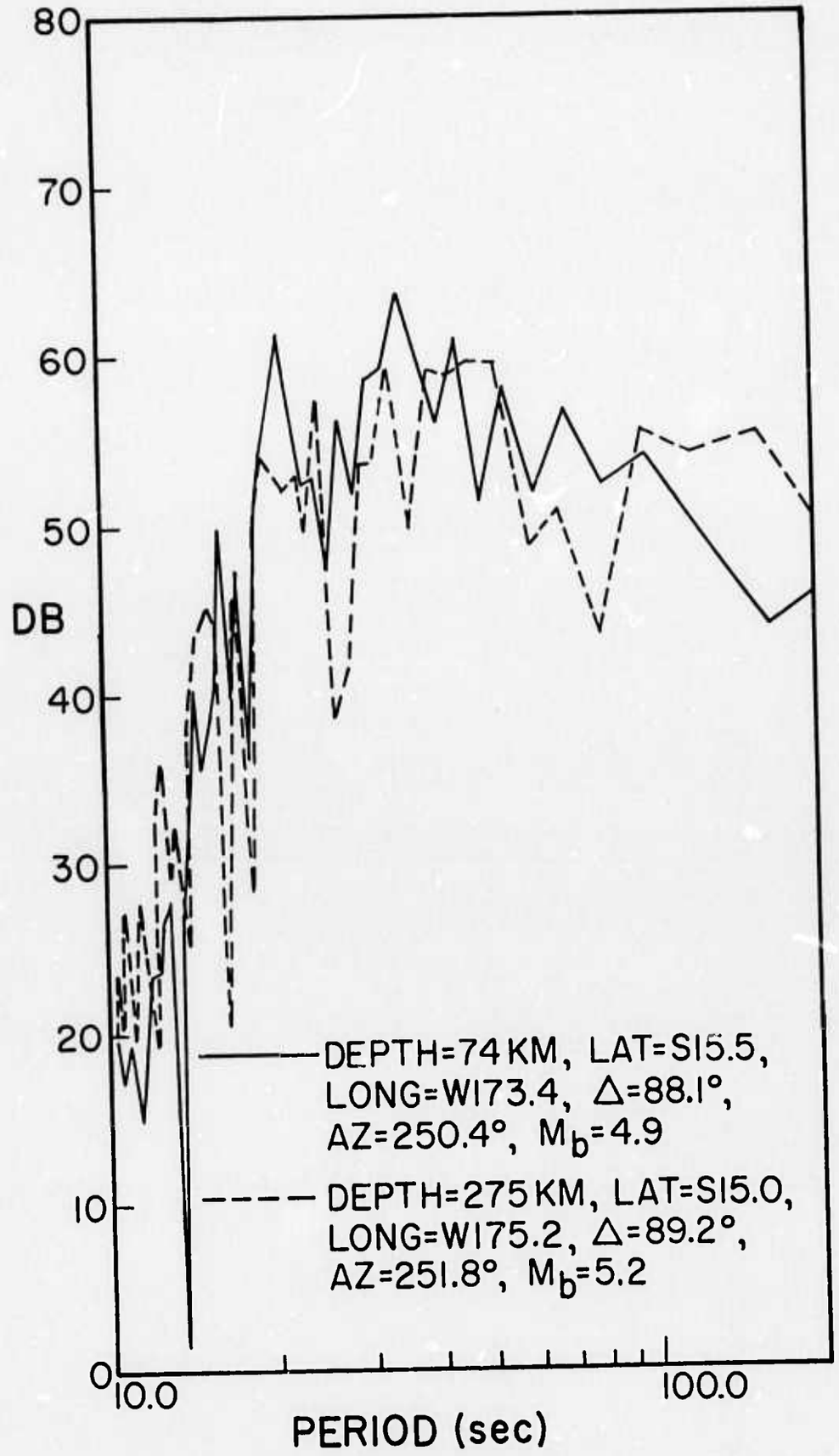
80
70
60
50
DB
40
30
20
10
0
10.0
100.0
PERIOD (sec)
DEPTH=74 KM, LAT=S15.5,
LONG=W173.4, Δ=88.1°,
AZ=250.4°, M_b=4.9
DEPTH=275 KM, LAT=S15.0,
LONG=W175.2, Δ=89.2°,
AZ=251.8°, M_b=5.2

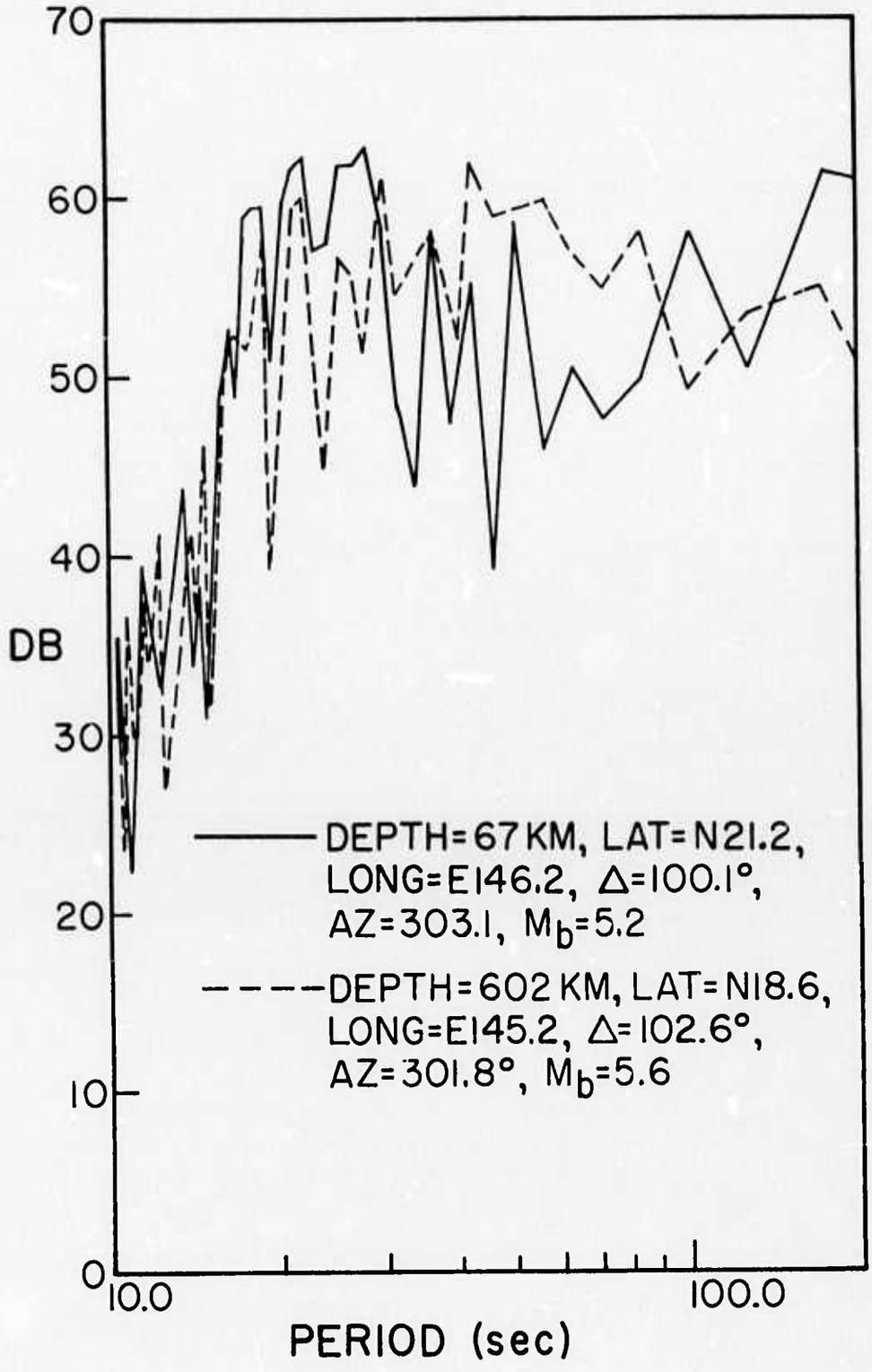
70
60
50
40
30
20
10
0
DB
10.0
100.0
PERIOD (sec)
DEPTH=67 KM, LAT=N21.2,
LONG=E146.2, Δ=100.1°,
AZ=303.1, Mb=5.2
DEPTH=602 KM, LAT=N18.6,
LONG=E145.2, Δ=102.6°,
AZ=301.8°, Mb=5.6

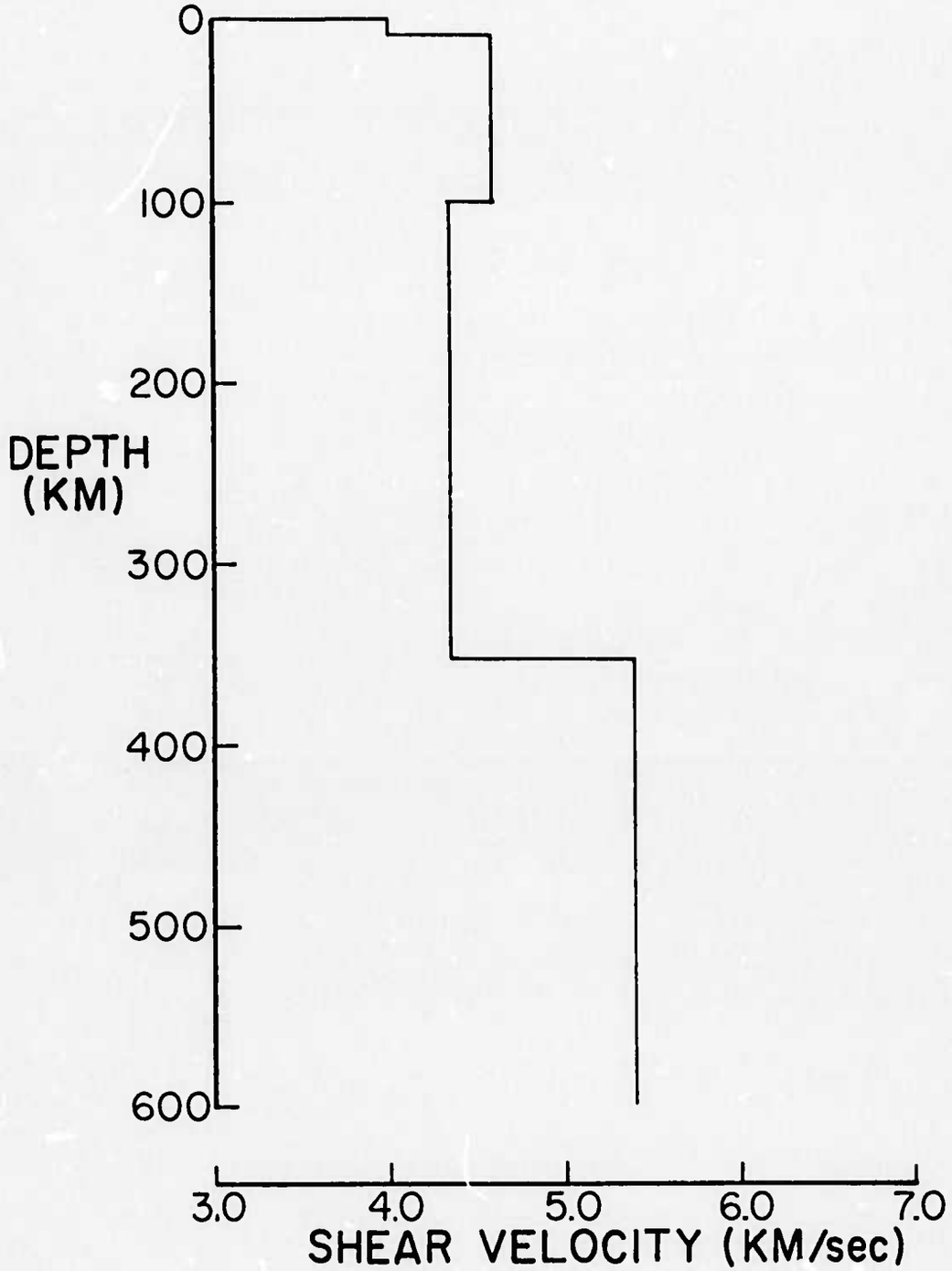
0
100
200
DEPTH
(KM)
300
400
500
600
3.0
4.0
5.0
6.0
7.0
SHEAR VELOCITY (KM/sec)

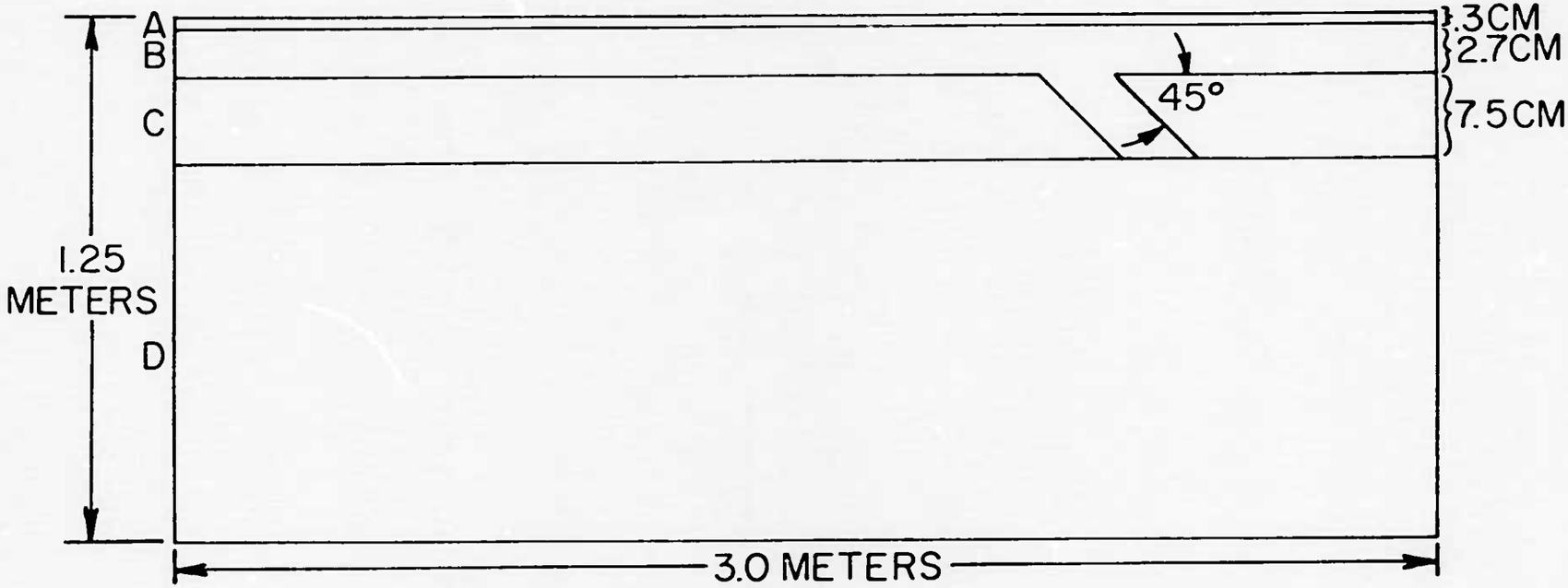

ZONE	V_p	β	VINYL / ALUMINUM	SCALED THICKNESS (KM)
A	4.14	2.39	1.6	10
B	4.78	2.76	0.8	90
C	4.57	2.64	1.1	250
D	5.48	3.24	0	

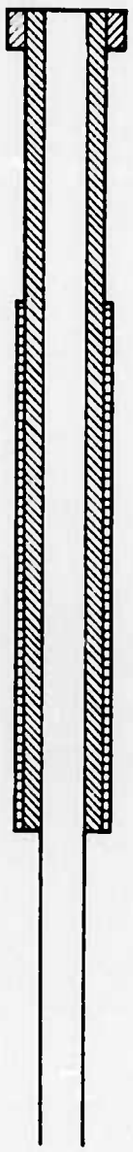

.040 IN. ALUMINUM
.016 IN. VINYL
.016 IN. VINYL
.006 IN. VINYL

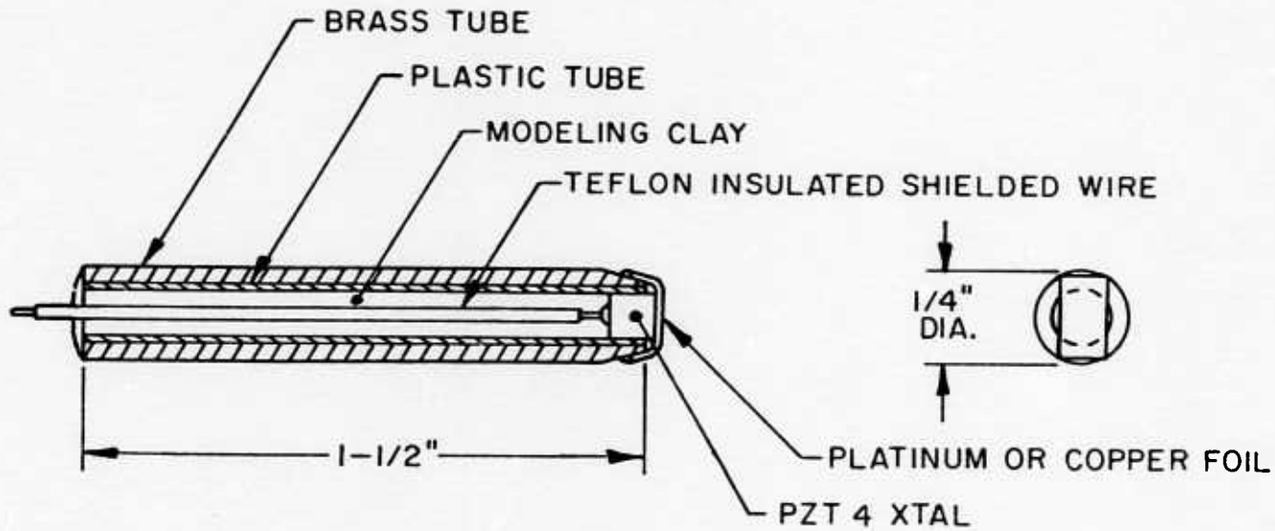
BRASS TUBE
PLASTIC TUBE
MODELING CLAY
TEFLON INSULATED SHIELDED WIRE
1/4"
DIA.
1-1/2"
PLATINUM OR COPPER FOIL
PZT 4 XTAL

RECEIVER

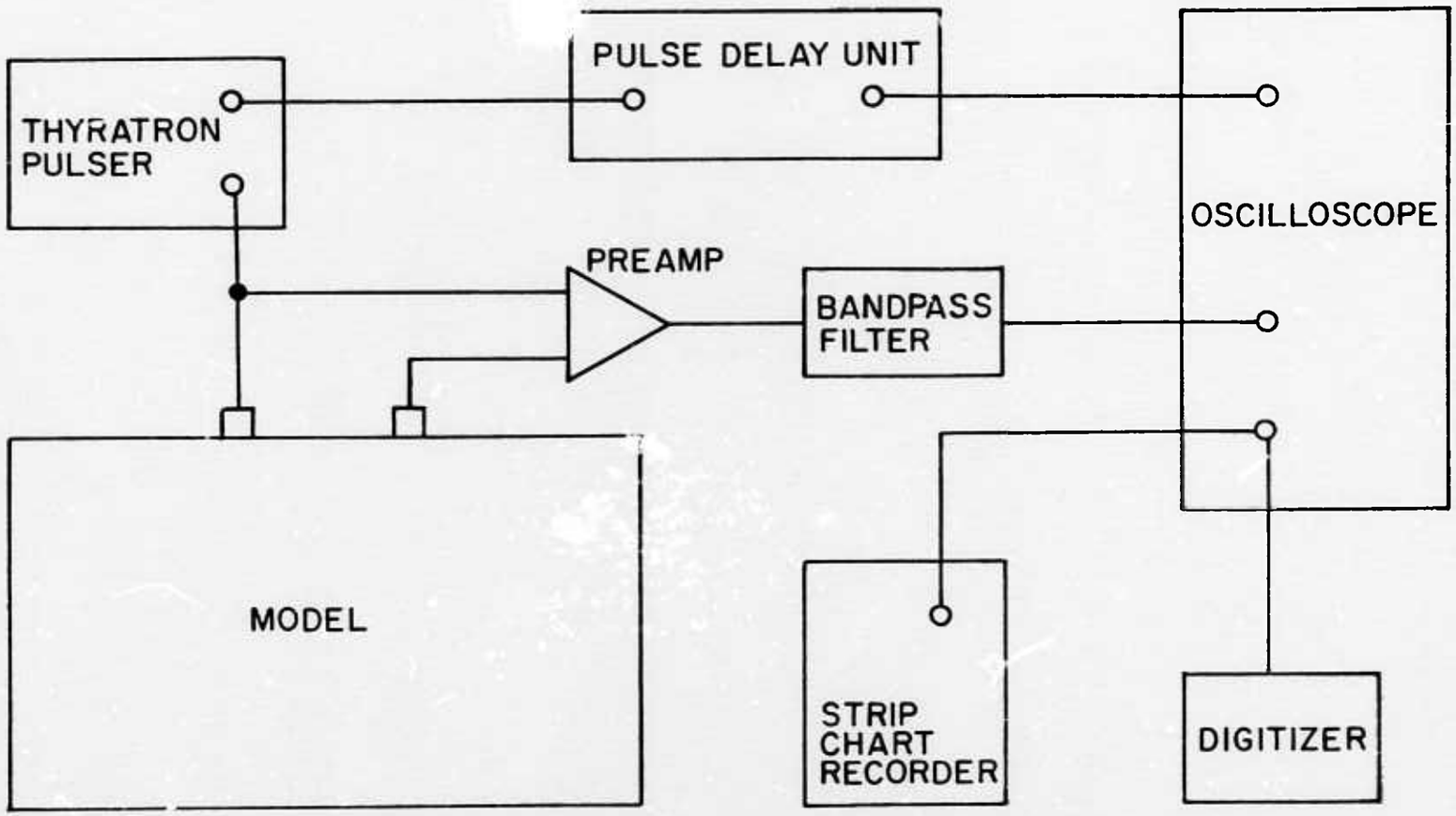
PULSE DELAY UNIT
THYRATRON PULSER
OSCILLOSCOPE
PREAMP
BANDPASS FILTER
MODEL
STRIP CHART RECORDER
DIGITIZER

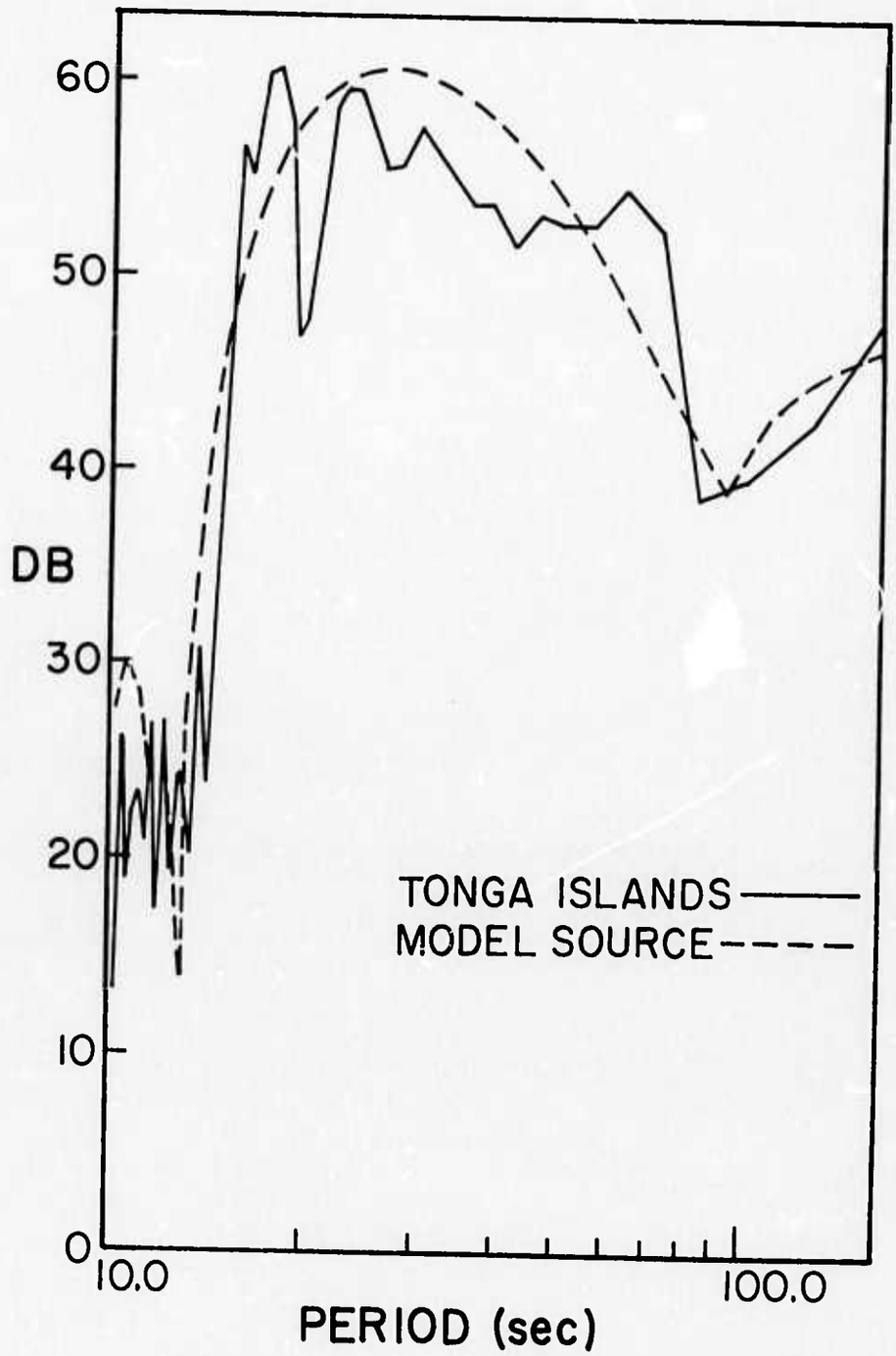
60
50
40
DB
30
20
10
0
10.0
100.0
PERIOD (sec)
TONGA ISLANDS
MODEL SOURCE

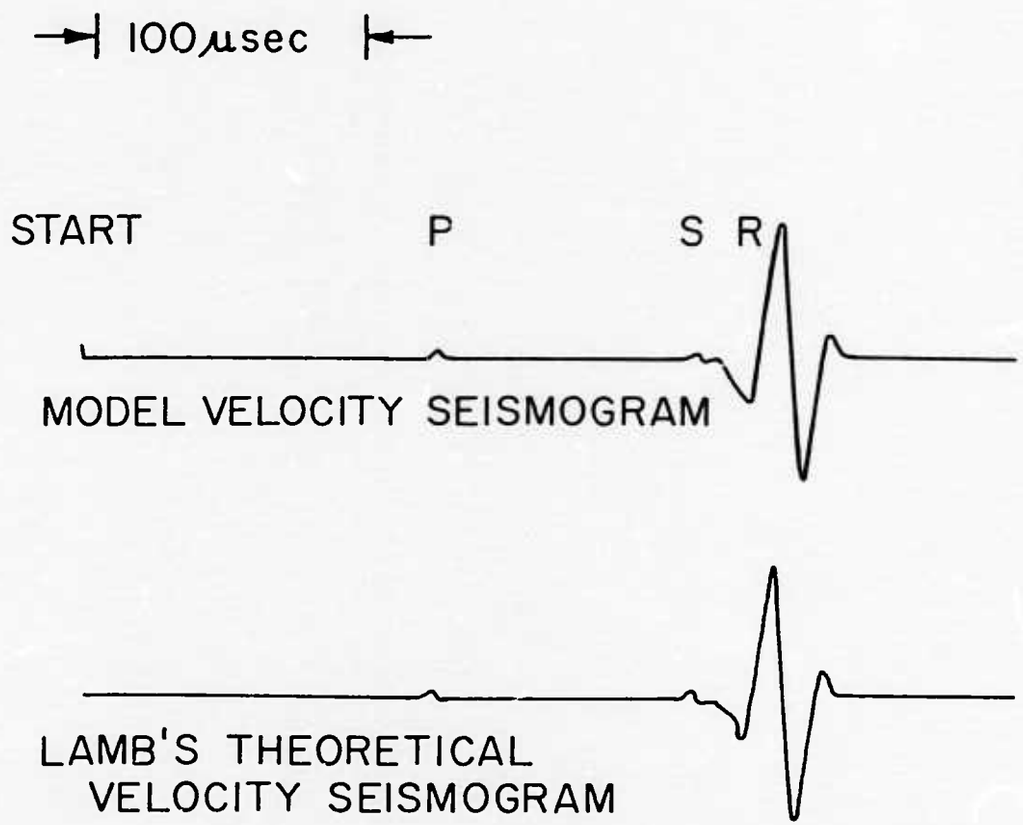
100μsec
START
P
S R
MODEL VELOCITY SEISMOGRAM
LAMB'S THEORETICAL
VELOCITY SEISMOGRAM

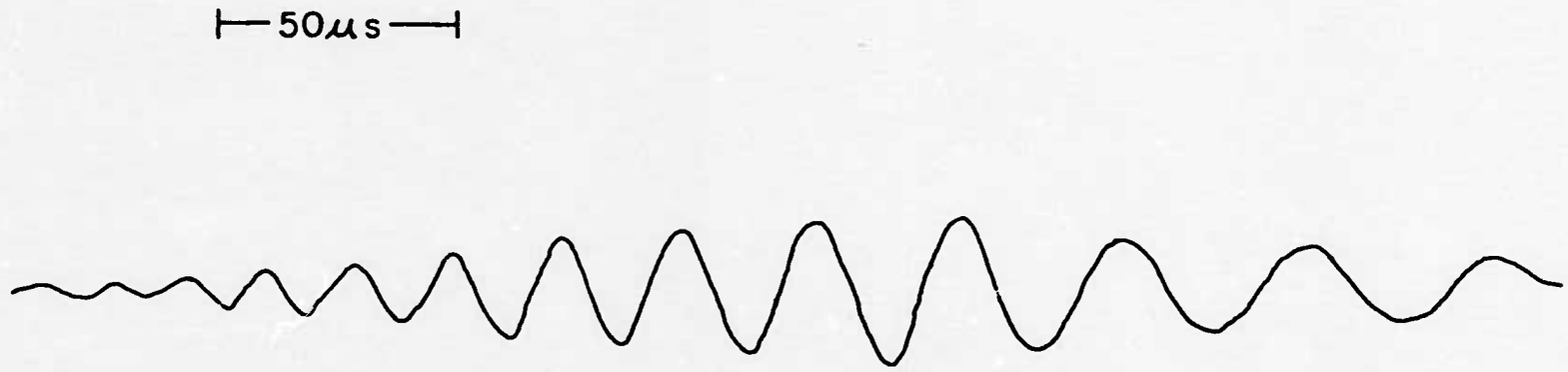

FLEXURAL WAVE

141<

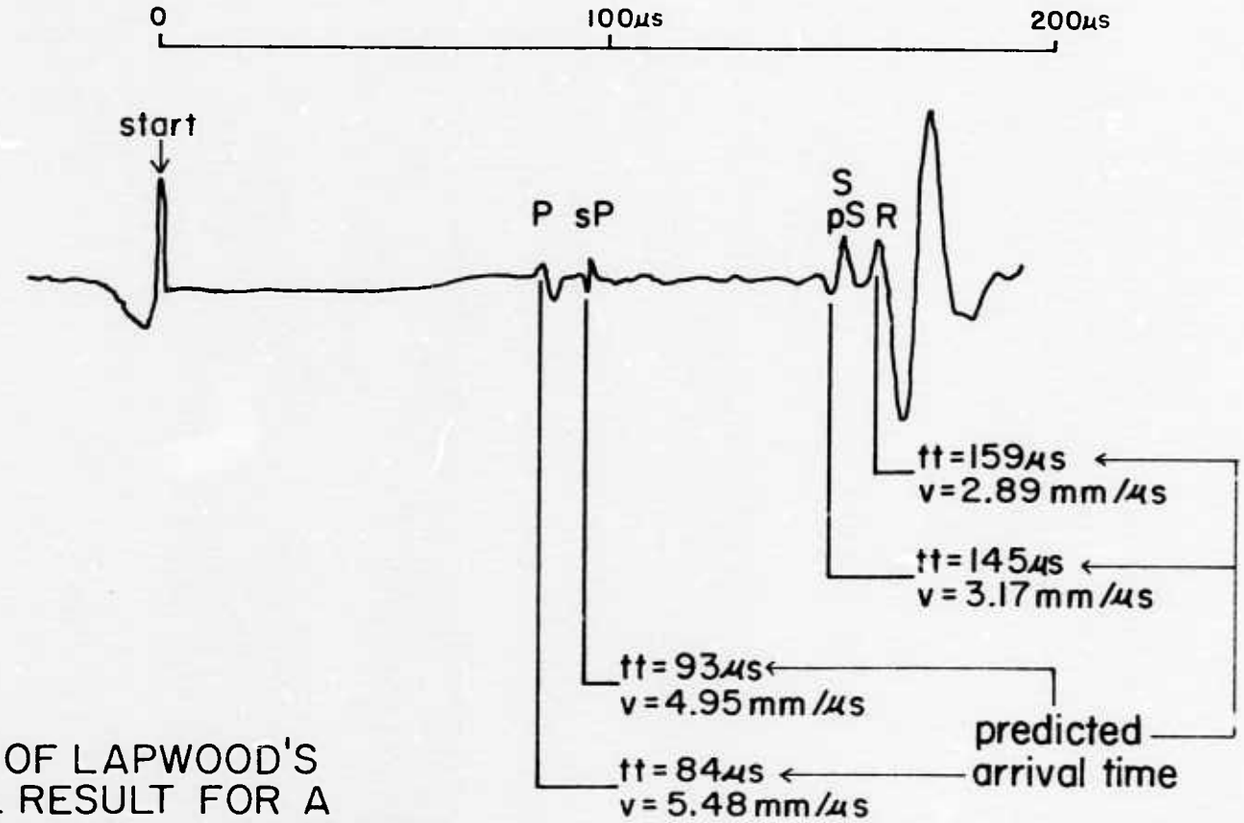

VERIFICATION OF LAPWOOD'S THEORETICAL RESULT FOR A BURIED SOURCE IN A HALF-SPACE

$x = 460\,mm$

$h = 40\,mm$

$R = 2.91\,mm/\mu s$

$\alpha = 5.48\,mm/\mu s$

$\beta = 3.19\,mm/\mu s$

142

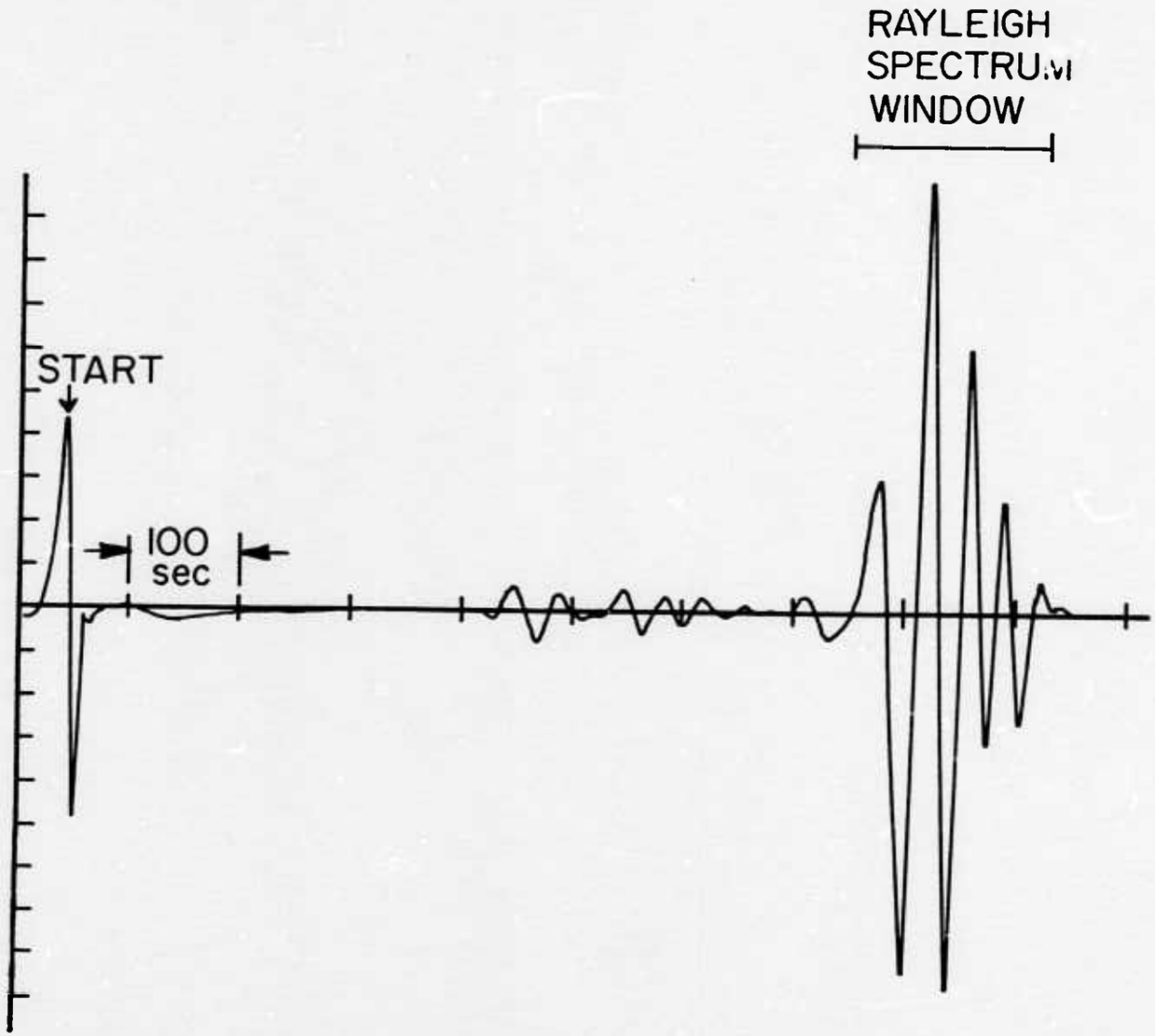
RAYLEIGH
SPECTRUM
WINDOW
START
100
sec

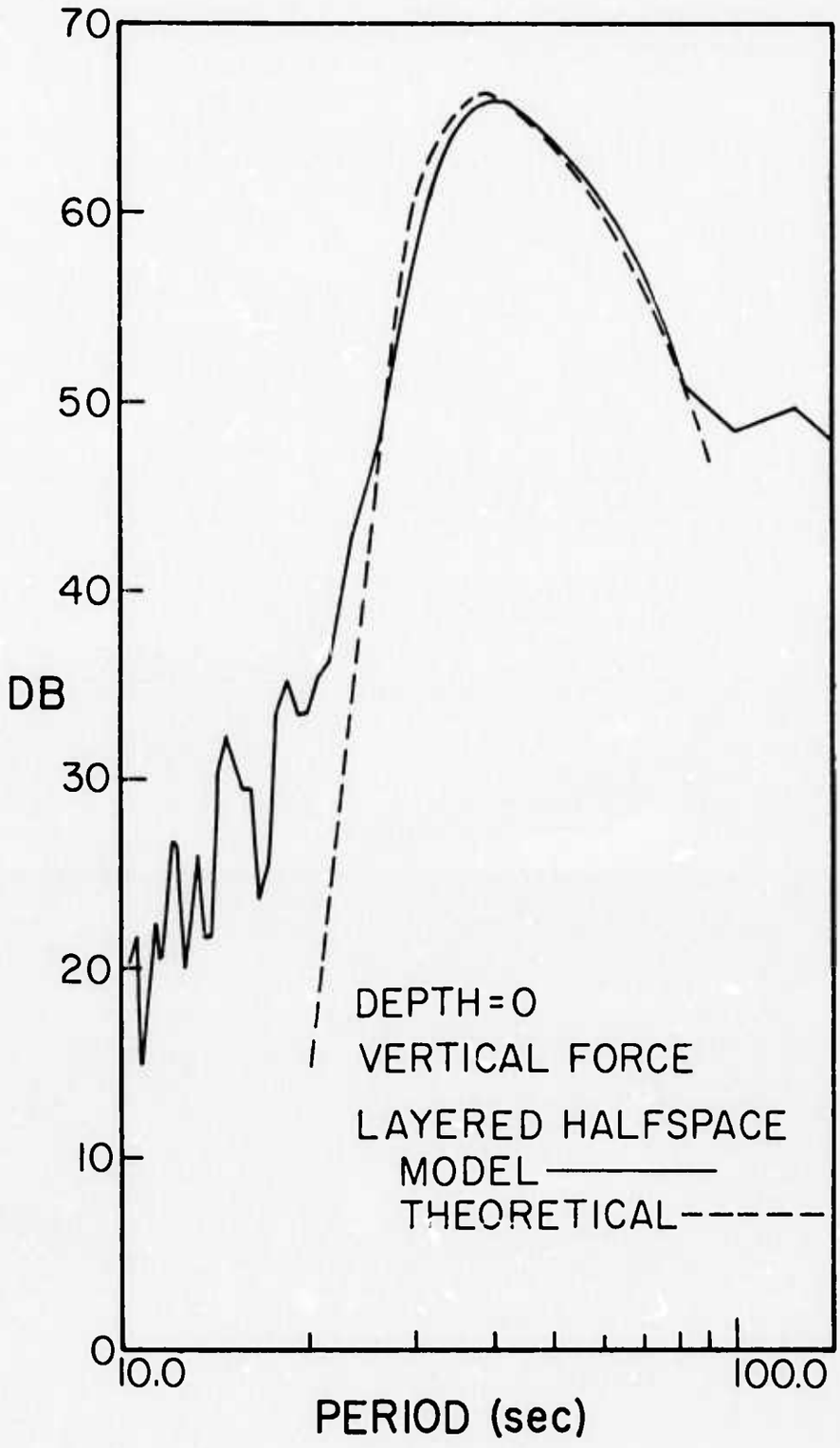
70
60
50
40
DB
30
20
10
0
10.0
100.0
PERIOD (sec)
DEPTH=0
VERTICAL FORCE
LAYERED HALFSPACE
MODEL
THEORETICAL

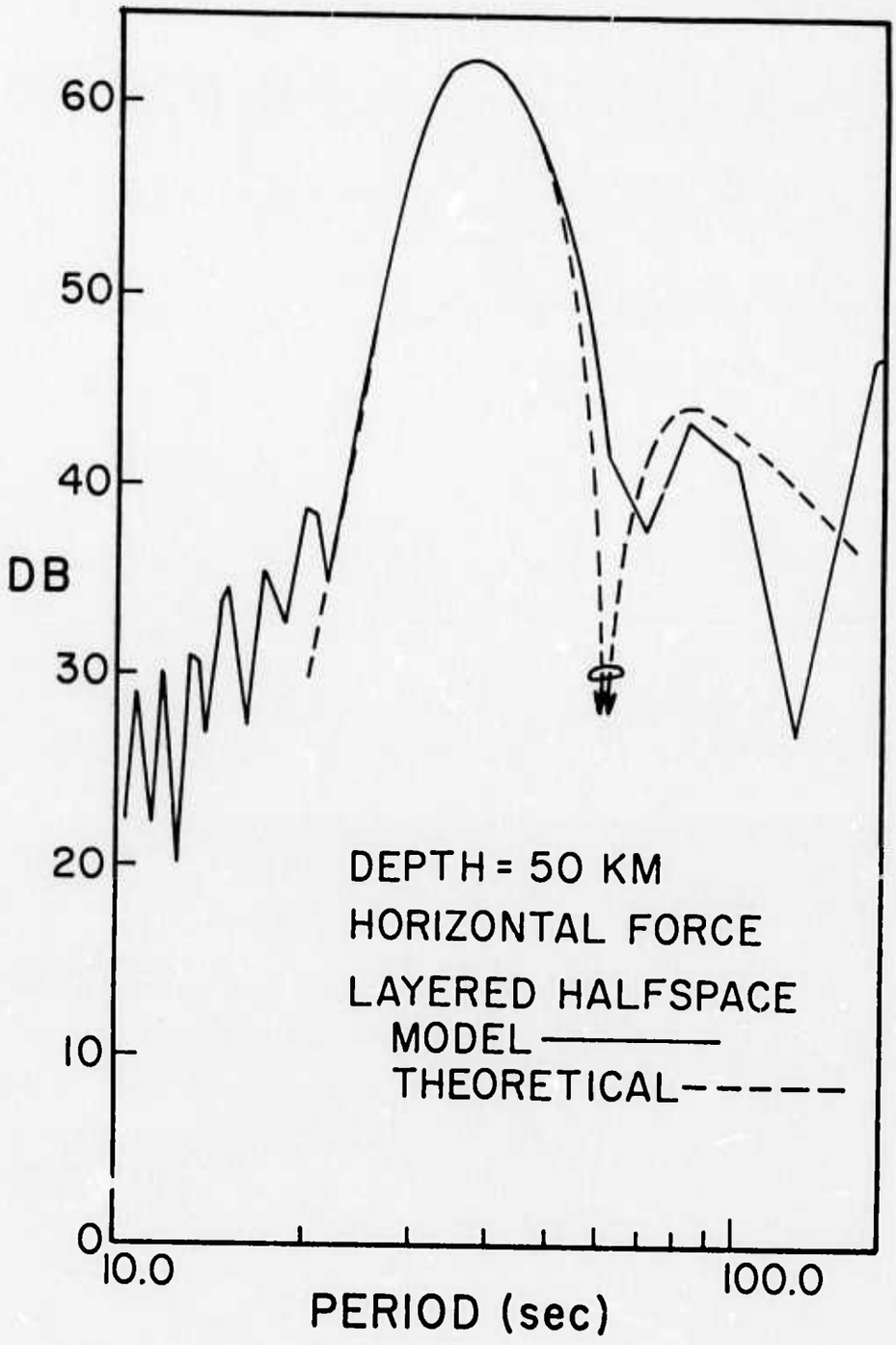
60
50
40
DB
30
20
10
0
10.0
100.0
PERIOD (sec)
DEPTH = 50 KM
HORIZONTAL FORCE
LAYERED HALFSPACE
MODEL
THEORETICAL

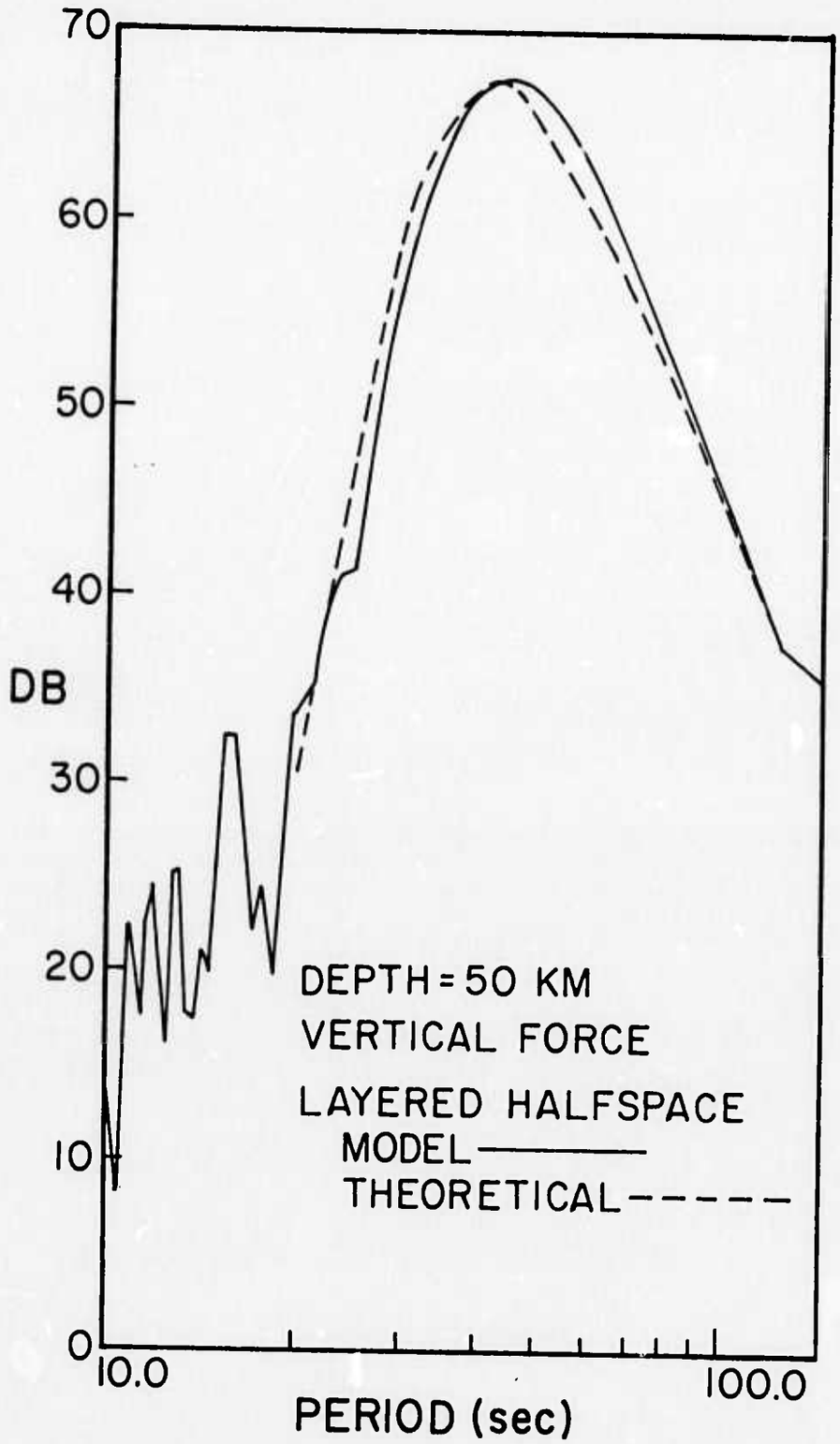
70
60
50
40
DB
30
20
10
0
10.0
100.0
PERIOD (sec)
DEPTH = 50 KM
VERTICAL FORCE
LAYERED HALFSPACE
MODEL
THEORETICAL

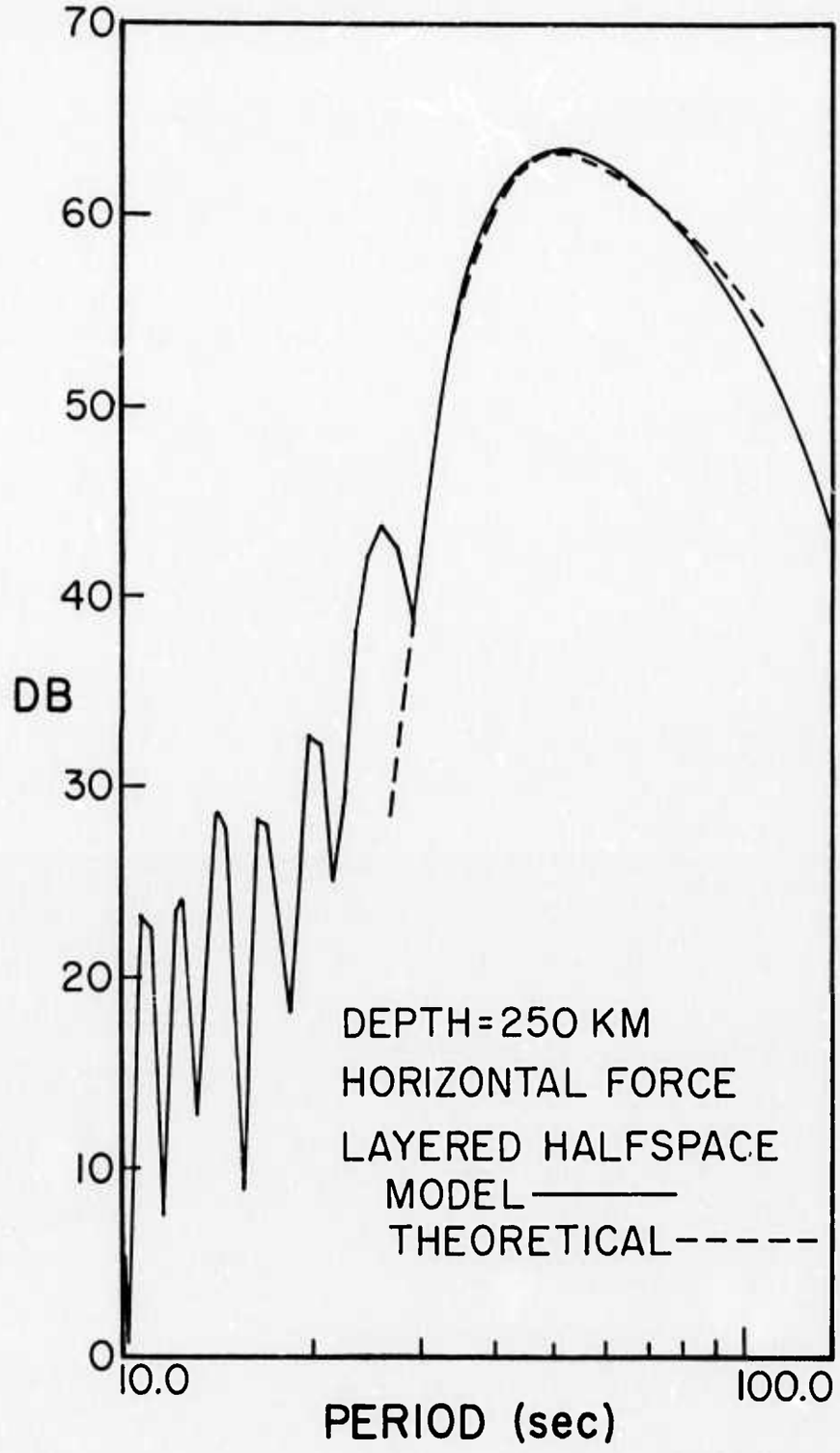
70
60
50
40
DB
30
20
10
0
10.0
100.0
PERIOD (sec)
DEPTH=250 KM
HORIZONTAL FORCE
LAYERED HALFSPACE
MODEL
THEORETICAL

147<

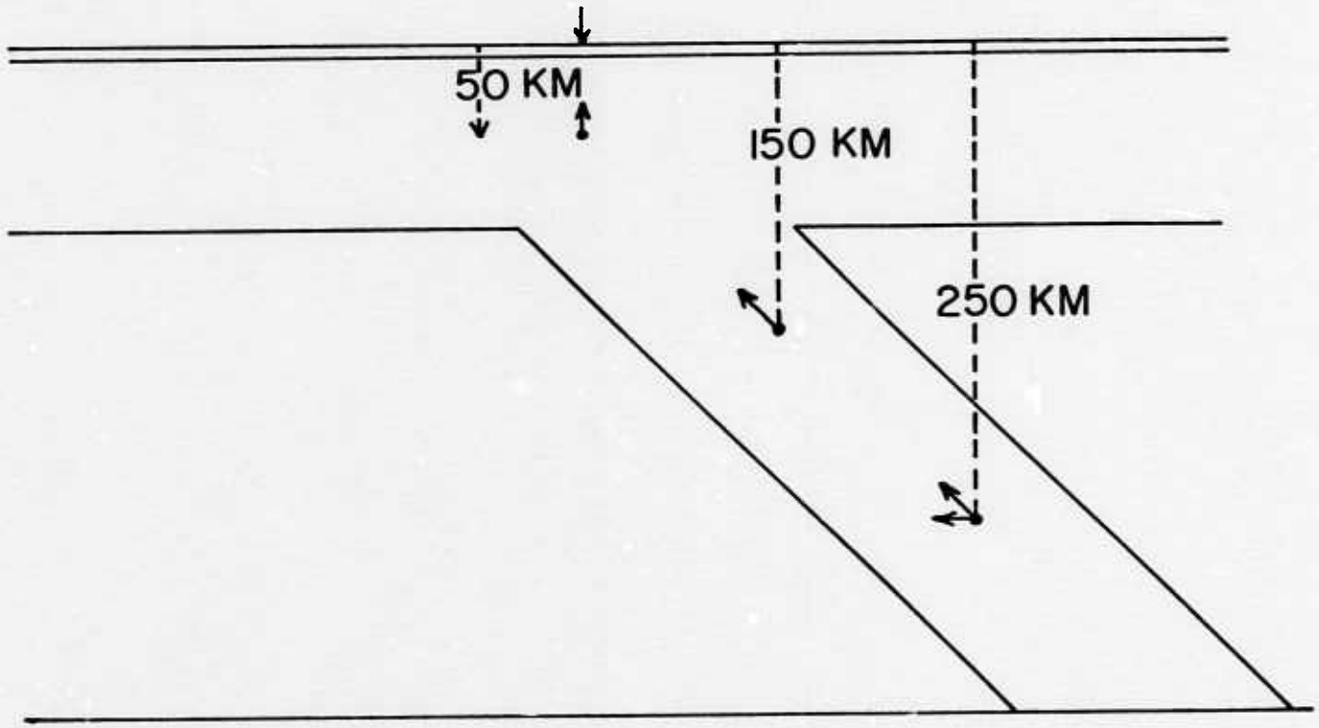

143

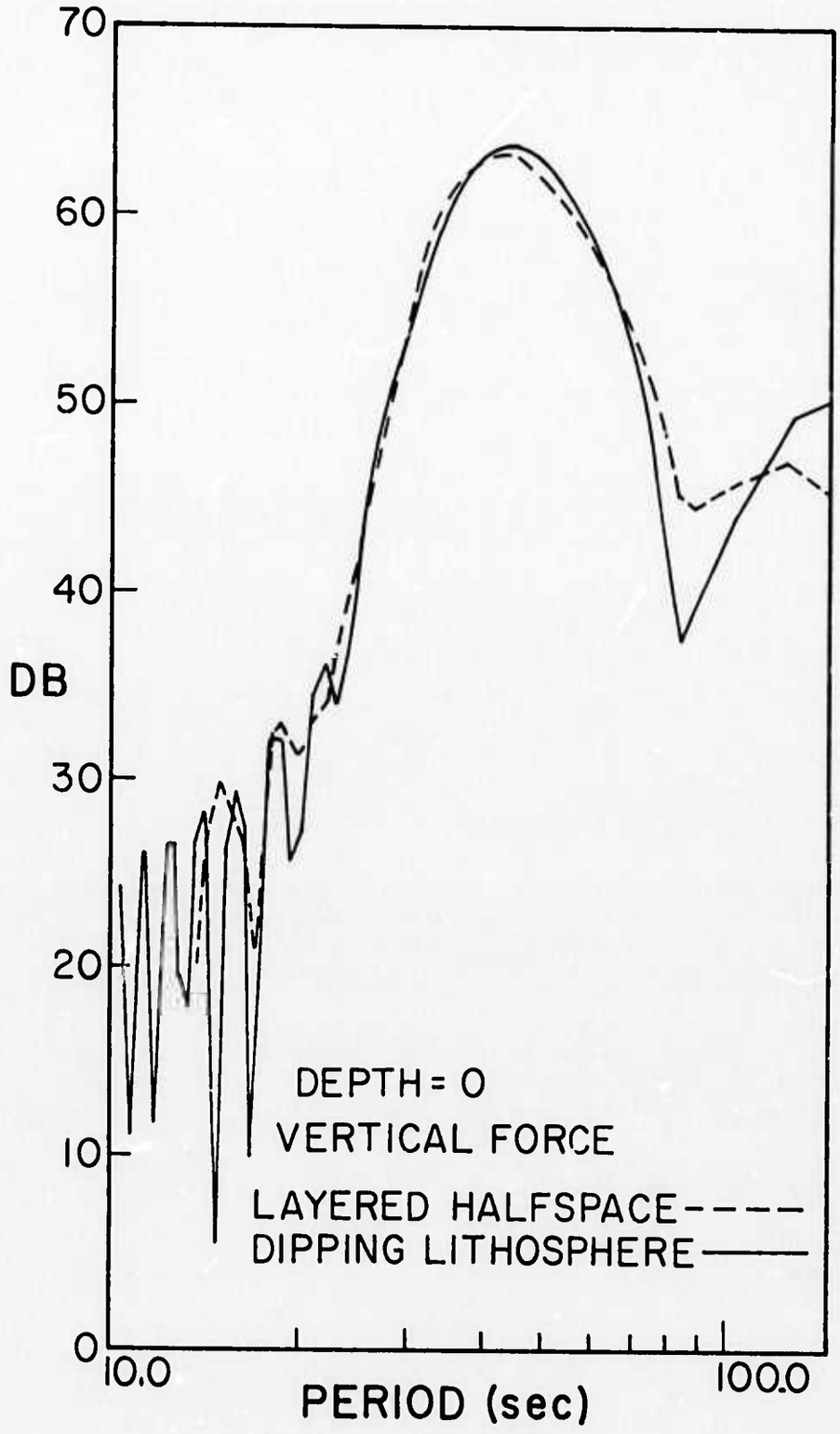
70
60
50
40
DB
30
20
10
0
10.0
100.0
PERIOD (sec)
DEPTH = 0
VERTICAL FORCE
LAYERED HALFSPACE----
DIPPING LITHOSPHERE——

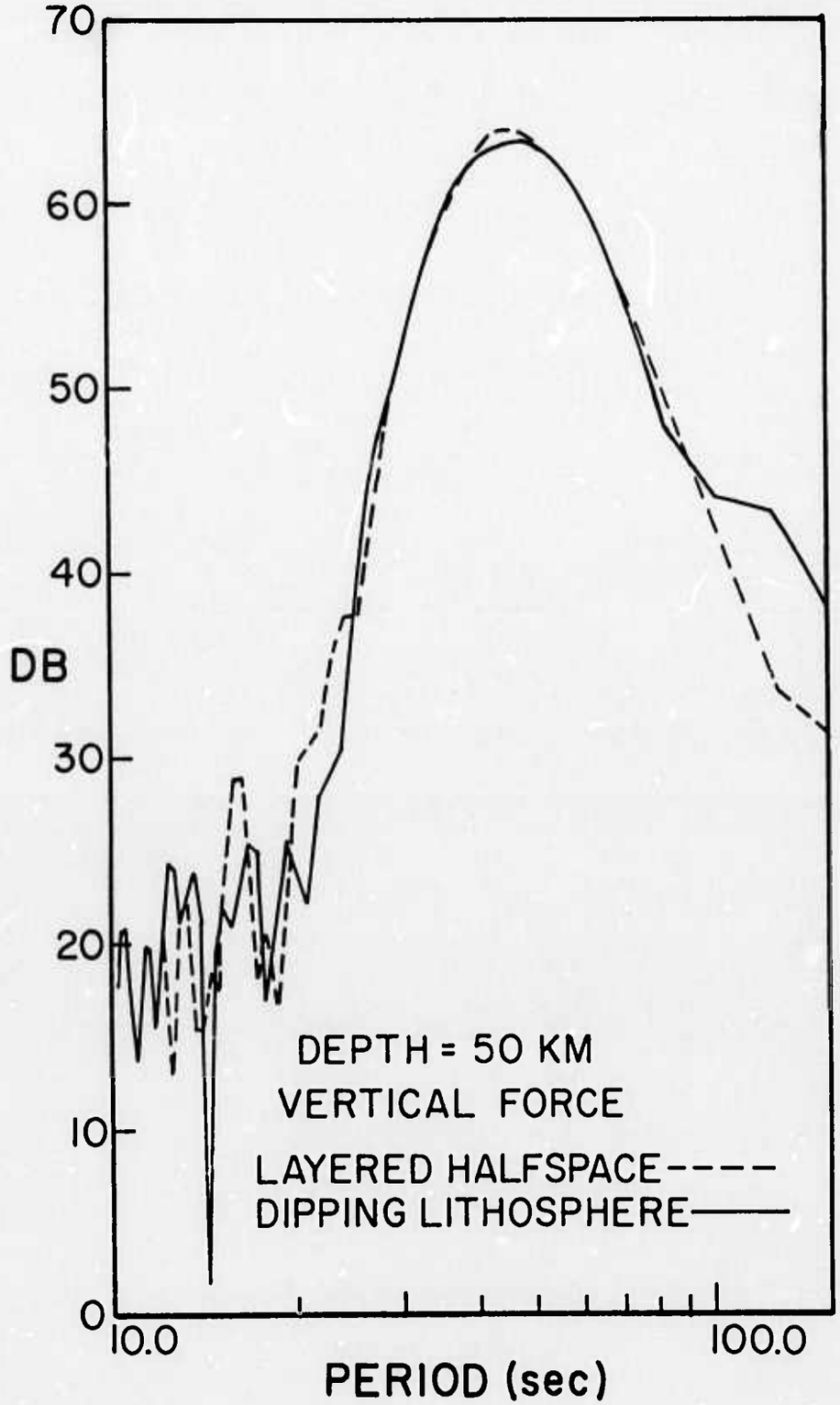
70
60
50
40
DB
30
20
10
0
10.0
100.0
PERIOD (sec)
DEPTH = 50 KM
VERTICAL FORCE
LAYERED HALFSPACE----
DIPPING LITHOSPHERE——

150

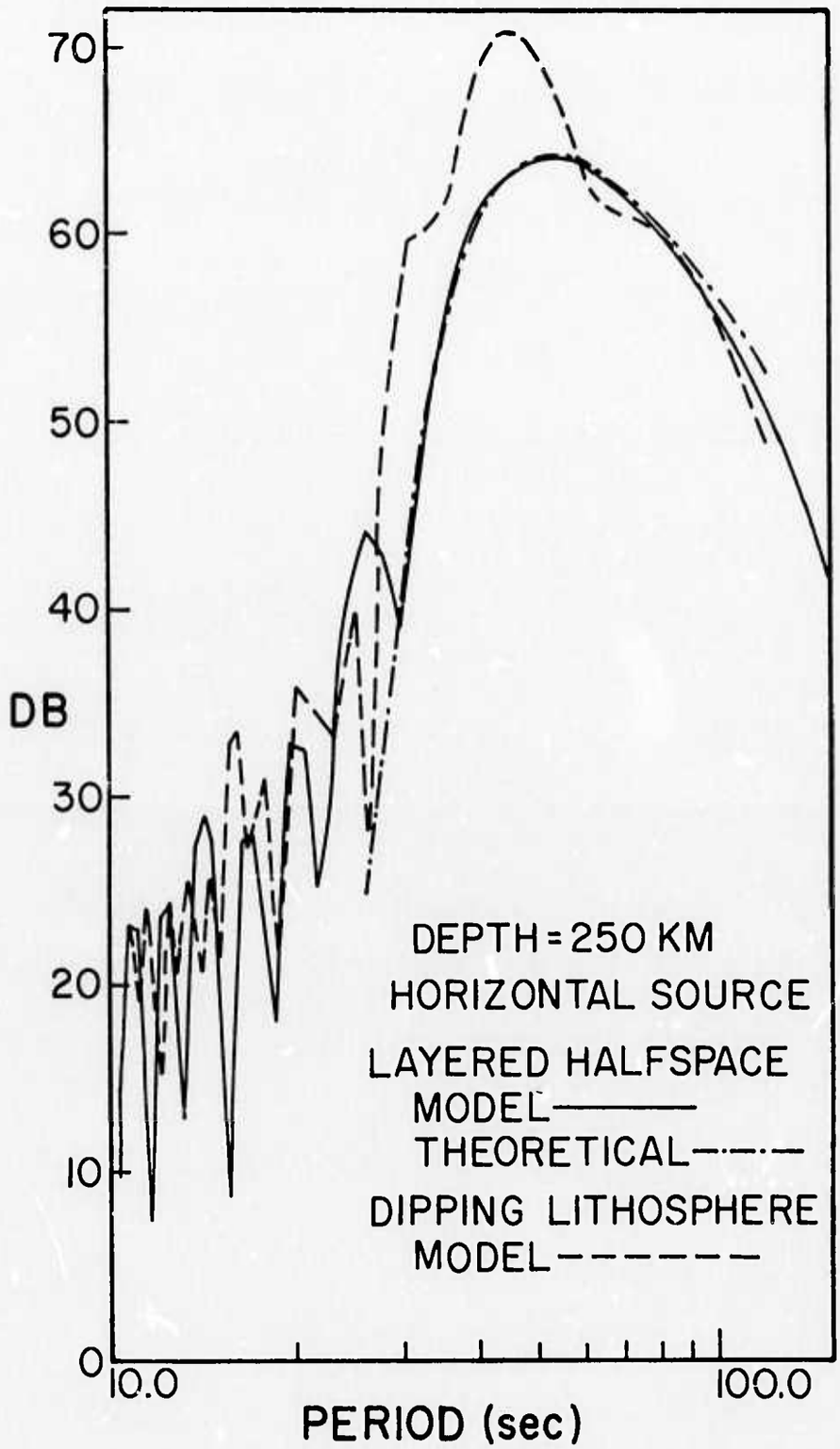
70
60
50
40
DB
30
20
10
0
10.0
100.0
PERIOD (sec)
DEPTH = 250 KM
HORIZONTAL SOURCE
LAYERED HALFSPACE
MODEL
THEORETICAL
DIPPING LITHOSPHERE
MODEL

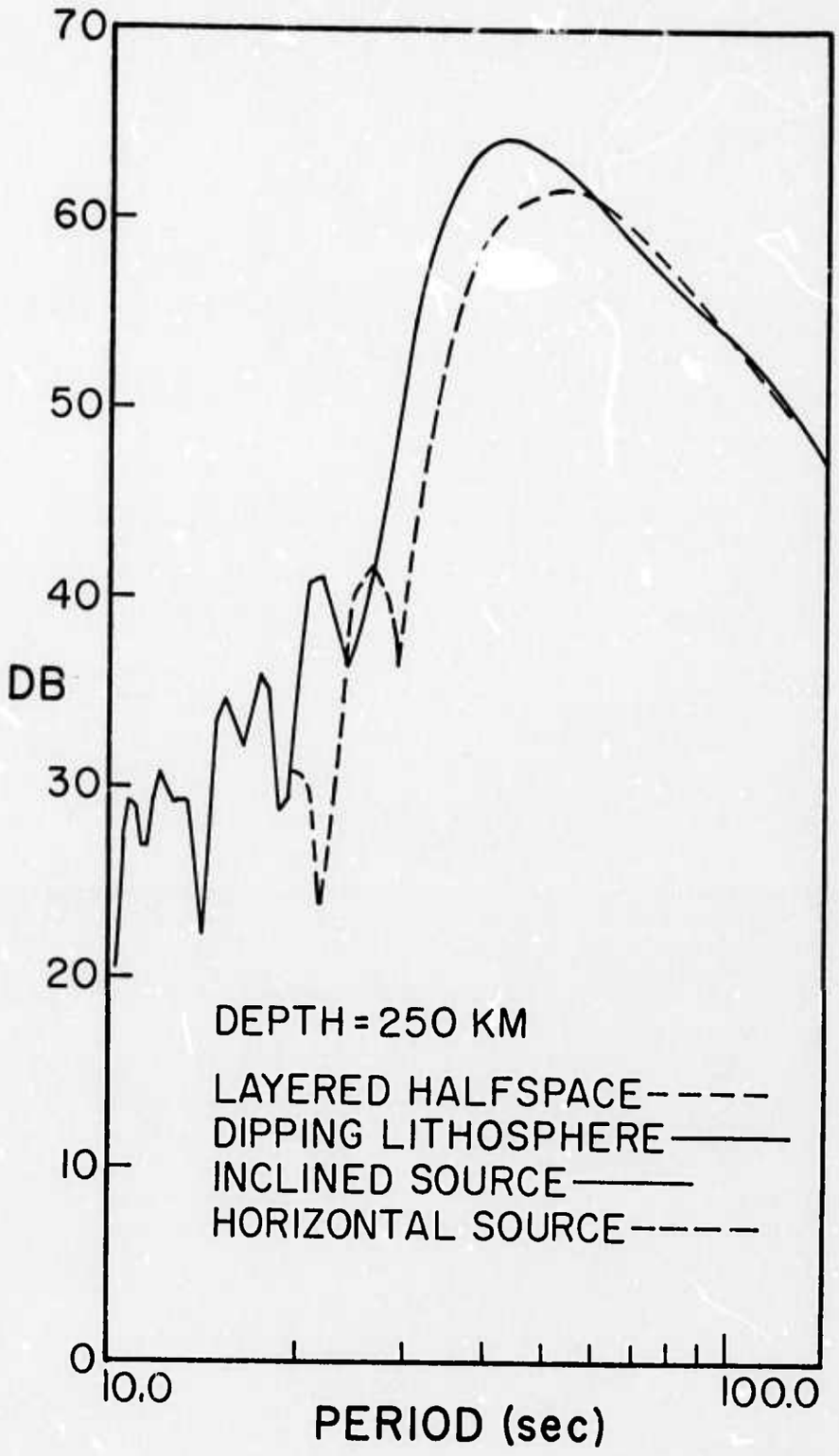
70
60
50
40
DB
30
20
10
0
DEPTH = 250 KM
LAYERED HALFSPACE----
DIPPING LITHOSPHERE——
INCLINED SOURCE——
HORIZONTAL SOURCE----
10.0
100.0
PERIOD (sec)

152

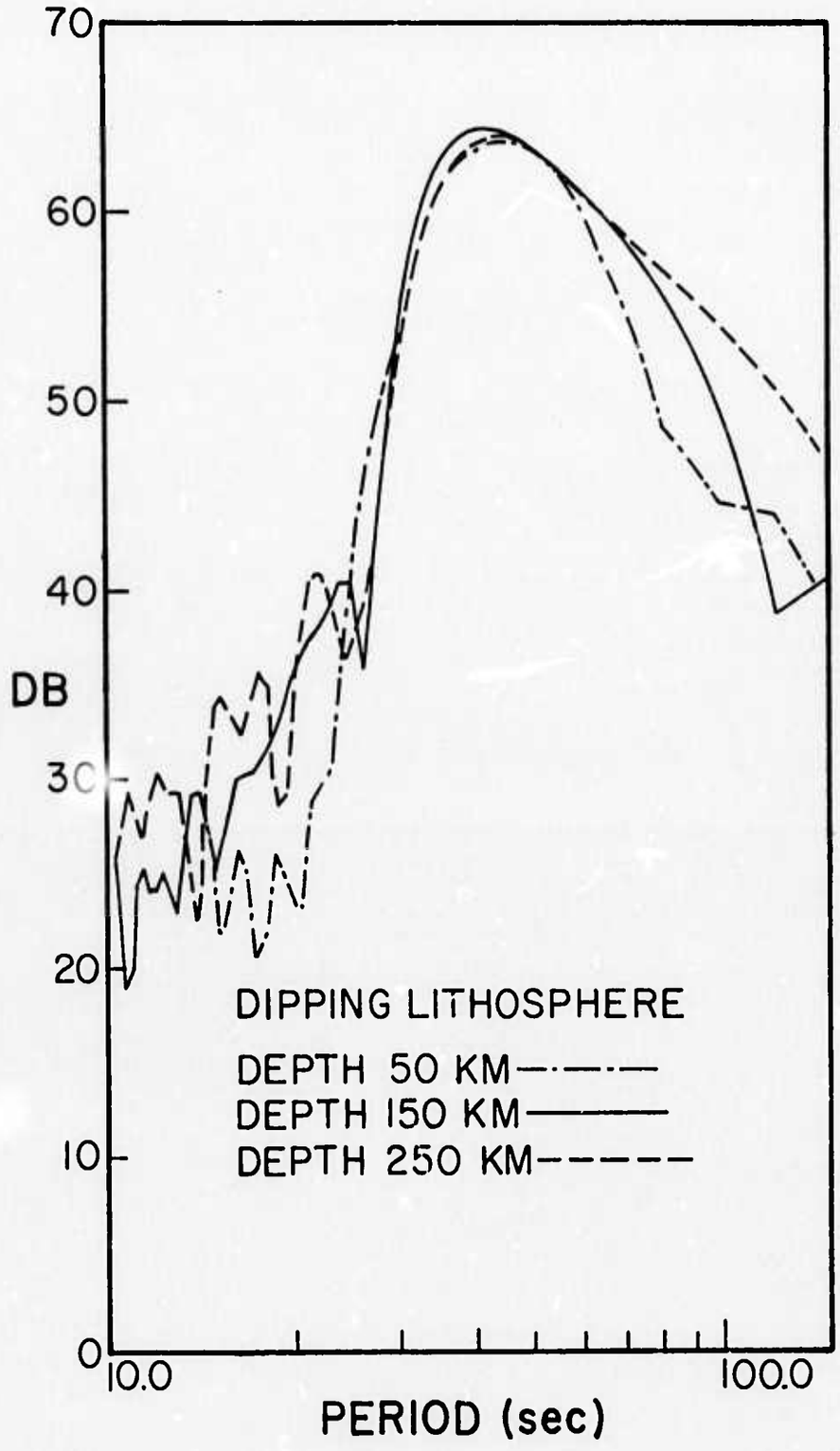
70
60
50
40
DB
30
20
10
0
10.0
100.0
PERIOD (sec)
DIPPING LITHOSPHERE
DEPTH 50 KM
DEPTH 150 KM
DEPTH 250 KM

153

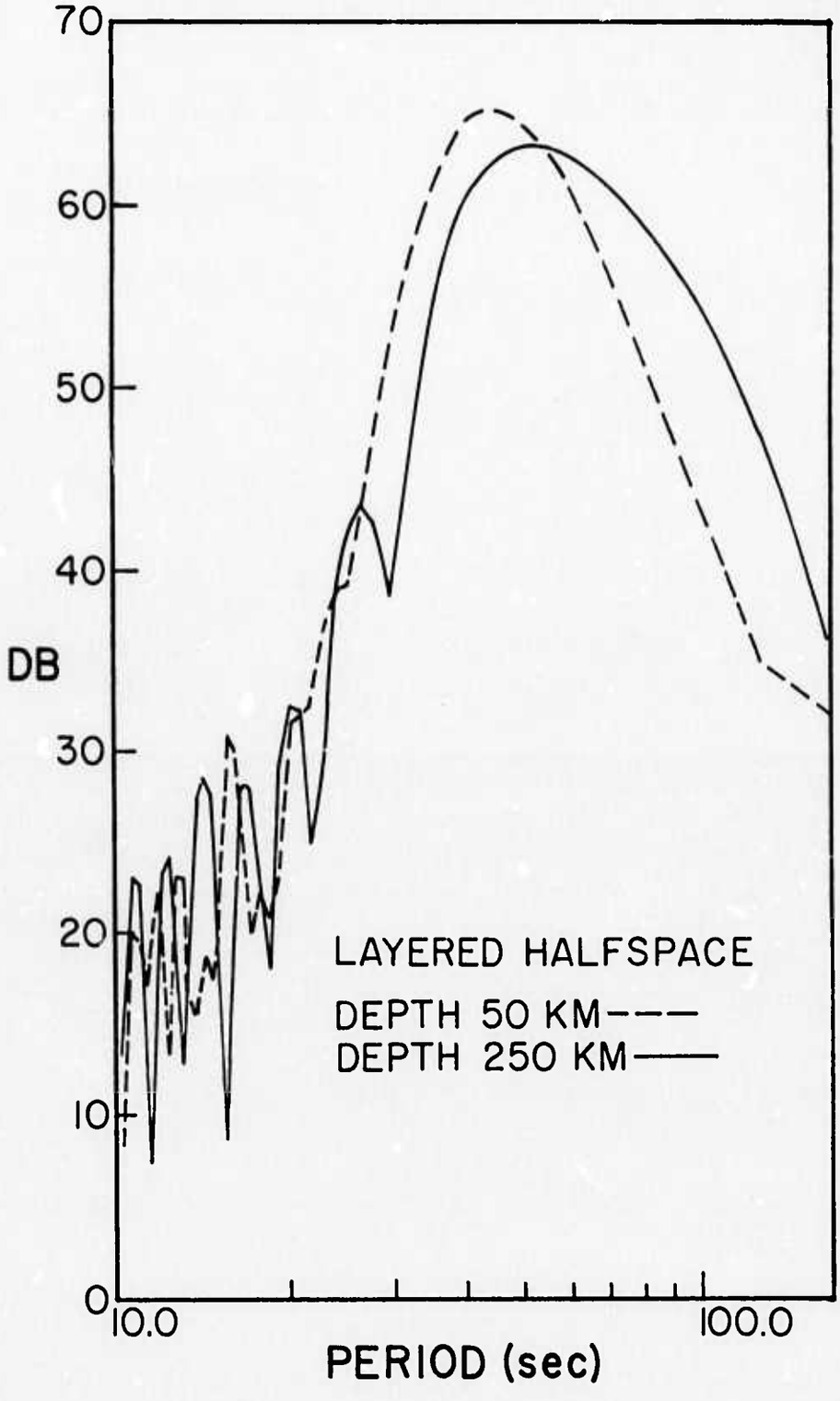
70
60
50
40
DB
30
20
10
0
10.0
100.0
PERIOD (sec)
LAYERED HALFSPACE
DEPTH 50 KM---
DEPTH 250 KM——